Nanoparticle Morphology Control in Multi-Material Polymer Composite Fibers

by

Weiheng Xu

A Dissertation Presented in Partial Fulfillment
of the Requirements for the Degree
Doctor of Philosophy

Approved June 2022 by the
Graduate Supervisory Committee:

Kenan Song, Chair
Xiangfan Chen
Beomjin Kwon
Bruno Azeredo

ARIZONA STATE UNIVERSITY

August 2022

ABSTRACT

Polymer composite has been under rapid development with advancements in polymer chemistry, synthetic fibers, and nanoparticles. With advantages such as lightweight, corrosion resistance, and tunable functionalities, polymer composite plays a significant role in various applications such as aerospace, wearable electronics, energy storage systems, robotics, biomedicine, and microelectronics. In general, polymer composite can be divided into particulate-filled, fiber-filled, or network-filled types depending on the manufacturing process and internal structure. Over the years, fabrication processes on the macro- and micro-scales have been extensively explored. For example, lamination, fiber tow steering, and fiber spinning correspond to meter, millimeter, and micrometer scales, respectively. With the development of nanoparticles and their exceptional material properties, polymer nanoparticle composite has shown promising material property enhancements. However, the lack of economical solutions to achieve nanoscale nanoparticle morphology control limits the reinforcement efficiency and industrial applications. This dissertation focuses on utilizing additive manufacturing as a tooling method to achieve nanoparticle morphology control in polymer nanocomposite fibers. Chapter 1 gives a thorough background review regarding fiber composite, additive manufacturing, and the importance of nanoparticle orientation. Two types of nozzle designs, concentrical and layer-by-layer, are 3D printed and combined with the dry-jet-wet fiber spinning method to create continuous fibers with internal structures. Chapters 2 to 5 correspond to four stages of my research, namely, (2) multi-material fiber spinning, (3) interfacial-assisted nanoparticle alignment, (4) microscale patterning, and (5) nanoscale

patterning. The achieved feature resolution also improves from 100 Âµm, 10 Âµm, 2 Âµm, to 170 nm, respectively. The process-structural-property relationship of polymer nanocomposite fibers is also investigated with applications demonstrations including sensors, electrically conductive fibers, thermally conductive fibers, and mechanically reinforced fibers. At last, Chapter 6 gives a summary and some future perspectives regarding fiber composites.

This thesis work is dedicated to my parents who have been the constant source of support and encouragement. This work is also dedicated to my lovely wife and children, Yinlian, Yaen, and Haoen. I am thankful for having you in my life.

ACKNOWLEDGMENTS

I would like to take advantage of this opportunity to thank those who have shown me love and support. It is truly an exciting period of my life, and I appreciate every moment of my Ph.D. studies.

First of all, I would like to acknowledge and give my warmest thanks to my supervisor, Professor Kenan Song, who introduced me to the field of polymer composite and showed continuous support through all stages of my Ph.D. study and research.

Secondly, I am grateful to my committee members, Professor Xiangfan Chen, Professor Beomjin Kwon, and Professor Bruno Azeredo who have dedicated their time and effort to my research and have contributed insightful comments and visions on both research and career path directions.

Thirdly, I thank my fellow labmates and friends, Sayli Jambhulkar, Dharneedar Ravichandran, Yuxiang Zhu, Rahul Verma, Rahul Franklin, Namrata Kanth, Mounika Kakarla, Mohammed Bawareth, Amm Hasib, Siying Liu, Wenbo Wang, and Luyang Liu. It is their help that has made my research possible. I am also grateful for the much fun I had with new members of AMAML, Dhanush Patil, Nathan Fonseca, and Varun Kumar. In addition, I appreciate all help I received from the ASU Poly business center, especially our account manager Lisa Zelasko, and my academic advisor, Meghan Vaughn.

Last but not least, I received valuable advice and comments from the Eyring Materials center, especially from David Lowry, Sisouk Phrasavath, Kenneth Mossman, Douglas Daniel, Timothy Karcher, Emmanuel Soignard, and Karl Weiss.

TABLE OF CONTENTS

Page

LIST OF TABLES viii

LIST OF FIGURES ix

CHAPTER

1 INTRODUCTION 1

1.1 Background 1

1.2 Continues Fiber Spinning Techniques 2

1.3 Multimaterial Composite Fibers 5

1.4 Importance of Nanoparticle Orientation 9

1.5 Additive Manufacturing as Tooling Engineering for Nozzle Design 14

1.6 Strategies to Utilize 3D Printing for Nanoparticle Morphology Control 16

2 MULTIMATERIAL FIBER SPINNING WITH COAXIAL STRUCTURE FOR VOLATILE ORGANIC COMPOUNDS SENSING 18

2.1 Introduction 18

2.2 Experimentation and Characterization 21

2.3 Rheological Control for Self-Induced Hollow Core 24

2.4 Optimization of the Middle Chemiresistive layer 28

2.5 Multilayer Multimaterial VOCs Sensor 31

2.6 Sensitivity and Selectivity of Multilayered VOCs sensor 33

2.7 Piezoresistive Sensing 37

2.8 Conclusion 44

CHAPTER Page

3 IN-SITU ALIGNMENT OF GRAPHENE NANOPLATELETS VIA COAXIAL FIBER SPINNING 45

3.1 Introduction.....45

3.2 Experimentation and Characterization.....47

3.3 Multilayer Morphology and Nanoparticle Orientation Studies 49

3.4 Mechanical and Electrical Properties.....57

3.5 Conclusion 59

4 MICROSCALE PATTERNING OF NANOPARTICLES FOR ANISOTROPIC PROPERTIES 60

4.1 Introduction.....60

4.2 Experimentation and Characterization.....65

4.3 Rheological Behavior Study 68

4.4 Multilayer Morphologies.....76

4.5 Mechanical Properties 80

4.6 Parallel Model for Thermal Conductivity.....88

4.7 Further Application Demonstrations.....95

4.8 Conclusion 99

5 NANOSCALE PATTERNING AND MORPHOLOGY CONTROL OF CARBON NANOTUBES IN COMPOSITE FIBER 100

5.1 Introduction.....100

CHAPTER Page

5.2 Experimentation and Characterization....103

5.3 CNTs Dispersion Quality....105

5.4 Mechanical Reinforcement....114

5.5 Polymer Crystallinity Dependency on Layer Morphology....119

5.6 Layer-Layer Interactions....125

5.7 Shear Stress-Induced Nanoparticle Orientation....129

5.8 Conclusion....133

6 SUMMARY AND FUTURE OUTLOOK....135

REFERENCES....137

APPENDIX

A STATEMENT OF COAUTHORS' PERMISSIONS....152

LIST OF TABLES

Table		Page
1.	Nanoparticle Alignment Mechanisms	11
2.	3D Printing-Facilitated Nozzle Designs	16
3.	Fiber Drawing Conditions and Diameters	49
4.	Summary of the Spinning Dope Compositions and Fiber Terminology	72
5.	Fitted Carreau-Yasuda Model (Equation 5.1) of Different Types of Solution	108
6.	Draw Ratios of All Types of Fibers	109
7.	Mechanical Data of All Fibers	118
8.	The Activation Energy Calculated for the Cyclization Process	124
9.	DSC Peak Temperatures of All Fibers for Different Heating Rates	124

LIST OF FIGURES

Figure Page

1. Common Fiber Spinning Techniques. Adapted with Permission From Ref[29].... 4
2. (a) Number of Publications Containing Keywords “Core-Shell Structure” and “Fiber” Based on Google Scholar Search (1995-2020). (b) Examples of Microstructures in Fiber Materials..... 5
3. (a) Solidworks Sketch of the Multi-Channeled Spinneret. (b) 3D Printed Spinneret Using 3D Laser Sintering. (c) Internal Spinneret Structure for Multi-Material Extrusion. 19
4. Schematics of (a) Dry-Jet-Wet Fiber Spinning Process and (b) Multilayered Composite Vocs Sensor. 21
5. SEM Images of 20wt% Soft35 TPU with Water to Methanol Ratios of 100:0, 80:20, 50:50, 20:80, 0:100. Scale Bars Are 50 µm. 25
6. Fiber Morphology Characterization. (a1) The Cross-Section of 20wt% TPU Soft35 with Magnified Images Showing (a2) Across Layers, (a3) Interior Surface, and (a4) Exterior Surface Morphology with the Inserted Photo Showing the Fiber Flexibility. 26
7. (a) The Relationship Between Storage and Loss Moduli with Increasing Oscillation Strain for 20 Wt%, 40 Wt%, and 50 Wt% TPU Soft35, and (b) Their Corresponding Tan Delta Values. The Cross-Section SEM Image of the Multi-Layered Fiber with (c1) 28 Wt% 1185, (c2) 40 Wt% Soft35 and (c3) 20 Wt% Soft35 as the Core Layer. 27

Figure Page

8. Optimization of the Middle Sensing Layer. (a) The Electrical Conductivity of 1-Phase Fibers with 3 Wt% Nanofillers At Different Ratios of MWCNTs. (b) The Tan Delta Values for the Spinning Solution Under Stress Sweep Oscillation. (c) Uniaxial Stress and Strain Curves for 1-Phasex%Cnts Fibers, and (d) Electrical Responses for 1-Phasex%Cnts Fibers Under 420 Ppm of Methanol..... 30
9. SEM Images of (a) GnPs and (b) Multi-Walled Cnts with Scale Bars of 2 μm.. 31
10. Vocs Sensor Comparison Between the 1-Phase95%Cnts and 4-Phase95%Cnts Sensors In (a) Chemiresistive Response, Structure Morphologies of (b1-2) 1-Phase and (b3-4) 4-Phase Fibers, (c) Humidity Influence on the Electrical Stability, and (d) Cyclical Temperature Influence on 4-Phase95%Cnts..... 33
11. Sensing Characterization of the 4-Phase95%Cnts Fiber as Vocs Pass Through the Hollow Core. (a) A Schematic of the Experimental Setup. (b1-4) The Response Characteristics to Hexane, Methanol, Ethanol, and Xylene At Different Concentrations for 30 Seconds. (c) Summarized Relationship Between Output Response and Input Vapor Concentrations for Different Solvents..... 36
12. The Swelling Degree of the Polymer Under Different Types of Solvents with Their Observed Lod..... 36
13. Chemiresistive Behavior of the 4-Phase95%Cnts Sensor Under the Influence of Strain Deformation. 39
14. The In-House Testing Setup Combines a Dynamic Mechanical Analyzer (DMA) with the Chemiresistor. 40

Figure Page

15. Long-Term Mechanical Stability of the Sensor. (a) The Sensor's Storage Modulus and Electrical Response During and After Constant 130 Ppm Ethanol Flow for 8 Hours. (b) The Zoomed-in Response of the Corresponding Sections Demonstrates the Detection of 0.1% Strain During and After VOCs Sensing..... 42
16. The Experimental Set-up for Pressure Sensing. 43
17. Piezoresistive Effect Under Air Pressure of the 4-Phase95%Cnts Fiber with (a) Stepwise Increase of Pressure and (b) Cyclic Performances. 43
18. Schematic of the (a) 3-Phase GnPs/PVA Fiber and (b) 1-Phase, 2-Phase, 3-Phase, and D-Phase Fiber Structures..... 46
19. Cross-Sectional SEM Images of the as-Spun (a) 1-Phase, (b) 2-Phase, (c) 3-Phase, (d) D-Phase Fibers. (e) Optical Microscope Image of 2-Phase and 3-Phase Fibers. (f) TGA Weight Residue with Respect to Drawing Ratios..... 51
20. Cross-Sectional SEM Images of the (a) 3-Phase Fiber After Drawing with Corresponding (B1-3) Showing Zoomed-in Sections..... 53
21. Crystallinity Based on (a) DSC Measurements of Enthalpy of Fusion and (b) XRD Fitted Area. 53
22. Raman Spectroscopy Data and Illustration of the Alignment Process. (a1) Cross-Sectional View (Along the Fiber Axis, Y-Axis) of the 3-Phase Fiber Showing Middle and Side Sections for Raman Spectroscopy Tests. (a2) Top View (Perpendicular to the Y-Axis). Normalized 2D Band Intensity for (b) Middle and (c) Side Sections. 55

Figure Page

23. Schematic of the GnP Alignment Process. 56

24. Mechanical and Electrical Properties. (a) Stress-Strain Curves Fiber Different Fibers. (b) Relationship Between Modulus and Electrical Conductivity of 3-Phase Fiber. 58

25. Fracture Surface Morphology of (a) 1-Phase, (b) 2-Phase, (c) 3-Phase, and (d) D-Phase Fibers. 59

26. The Experimental Design and Setup. (a) The Combination of Dry-Jet-Wet Spinning and Force Assembly Process for the Fabrication of Multilayered Fiber. (b) the Working Mechanism for the Force Assembly Process. 62

27. Design of the Multilayered Spinneret. 63

28. (a) Comparisons Among the Maxwell-Eucken, Parallel, and Series Models (Insert Illustrations).[187] (b) Schematic Illustrations of the Hierarchically Structured Composites, From Nanoscale Layers to Microscale Fibers to Macroscale Fabrics. 65

29. The Flow Behaviors of Different BN Volume Concentrations with (a) 15 wt%, (b) 12 wt%, (c) 10 wt% (d) 5 wt% PVA/DMSO. 69

30. Composition Optimization for Spinnability and Layer Formation of (a) Viscosity (b) Tan(Δ) At Different BN and PVA Concentrations. (c) Viscosities of Pure PVA and BN/PVA Suspensions. (d) The Fiber Composition Spinnable Window..... 73

31. Layer Formation Morphology Studies of a 64-Layered Composite with Distinct Layers and Disrupted Layers. 74

Figure Page

32. CFD Simulations of the Layer Formability of the 16L10% Fiber Going Through Four Multipliers (#1-4). 74

33. (a) DSC of Tg with Increased BN Vol%. TGA of Fibers with (b) Different Layer Numbers and (c) Different BN Vol%. (d) A Weight Residue Comparison Between the Experimental and Theoretical Values of the 32-Layered Fibers. 76

34. Experimentally Measured and Theoretically Predicted Layer Thickness Along the Dotted Black Line with Increased Layer Numbers..... 78

35. (A1-2) Optical Images of the As-Spun 64L10% Fiber From the Major and Minor Axis, Respectively. Cross-Sectional SEM Images of (b) the Post-Drawn 64L10% Fiber with Zoom-in Regions Showing the (c) BN Layers with Falsified Coloring and (d) BN Nanoparticle Morphology. Micro-CT Images of the 3D Continuous BN Channels for (E1-2) 8L10% and (F1-2) the 16L10% Fibers From the Top and Oblique Views. 78

36. (a) Assembled Nozzles with 5 Multipliers. Exiting Nozzle Geometries with Aspect Ratios of (b1) 1, (c1) 2, and (d1) 10, and Their Corresponding Fiber Cross-Sectional SEM Images with Aspect Ratios of (b2) 1, (c2) 1.5, and (d2) 2.5. 80

37. Mechanical Properties of Uniform and Layered Fibers (a) Stress-Strain Curves of Uniform Fibers After Drawing At 100 °C. (b) Young's Modulus and Ultimate Tensile Strength Between the Uniform and 32-Layered Fibers After Hot Drawing At 100 °C. 83

Figure Page

38. Mechanical Properties of Uniformly Structured Fibers Drawn At 25 °C, 100 °C, and 180 °C. (a and b) The Ultimate Tensile Strength and (c and d) Young's Modulus. 83

39. Micro-CT Scan for the U20% Composite Fibers with Voids as Defects After Hot Drawing..... 84

40. Mechanical Properties of Layered Fibers. (a) Relationships of Young's Modulus and Ultimate Tensile Strength Values with Different Layer Numbers. (b) Deformation Simulations of Fibers with Different Layer Numbers Via FEM. The Stress-Strain Curve of 32L10% Fibers Drawn At (c) Room Temperature and (d) 100 °C with Stepwise Fractures. (e) SEM Images of the 32L10% Fibers Showed Distinct Surface Morphologies within the PVA and PVA/BN Layers During Fracture. 86

41. Fractured Fiber Morphologies of the (a) Pure PVA, (b) 4L10%, and (c) 8L10%, Fibers (Top) with Zoomed-in Sections (Bottom) 87

42. (A1) Schematics Showing the Crack Propagation Route with (a2-3) the SEM Images of Propagated Cracks in PVA and 32L10% Fibers, Suggesting that the BN-Containing Layers Served as Crack Barriers or Reflectors. 87

43. 10vol% BN Loaded Fibers with Their Stepwise Fracture Probability. 88

44. Thermal Conductivity Calculation and Measurements. 89

45. Schematic Illustration of the Proposed Thermal Conductive Pathways for Uniform (the Top Insert) and Layered (the Bottom Insert and the SEM Image) Fibers. 91

Figure Page

46. FEA of Thermal Behaviors of the Multilayered Fibers. (a) Simulation Result of 20 Vol% BN/PVA Fibers with Different Layer Thicknesses with (b) Top Surface Temperature Profiles and (c) Averaged Overall Fiber Temperatures. (d) A Zoomed-in Section of B with Arrows Indicating the Minimum and Maximum Temperatures of the PVA and BN/PVA Layers, Respectively, and (e) Shows the Temperature Changes with Layer Numbers. 93

47. (a) Handwoven 32L20% Fiber Fabric Showed the Thermal Response Differences Between (b) 32L20% Fabrics (Top) and Pure PVA Fabrics on a Peltier Plate (Bottom). (c) An Experimental Setup (Bottom Schematic) with Programmable Heating Rates (Top Figure) for Measuring (d) Static and (e) Dynamic Thermal Responsiveness of the 32L20% and PVA Fabrics. 95

48. Potential Applications of the Fiber Layering Technique. (a) A CFD Simulation of Layer Formability in the Series Model. (b1) An Optical Image of the Layered Al/PAN Fiber, (b2) SEM Imaging of the Porous PAN Fiber. (b3) A Zoomed-in SEM Image of the Pores-Aligned Layer and Solid Layer Regions. (b4) Predicted Thermal Conductivity Values Based on the Series-Maxwell-Eucken Model.[187] (c1-2) SEM Images of Alternating Layers in BN/GnPs Composite Fibers. (c3) Measured Anisotropic Electrical Conductivity of the Thermally Conductive Fiber Along and Across the Fiber Axial Direction. 98

49. Schematic of the Carbon Fiber Hierarchal Structure From Nano to Macro Scales. 103

Figure Page

50. Multilayer Structure Characterization. (a) Photograph During 32-Layer Fiber Spinning. (b) Cross-Sectional Optical Image of a 32-Layer Fiber. Rheology Behavior of (c1) PAN and CNT/PAN, and (c2) Stacked PAN and CNT/PAN Layers. (d) Stability Test of CNT/PAN and PAN Layered Solutions. 106
51. Optical Images for the As-Spun Fibers of 8-, 32-, 256-, 512-, 1024-Layered, and D-Phase Fibers. Images Were Processed Using ImageJ. The Coordinate of Each Spot Was Then Used to Calculate Their Nearest Neighbor Using MATLAB... 110
52. (a) SEM Images of the Post-Drawn 8-, 32-, 256-, 512-, and D-Phase Fibers Where Yellow- and Red-Colored Regions Represent CNT/PAN and PAN Layers, Respectively. the Mean and Standard Deviation Values of the Clusters of Post-Drawn Fibers in Terms of (b) Cluster Size and (c) the Nearest Neighbor Distance. 111
53. Nanoparticle Cluster and Dispersion Study. (a) CNT Cluster Distribution of the As-Spun Fiber. (b) First Nearest Neighbor Distribution of the As-Spun Fiber. (c) CNT Cluster Distribution of the Post-Drawn Fiber. (d) First Nearest Neighbor Distribution of the Post-Drawn Fiber. (e) The Mean and Standard Deviations of (a). (f) The Mean and Standard Deviations of (b). 113
54. Consistency of the Fiber Dimension During Fabrication. (a) Distribution of Collected Fiber Segments for Four Selected Fiber Types. (b) Calculated Fiber Diameters with Standard Deviation Compared with Measured Diameters From SEM Images. 114

Figure Page

55. Microtomed Cross-Sectional SEM Images of All Fiber Types 115

56. The Mechanical Properties of Different Fiber Types. (a) The Stress-Strain Curves of All the Multilayered Fibers Plus Pure PAN and D-Phase Fibers. (b) The Young's Modulus and Ultimate Tensile Strength of Different Fibers. (c) Enhancement of Ultimate Strength and Toughness with Increasing Layer Numbers. The Fracture SEM Images of (d) 512-Layered, (e) D-Phase, (f) 8-Layered, (g) and 1024-Layered Fibers at Room Temperature. 117

57. The Schematic Shows Different Fiber Morphologies of PAN Polymer Chains and CNTs Before and After Drawing. 119

58. XRD Measurements of Different Fiber Types..... 121

59. The D-Spacings (2θ ~17° Peak), Crystallite Sizes (2θ ~17° Peak), and Crystallinities for All Fiber Types. 122

60. DSC of All Fibers for Different Heating Rates Simulating the Stabilization Process with Calculated Activation Energy. 123

61. DMA of the Multilayered Fibers. (a) Storage Modulus, (b) Tan (Δ), (c) Tan $(\Delta)_S$, and (d) Tan $(\Delta)_{in}$ of Different Types of Fiber Structures. 127

62. Initial Tan (Δ)C Values at Room Temperature for Various Fibers and Their Peak Temperatures..... 128

63. (A1-5) SEM Images of the Fibers' Cross-Section After DMA with Temperature Sweeping. (b) The Measured Size of the Fractured Fibrils for Selected Fibers. 128

64. Polarized Raman Spectroscopy Mapping. 132

65. Comparison Between the Intensity of 0° and 90° for 512-Layered and D-Phase Fibers Shows I0°/I90° Ratios of 3.57 and 2.56, Respectively. 133

CHAPTER 1

INTRODUCTION

1.1.Background

One-dimensional (1D) fibers offer fascinating features, such as flexibility, large aspect ratio, high surface area, wearability, and inherent anisotropic characteristics. Since ancient times, humans have developed fabrics based on plants and animals, such as silk, hemp, cotton, wool, and fur.[1] For instance, there is evidence showing the use of artificially dyed flax fibers over 30,000 years ago.[2] The fibers' organic nature restrained their applications primarily to clothing and aesthetic purposes, with limited strain-to-break ranges (~10% to 30%), low ultimate tensile strength (<1 GPa), and low Young's modulus (< 20 GPa). The evolution of humanity and the need for advanced materials have urged researchers to synthesize much more durable artificial fibers from natural or synthesized materials. Since the first commercial synthetic polymer, known as Bakelite, in the 1900s, numerous high-performance macromolecule structure-based fibers have been developed, such as nylon, rayon, spandex, polybenzimidazole (PBI), polylactic acid (PLA), and aromatic polyamide.[3–5] For comparison, aramid fibers, commercially known as Kevlar, have an ultimate tensile strength greater than 2 GPa and Young's modulus greater than 120 GPa.[6] Since the mid-20th century, the rapid growth and development of inorganic-based, organic-based, composite-based, and carbon-based nanoparticles have resulted in numerous research toward nanoparticle polymer composite fibers, where multifunctional nanoparticles are dispersed within a single microscale fiber.[7] The enhanced properties,

including but not limited to mechanical durability, thermal conductivity, thermal insulation, chemical durability, and biocompatibility, began to broaden the applications of polymer fibers.[8–10]

1.2.Continues Fiber Spinning Techniques

In general, fiber spinning can be divided into a few categories, including but are not limited to melt spinning, solution spinning, electrospinning, and microfluidic spinning (Figure 1). Melt spinning is a process that requires melted polymer to be either thermally drawn or mechanically extruded through a tool of the spinneret, followed by procedures of cooling, solidification, and collection.[11] The solvent-free setup and fast process make it one of the most cost-efficient and environmentally friendly methods for fabricating thermoplastic materials, such as nylon, olefin, polypropylene (PP), polyethylene (PE), and nylon.[12–14] Solution spinning is often used for polymers that would quickly degrade before melting. In this method, a polymer is first dissolved in a solvent, followed by extrusion through a spinneret before continuous collection and post-treatment. Subcategories of solution spinning are dry-, wet-, and dry-jet wet spinning methods, which differ in the fiber solidification strategies via either gaseous air or liquid non-solvent. In dry spinning, the fiber is solidified as the solvent is dried after existing the nozzle. Usually, a low boiling temperature solvent, such as dichloromethane (DCM), with a boiling temperature of 39.6 °C and is chosen for fast fiber collection. This method is used to produce acetate, triacetate, modacrylic, and spandex fibers. In wet-spinning, the spinning dope travels through a coagulation bath where the solvent-nonsolvent exchange process takes place; the diffusion of the non-solvent in polymer/solvent solutions results in the precipitation of the

dope into gel fibers. This method is used in the production of polyimide (PI), aramid, and rayon fibers.[15,16] Dry-jet wet spinning combines dry- and wet- spinning processes, where dissolved polymer solution goes through an airgap before entering the coagulation bath. The airgap distance improves the fiber drawability, leading to the higher orientation of the fiber polymer chains, which are essential for high-performance semi-crystalline polymers, such as polyacrylonitrile (PAN), poly(ether sulfone) (PES), and polyvinyl alcohol (PVA).[17]

For all methods mentioned above, the fiber gradually solidifies and is continuously collected before necessary treatment, such as washing, cold-stage drawing, hot-stage drawing, surface treatment, sizing, and annealing. Parameters, including post-treatment conditions, spinning dope viscosity, air-gap distance (only for dry-jet-wet spinning), drying temperature, coagulation solvent condition, and take-up speeds, are significant for fiber properties, such as glass transition temperature,[18] cross-section dimension,[19] crystallinity,[20] and nanoparticle/molecular orientation.[21,22] For example, in microfluidic fiber spinning, polymer precursors flow through a nozzle or multiple microchannels with manipulated laminar flows that can significantly influence the molecular or nanoparticle conformations. As a result, the benefits of this microchannel-involved, flow-assisted method include precise control over fiber formation dynamics, structures, and functionalities. Different from drying or solvent exchanging processes used in traditional fiber spinning methods, new spinning apparatus can incorporate more versatile solidification processes, such as photopolymerization reaction,[23] nonsolvent-induced phase separation,[24] chemical crosslinking reaction,[25] and ionic crosslinking reaction,[26]

which have been investigated with more flexible material choices. Furthermore, designing the microchannel dimensions and shapes makes it easier to achieve more delicate dimensional control over physical geometries (e.g., cross-sectional shapes) and chemical compositions (e.g., multimaterial inclusions), making it a widely used method for medical applications.[27]

Electrospinning utilizes the electrostatic force, unlike the melt, solution, and microfluidic spinning methods where polymer feedstocks are mechanically extruded from nozzles. Polymers are first dissolved in volatile solvents or melted during electrospinning before being subjected to a high-voltage or high-electric field. By overcoming the surface tension of the polymeric solutions (i.e., the threshold intensity), the hemispherical surface at the nozzle tip begins to elongate, forming a structure known as the Taylor cone. Through a series of procedures (e.g., jetting, solvent evaporation, and solidification), continuous or non-continues fibers with micron to nanometer scale are collected as a non-woven mat, different from previously introduced single fiber fabrication methods.[28]

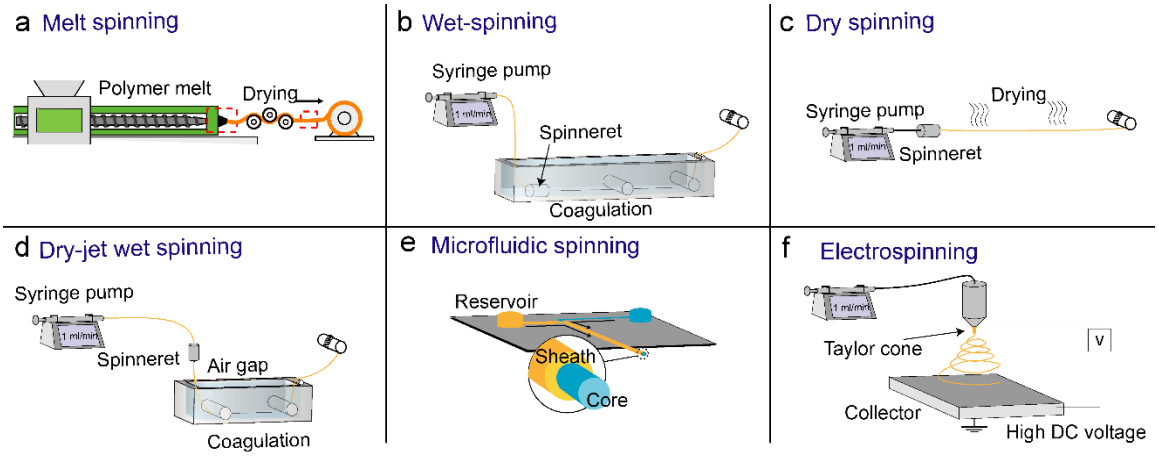

Figure 1. Common fiber spinning techniques. Adapted with permission from ref[29].

1.3.Multimaterial Composite Fibers

Since the 21st century, composite fibers have grown beyond the traditional uniform/homogeneous structures. According to Google Scholar, the number of publications containing the keywords “core-shell structure” and “fiber” has grown from 342 to 16400 every five years from 1995-2000 to 2015-2020 (Figure 2a). Other structures, including porous, coaxial, layer-by-layer, and segmented morphologies, show similar increasing trends based on Google Scholar keywords search (Figure 2b). This section briefly introduces each of the major micro-fiber structures with their applications ranging from energy storage devices, smart systems, wearable electronics, and healthcare to sustainable products.[30–34]

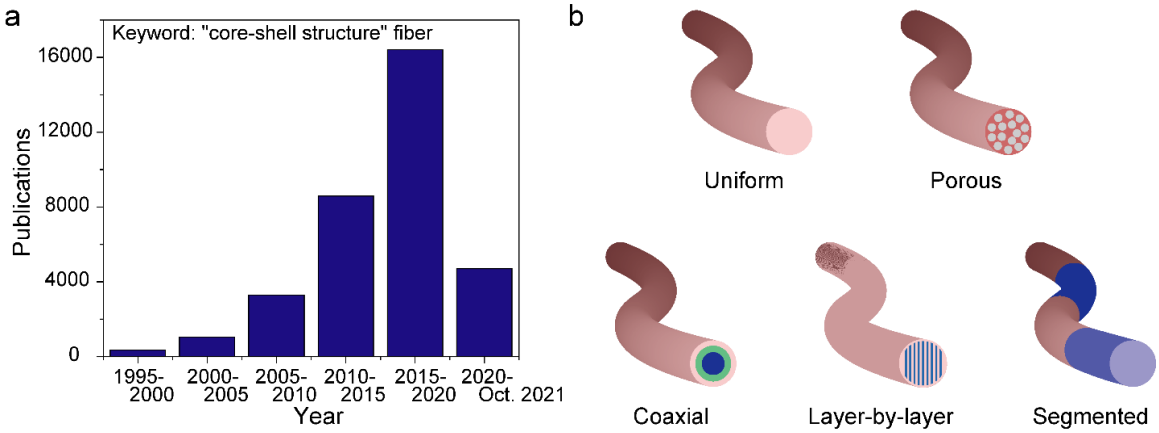

Figure 2. (a) Number of publications containing keywords “core-shell structure” and “fiber” based on google scholar search (1995-2020). (b) Examples of microstructures in fiber materials.

Porosity is a fiber characteristic pertaining to the surface area, reactivity, roughness absorbability, loading capability, mechanical stretchability/compressibility, and thermal

conductivity. The precise control over porosity is vital to applications across catalysis, sensing, absorption, energy storage, and tissue engineering.[35,36] Porogen use is one of the most common methods, and it can be primarily divided into solid,[37,38] gaseous,[39] solvent,[40–42] ionic liquid,[43] and oligomeric porogen.[44] Porous structures are obtained by mixing the porogen with polymer matrices, followed by etching, washing, or evaporating. For example, Anikeeva and her group have premixed filtered salt with polycaprolactone (PCL) for thermal fiber drawing. By rolling salt and PCL mixture around a polystyrene (PS) sacrificial core, hollow and porous PCL fiber were obtained with controllable micron-scale pore size for microchannel nerve guidance.[38] Nevertheless, material selection is tricky and must fulfill the following criteria. First, the porogen must be inert and does not react with the other ingredients. Second, the porogen must be compatible with the manufacturing method. For example, solid porogen is usually associated with melt processing, and porogen with a high boiling point is generally favored for solution spinning. Third, porogen must form a homogeneous and stable solution with the monomers and crosslinkers. Based on how well these criteria are fitted, the porogen method can create pores with well-controlled size and distributions. Nevertheless, the top-down approach requires multiple steps and sacrificial materials, which are not usually economically viable. On the other hand, spontaneous phase-separation is an alternative method for creating porous structures during solution spinning, which does not involve second-phase porogen materials. Both non-solvent induced phase separation (NIPS) and thermally induced phase separation (TIPS) result in polymer-rich and solvent-rich regions, forming nanometer to micrometer pores.[45–48] Another strategy via a simple combination of freeze-drying and

fiber spinning does not require porogen.[49–51] For example, Bai and his group recently showed that the solvent would crystallize and leave a porose structure after freeze-drying by applying a cold source during solution fiber spinning. Interestingly, the pores were aligned with preferential direction through optimizing the spinning parameters, resulting in enhanced mechanical properties.[52]

The coaxial structure is when a core material is covered concentrically by one or more layers of other materials, with each layer contributing a different functionality. Melt-based, solution-based, or microfluidic spinning techniques are often used with multiple inlets and outlet nozzles. The challenges include establishing stable interfaces between materials, choosing compatible solidification methods, and ensuring continuous fiber collection across layers. The primary benefits of coaxial design include broad and enhanced fiber functionalities. For example, Zhao and his coworkers have demonstrated a fiber spinning technique for fabricating supercapacitors.[53] From the electrodes to the electrolyte, the supercapacitor consists of four layers in a concentric structure, and all layers are simultaneously formed via solvent evaporation. Compared to other fiber supercapacitors with twisted or parallel structures, the coaxial fiber design enhanced volumetric capacity and dynamic stability.[53] Moreover, the coaxial system includes non-conventional designs, such as parallel hydrogel electrode cores covered with electroluminescent outer layer for brain interface communications,[54] multifunctional core fiber for magnetic resonance imaging,[55] and islands-and-sea structure for carbon fibers.[56]

The layer-by-layer fiber structure is defined by incorporating different material compositions parallel to the fiber axial direction. Cantrece fiber is the first-ever

commercially available layer-by-layer fiber and was introduced by Du Pont back in the mid-1960s. It consists of two adjacent nylon polymers. The fiber transforms into a highly coiled elastic fiber upon retraction due to the mismatch strain between layers.[57] By the same token, a typical application of layer-by-layer fiber is for bilayer actuation, where two adjacent materials show different responses to a stimulus.[58] Furthermore, the high interfacial area between the layers is another structural characteristic. Kenics static mixer (KSM) and the forced assembly processes can generate multilayered structures and have been developed for over decades.[59–62] Madero and coworkers have demonstrated that through using 7 KSM elements, the cell/hydrogel interface surface area of ~100 $cm^2\,cm^{-3}$ was achieved for higher cell alignment and more durable cell life.[63,64]

Unlike structures mentioned above, where constant cross-sections were maintained, segmented fiber has different materials continuously aligned along its axis, leading to unique multifunctionality. For melt spinning, thermal drawing of preformed, segmented raw materials[65] or in-situ surface patterning techniques have been developed.[66] For wet spinning, the most common methods are the Rayleigh instability technique,[67] switching input material types,[68,69] and physical segmentation during fabrication.[70] For example, Ho and coworkers have developed a scalable thermoelectric (TE) fabric composed of segmented fibers.[70] A continuous alternating extrusion process of p-type and n-type gel solution was used, followed by freezing gelation. Low loss modulus, G'', and storage modulus, G', were formulated to enable gel deformation under applied pressure. Through fiber weaving, p/n-type TE segments formed successive p-n junctions between hot and cold surfaces in fabrics.

1.4.Importance of Nanoparticle Orientation

1D and 2D nanomaterials possess unique anisotropic mechanical, electrical, thermal, and optical properties, leading to wide applications in energy storage systems, electronics, actuators, sensors, robotics, drug delivery, water treatment, tissue engineering, and composite manufacturing. 1D nanoparticles are in the forms of nanofibers, nanorods, nanotubes, and nanoribbons, while 2D nanoparticles are in the forms of nanoflakes, nanoplatelets, nanochips, and nanolayers. However, these nanomaterials fail to translate their theoretically predicted properties into practical applications due to nonuniform dispersion and lack of alignment. Therefore, it is highly desirable to achieve optimized assembly of 1D and 2D nanoparticles with well-manipulated orders at selective positions. For example, alignment of conductive nanoparticles can achieve significantly reduced scattering of electrons and phonons at matrix nanoparticle interfaces, resulting in higher conductivity compared to randomly dispersed nanoparticles, improving the performances of electrodes, supercapacitors, transistors, sensors, actuators, heat exchangers, thermoelectrical converters, optics, and biomedical devices.[71,72]

Due to the significance of nanoparticle orientation, needless to say, numerous methods have been explored. Torque experienced by the nanoparticles is one of the major driving forces of nanoparticle alignment. It can be generated either through internal or external factors. Internally, shear-induced alignment has been widely used for its facile mechanism, cost-effectiveness, and broad compatibility with established industrial methods.[73] During extrusion or spreading, nanoparticles experience a torque force due to the shear rate differences perpendicular to the elongation direction, and alignment occurs when the shear

rate exceeds the particle characteristic relaxation time. Another method of using internal hydrodynamic forces also shows efficient nanoparticle alignment. As droplets of solvent/nanoparticles evaporate, the pinned contact at the droplet edge develops an internal hydrodynamic flow which carries entrained particles to the air-liquid-substrate interface. Different nanoparticle alignment is achieved by controlling parameters, such as temperature, contract angle, velocity vector fields, and substrate morphology.[74] On the other hand, the external field using an acoustic field can pattern and align nanoparticles within a fluid medium. For a 1D pressure field, the neighboring trap distances are half of the acoustic wavelength, λ. The counter-propagating plane waves generate a standing-wave field, which leads to steep acoustic pressure gradients. These pressure gradients apply acoustic radiation forces on the suspended particles, thus manipulating them toward pressure nodes. Since nanoparticles have a higher density than the host fluid medium, the acoustic waves will force them toward the pressure nodes. On the other hand, the fluid medium with a lower density will move toward the antinodes.[75] The magnetic field has also been explored for nanoparticle alignment.[76–79] As the electrons circle around the circumference of nanoparticles (i.e., carbon nanotubes (CNTs)), they create a large orbital magnetic moment that results in the anisotropic susceptibility of CNTs. They are ultimately causing a magnetic field-induced torque that acts on the CNTs. The alignment direction of CNTs is parallel to the magnetic field as this configuration results in minimum magnetic energy.[80] However, similar to the electric field, both methods require the nanoparticles to be responsive to magnetic fields (e.g., FePt, Fe_2O_3, Fe_3O_4, CuO, FeCoV, Ni, TiO_2, and hematite) or electrical fields (e.g., CNTs, graphene nanoplatelets (GnPs), silver nanowires

(AgNWs), and $BaTiO_3$).[81] Table 1 summarizes a few alignment mechanisms with relevant materials and applications.

Table 1. Nanoparticle alignment mechanisms

Mechanism	Matrix	Nanoparticle	Application	Year	Ref
Shear flow	Epoxy	SiC/CFs	Mechanical reinforcement	2014	[82]
Shear flow	Hydrogel	nanoclay, CNT	Mechanical reinforcement	2020	[73]
Acoustic interactions	Epoxy	NCCF	Enhanced electrical conductivity	2020	[83]
Magnetic interactions	UV resin	Fe_3O_4, Al_2O_3	Mechanical reinforcement	2015	[84]
Magnetic interactions	Ecoflex	Silica, NdFeB	Actuator	2018	[78]
Electrical field	UV resin	GnPs	Sensing	2019	[71]
Freeze-drying	PEO	LAGP	Solid electrolyte	2019	[85]
Freeze-drying	PVA	Voids	Thermal insulation	2019	[86]
Self-assembly	Epoxy	Mxene	Sensing	2022	[87]
Self-assembly	PDMS	Cellulose	Photonic structure	2019	[88]
Dip coating	Epoxy	CFs	Sensing	2019	[89]

Abbreviations: NCCF, nickel-coated carbon fibers; LAGP, $Li_{1.5}Al_{0.5}Ge_{1.5}(PO_4)_3$; PEO, polyethylene oxide; GnPs, graphene nanoplatelets; CFs, carbon fibers;

Fibrous structure materials are known for their anisotropic properties for mechanical, electrical, and thermal applications.[90–94] For polymer nanoparticle composite fibers, controlling the filler particles' spatial orientation is more crucial for many applications. For example, the mechanical reinforcement efficiency (Equations 1 to 6) for nanoparticle polymer composite fibers is highly dependent on the Krenchel orientation factor (η_o) (Equation 3) which is calculated based the average angles between each nanoparticle axis to the fiber axis.[95,96]

$$E_c = E_m V_m + \eta_o \eta_f E_f V_f \tag{1.1}$$

$$\sigma_c = \sigma_m V_m + \eta_o \eta_f \sigma_f V_f \tag{1.2}$$

$$\eta_o = \frac{\int_0^{\frac{1}{2}\pi} I(\phi) cos^4 \phi d\phi}{\int_0^{\frac{1}{2}\pi} I(\phi) d\phi} \tag{1.3}$$

$$\eta_f = 1 - \frac{tanh\ (ns)}{ns} \tag{1.4}$$

$$n = \sqrt{\frac{2G_m}{E_f ln(\frac{2R}{d})}} \tag{1.5}$$

$$a = l/d \tag{1.6}$$

Here E_c, E_m, and E_f are the moduli for the composites, the polymer matrix, and the reinforcement fillers, respectively. σ_c, σ_m, and σ_f are the tensile strength values for the composites, the polymer matrix, and the reinforcement fillers, respectively. V_m and V_f are the volume fractions for the polymer matrix and the reinforcement particles, respectively. The length factor (η_f) is related to the mechanics of the composite phases and the distribution of particles. R and d are the quasi-radius and distance between nanoparticles.

The orientation factor (η_o) is calculatable by measuring the $I(\Phi)$ measurable via experimental procedures by a Gaussian or Lorentzian distribution as a function of Φ.[97,98] Different methods have been developed to measure the orientation factor depending on the samples and area of interest. Scanning electron microscopy (SEM), scanning tunneling microscopy (STEM), atomic force microscopy (AFM), and polarizing microscopy are particularly suitable for exposed nanoparticles, including thin coatings, microtomed sections, and fractured surfaces.[81] Combining with imaging analysis software, statistical analysis, and Fast Fourier Transform (FFT), Herman's orientation factor, f, as shown in Equation (7) can be estimated

$$f = \frac{3 < cos^2\delta > -1}{2} \tag{1.7}$$

where $< cos^2\delta >$ can be derived from FFT results.

Polarized Raman spectroscopy and X-ray diffraction (XRD) methods are often used in cases where the nanoparticles cannot be directly observed. For example, the intensity of the Raman shift at 1590 cm^{-1} of carbon-based nanoparticles, such as graphene, CNTs, and GnPs, show strong angular dependency with the angle between the polarized Raman light and the sample principal axis. By rotating the sample, the preferred alignment of the nanoparticles can be observed.[99] Similarly, for the XRD method, the alignment of carbon nanoparticles can be evaluated by plotting the integrated intensity along the 2θ angle along the azimuth angle. For example, two peaks can be observed for aligned CNTs, while no peaks can be observed for randomly orientated CNTs. For orientation degree, a smaller

full-width-half-maximum (FWHM) value corresponds to higher alignment, and vice versa.[100]

1.5.Additive Manufacturing as Tooling Engineering for Nozzle Design

Additive manufacturing (AM), also known as 3D printing, describes adding one layer of material upon another for products with designed 3D geometries and desirable compositions. This bottom-up fabrication process has been recognized by many as the fourth industrial revolution for numerous advantages over conventional top-down manufacturing.[101] The general printing procedure includes modeling, slicing, printing, and post-treatment. 3D printing has many advantages compared to traditional manufacturing techniques, including but not limited to (1) reduced iterative design opportunity costs, (2) decentralized production without logistic costs, (3) easily achieved complex and customizable geometry designs, and (4) limited waste materials. According to the American Society for Testing and Materials (ASTM), 3D printing can be divided into seven categories, including (1) material extrusion, (2) material jetting, (3) binder jetting, (4) sheet lamination, (5) vat photopolymerization, (6) powder bed fusion, and (7) directed energy deposition.[102] Depending on the print requirement, each 3D printing type has its own advantages and preferences.[103] For instance, photocuring-based methods include stereolithography (SLA), digital light processing (DLP), direct laser writing (DLW), and especially two-/multi-photon polymerization (2/MPP), offering higher spatial resolution (e.g., ~100 nm for 2/MPP) and better isotropic properties than other 3D printing approaches.[104] Extrusion-based methods, including direct ink writing (DIW) and fused deposition modeling (FDM), are derived from extrusion-based methods, such as filament

extruding or fiber spinning, making them highly cost-efficient with good accessibility (~$200 for FDM).[105] Inkjet-based MultiJet/PolyJet printing methods or electrohydrodynamic (EHD) printing allow pure nanoparticle deposition and multi-material compatibility.[106] Powder bed fusion (PBF)-based methods of selective laser sintering (SLS) and selective laser melting (SLM) utilize high-intensity power lasers primarily suitable for metal processing (e.g., steels, titanium, nickel-based, cobalt-chrome, and aluminum alloys).[107]

Manufacturing opportunities that were once limited by experimental setups are now open due to the marketization of 3D printing; researchers can design and rapidly prototype their printhead (i.e., spinneret) with highly customizable features. The first advantage is that the fast iterative design cycle enables material property-driven design rather than design-driven material property. This rapid prototyping function results in more extensive material selection ranges. For instance, nozzle jamming is one of the main limitations towards achieving the theoretical packing density for high nanoparticle-loaded fiber. Nozzle geometries, including diameter, extrusion length, and boundary faucet designs, all contribute to the nanoparticle concentration threshold, and their modifications are expensive and time-consuming. By willfully controlling these parameters through 3D printing, a larger threshold could be achieved.[108,109] The second advantage of 3D printing tooling engineering is based on its more versatile geometry designs. As previously mentioned, 3D printing can achieve detailed structures, such as undercuts, overhangs, voids, and complex internal geometries, with a range of feature resolutions depending on the printing mechanism (i.e., 0.1 μm for 2PP, 0.03-50 μm for EHD, 10-200 μm for SLA,

and 50-500 μm for FDM).[29] This provides the necessary tools for creating property-driven parts for broader processing needs, such as co-axial nozzles and multi-material nozzles. Table 2 summarizes a selection of fiber microstructures enabled with different nozzle designs through various 3D printing techniques.

Table 2. 3D printing-facilitated nozzle designs

3D printing technique	Nozzle Material	Microstructure	Application	Year	Ref
Polyjet	VeroClear, Agilus	Vertically aligned SiC fiber	Isotropic swelling	2020	[110]
SLM	Stainless steel	Coaxial	Cell growth	2014	[111]
SLA	Commercial resin (CLEAR PLGPCL04)	Segmented liquid droplet	Soft actuator	2018	[112]
SLA	Commercial resin (HTM140)	Segmented	Soft robotics	2019	[68]
SLS	Chrome-Cobalt alloys	Coaxial	Mechanical reinforcement	2021	[113]
DLW	PDMS	Coaxial	Cell size bio-compatible fiber	2021	[114]
2PP	Commercial resin (IP-S)	Micro droplets	Gas dynamic virtual nozzles	2022	[115]

1.6.Strategies to Utilize 3D Printing for Nanoparticle Morphology Control

This thesis aims to utilize 3D printing as a tooling method to simultaneously achieve microscale nanoparticle patterning and nanoscale nanoparticle alignment. Two types of nozzle designs, concentrical and layer-by-layer, and four chapters, namely, (1) coaxial nozzle design for multi-material extrusion, (2) coaxial nozzle design for nanoparticle alignment, (3) layer-by-layer nozzle design for nanoparticle patterning, and (4) layer-by-layer nozzle design for nanoparticle alignment have been included in this dissertation. This thesis also investigates the process-structural-property relationship of polymer nanocomposite fibers with some demonstrated applications, e.g., sensors, electrically conductive fibers, thermally conductive fibers, and mechanically reinforced fibers.

CHAPTER 2

MULTIMATERIAL FIBER SPINNING WITH COAXIAL STRUCTURE FOR VOLATILE ORGANIC COMPOUNDS SENSING

2.1.Introduction

The first step of exploring 3D printing as a tooling method for composite fiber spinning is to accomplish the multi-material composite structure. Out of many designs, the coaxial structure has been widely explored for its multifunctionality generated due to the multimateiral compatibility between each of the many layers. For example, Chen's group from Nanyang Technological University published their work on coaxial patterned fiber as asymmetric supercapacitors using a multichannel nozzle.[53] The multi-material fabrication method shows several advantages compared to the traditional parallel and twisted structures, including superior electron transfer, faster ion diffusion, and a more dynamically stable structure within the electrodes. Furthermore, the single-step extrusion-based process improves the interfacial delamination issues compared to the traditional layer-by-layer fabrication method. With a similar design concept, a nozzle has been customized (Figure 3a) and 3D printed (Figure 3b) with diameters of the inner, middle, and outer outlets as 1 mm, 3 mm, and 5 mm, respectively. The wall thickness is controlled at 0.5 mm. These three channels are separated from each other inside the spinneret and only fuse into a single strand after existing the nozzle. Three concentrical outlets were designed with a 0.5 cm increment in length from inner to outer layers to ensure a distinct layer separation. As a result, this multichannel nozzle can simultaneously accommodate three material types within one individual fiber (Figure 3c).

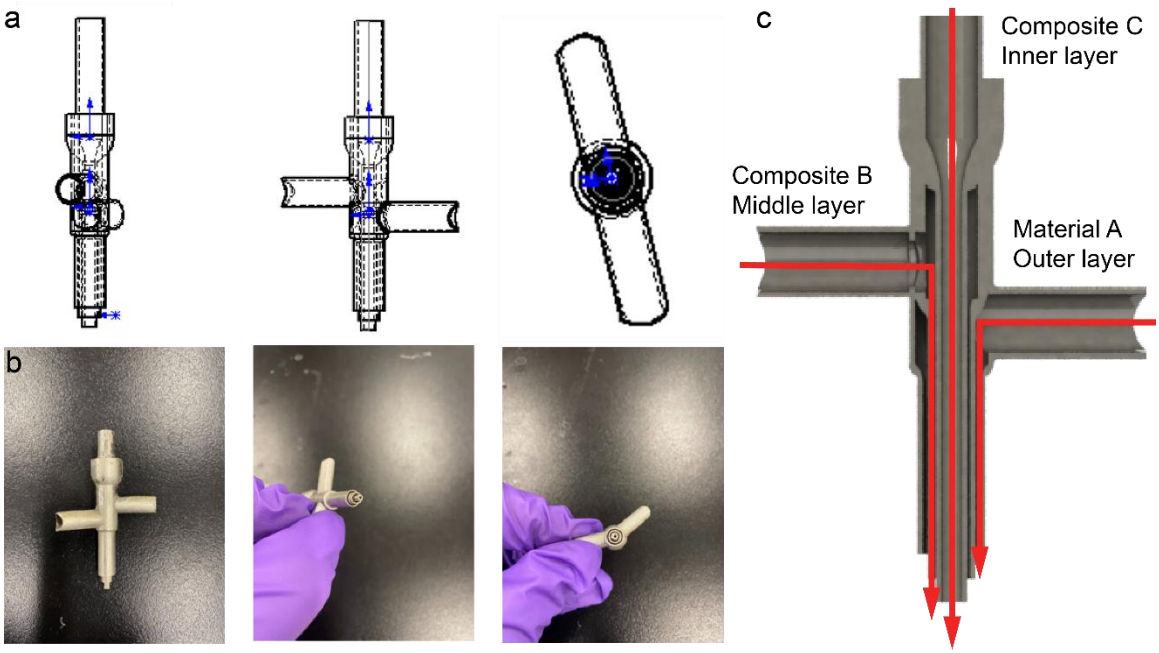

Figure 3. (a) Solidworks sketch of the multi-channeled spinneret. (b) 3D printed spinneret using 3D laser sintering. (c) Internal spinneret structure for multi-material extrusion.

One of the applications that could benefit from multi-material structure fibers is the detection of volatile organic compounds (VOCs), which is vital to numerous applications, such as long-term exposure to health risks,[16,116–118] environmental protection,[119,120] and control of various chemical processes.[121] Many attempts have successfully demonstrated portable chemiresistive devices with metal oxide semiconductors.[122–127] In particular, when nanostructured, their detection capabilities to analytes could reach a few parts per billion (ppb), with a fast response time.[128] As a result, they are ideal for biological applications, such as breath and respiratory diagnostics.[129] Nevertheless, the high sensitivities in conventional metal-oxides are more often coupled with high operating

temperatures and low environmental stability, limiting their application in multifunctional devices,[130–132] especially due to the low survivability of the rigid system under complex dynamic or fatigue conditions. As a comparison, conductive polymer nanoparticle composites demonstrate stable performances under extreme conditions,[133] display high manufacturability with scalability,[134–136] and satisfy specific requirements of wearable electronics.[137,138] Their gas sensing functionalities, based on the Flory-Huggins interaction parameters between solvents and polymers, have also been investigated with various polymer matrices and nanoparticles.[139–141] However, the main performance-limiting factor is their low sensitivity, usually in the range of several parts per thousand to a few hundred parts per million (ppm).

Increasing the specific surface area is an efficient method to increase sensitivity, such as macroscale helical structure[142], microscale scaffolds,[143] and nanoscale nanofibers.[144] Herein, a multilayered polymer nanoparticle composite sensor was fabricated with a dry-jet-wet fiber spinning method (Figure 4a). Each layer consists of different composites and functionalities. Through controlling the rheological behavior of the inner layer's plasticized thermoplastic polyurethane (TPU), a spontaneously assembled and continuously formed hollow-core fiber enables in-situ VOC detection during gas transportation. The porous structure (e.g., pore size, porosity) is optimized with a controlled coagulation rate to guarantee efficient VOC diffusion via the inner layer. The chemiresistive middle layer containing graphene nanoplatelets (GnPs) and carbon nanotubes (CNTs) incorporates resistive sensitivity changes upon VOC exposure. More importantly, the pore-free outer layer serves as protective packaging, demonstrated with

high mechanical flexibility and sensing stability during and after multiple strain deformations (Figure 4b). The coupled piezoresistive behavior also allows the detection of uniaxial deformation during VOC and pressure sensing applications.

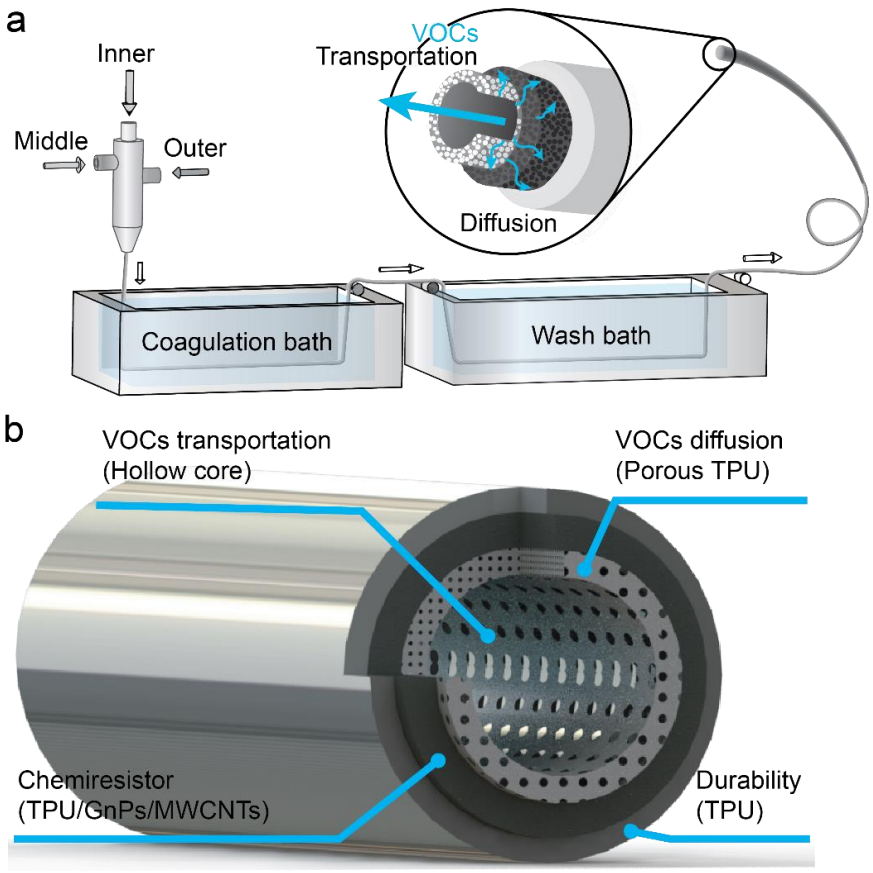

Figure 4. Schematics of (a) dry-jet-wet fiber spinning process and (b) multilayered composite VOCs sensor.

2.2.Experimentation and characterization

Materials*:* Methylene diphenyl diisocyanate (MDI)-based polyether TPU, Elastollan® (1185A), and plasticized MDI based polyester TPU, Elastollan® (Soft35) were kindly provided by BASF, Lemförde, Germany. Industrial-grade commercialized MWCNTs,

NC7000, with an average diameter of 9.5 nm and length of 1.5μm (Nanocyl, Belgium), were used as received. GnPs, methanol (HPLC, ≥99.9%), ethanol (ACS reagent, ≥99.5%), xylene (reagent grade, ≥98.5%), hexane (reagent grade, ≥98.5%), dimethylformamide (DMF) (anhydrous, ≥99.8%), and silver conductive paste (1.59 μΩ cm) were purchased from Sigma Aldrich, Missouri, USA. Polydimethylsiloxane (PDMS, Sylgard 184) was purchased from Dow Corning, Michigan, USA.

The dry-jet wet spinning of 1-Phase*x*%CNTs: 20 wt% of Soft35 was first dissolved in DMF (50 ml) at 90 °C for 2 hours. Desired GnPs were added and stirred for 1 hour at room temperature, following tip sonication at 60% amplitude for 10 minutes, with 5 seconds on and 5 seconds off. Desired MWCNTs were added and stirred for 1 hour, followed by 10 minutes of tip sonication under the same condition. Next, the spinning dope was degassed in a vacuum oven for 30 mins and sonicated in a sonication bath for one hour. After that, the spinning dope was transferred to a stainless-steel syringe and ejected with an air gap of 0.5 cm at a 2 ml min^{-1} rate into a 3000 ml coagulation bath containing 80:20 volume ratio of methanol ultra-purified water. Lastly, the resulted fiber was washed in ultra-purified water overnight and dried at 60 °C for 48 hours.

The dry-jet wet spinning of 4-Phase95%CNTs: 28 wt% of 1185A and 20 wt% Soft35 were mechanically stirred in DMF (100 ml) at 90 °C for 2 hours, respectively. They were degassed in a vacuum oven for 1 hour and were transferred to two stainless steel syringes. The 1185A solutions, optimized middle layer spinning dope (Soft35 with GnPs and MWCNTs dispersions), and Soft35 solutions were connected to the spinneret's outer, middle, and inner layer channels, respectively. All three spinning dopes were injected at

optimized rates of 2.0, 1.5, and 1.5 ml min^{-1} into the optimized coagulant (with a 0.5 cm air gap between the spinneret and coagulant), followed by 12 hours of washing in an ultra-pure water bath. It should be noted that a hollow core was formed as the fiber entered the coagulation bath, where it gradually gelled before solidifying at 60 °C in air for 48 hours.

VOCs sensing tests: All fibers were cut into 2 cm segments for VOCs sensing and were connected to copper wires with silver paste applied to both ends, followed by 1-hour drying at 60 °C. For vapor flow sensing, the 4-Phase95%CNTs fiber was connected to 1/8 nylon tubes on both sides, and PDMS was used for tight sealing of the sensors. One end of the fiber was sealed off with PDMS for pressure sensing, while the other was connected to a 1/8 nylon tube. The core was kept unblocked for vapor transportation. The organic solvent vapor was first generated from a gas bubbler with controlled dry clean air flowrates, V_{VOCs}, via a flowmeter (line A), as shown in Figure 10a. The solvent mass loss, m_{loss}, was separately calibrated with controlled V_{voc} for 30 minutes (i.e., VOCs of methanol, ethanol, and hexane) and 1 hour (i.e., VOC of xylene). Next, the organic solvent-containing gas flow was diluted with pure dry clean air, V_{air}, (line B), and the total gas flow through the 4-Phase fiber was controlled at 200 ml min^{-1}. Different gas flow concentrations were obtained by varying the ratios between V_{air} and V_{VOCs}. The organic vapor concentrations were calculated following Equation 2.1, in the unit of mg m^{-3} before being converted to parts per million (ppm, volume/volume) at standard temperature and standard pressure with associated molecular weights:

$$C_{VOCs} = \frac{m_{loss}}{V_{air} + V_{VOCs}} \quad (2.1)$$

Characterization: The electrical response was measured using a two-probe method with a digital multimeter (DMM7510, Keithley). Rheological behavior and uniaxial strain were conducted using Discovery HR-2 (TA instrument). A 40 mm, 2° Peltier cone plate with a 100 µm gap at 25 °C was used for viscosity and oscillatory tests. A scanning electron microscope (SEM) was employed for microstructural morphology analysis using XL30 ESEM, Phillips. To increase conductivity, all samples were coated with 15 nm of gold/palladium (Au/Pd).

2.3 Rheological Control for Self-Induced Hollow Core

Both TPU Soft35 and 1185A were used due to their different affinities to non-solvent during coagulation, polymer chain length, and macromolecular cross-linking density. As mentioned in the experimentation section, a pure Soft35 polymer solution, an MWCNTs/GnPs/Soft35 mixture, and a pure 1185A polymer solution were injected into the inner, middle, and outer spinneret inlet, respectively. As the spinning dope mixtures exited the spinneret, they first went through an air gap to facilitate interfacial fusion between these layers. Then, it entered a coagulation bath where the solvent and non-solvent experience a liquid exchange process due to their concentration gradient, resulting in polymer chain precipitation owing to their limited solubility in the non-solvent coagulant. TPU is known for its high porosity structure due to nuclei growth, essential for forming radial diffusion pathways.[145] Optimized coagulant, with ultrapure water to methanol

volume ratio of four to one, was selected from five different mixtures according to structural porosity, surface porosity, and spinnability (Figure 5).

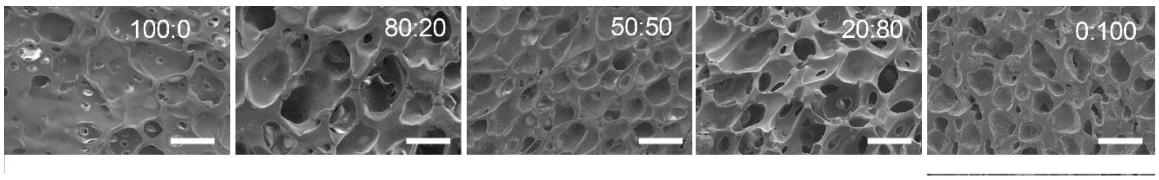

Figure 5. SEM images of 20wt% Soft35 TPU with water to methanol ratios of 100:0, 80:20, 50:50, 20:80, 0:100. Scale bars are 50 µm.

A self-induced hollow core was observed after washing and drying the fiber, similar to previously reported hollow polymer spheres.[146] SEM images confirm the multi-layered structure: the hollow core, a porous TPU inner layer, an MWCNTs/GnPs/TPU middle layer, and a pore-free TPU outer supporting layer (Figure 6a_1). The pores in the middle layer were non-uniform, with a diameter ranging from 20 µm to 2 µm (Figure 6a_2). This variation was likely the result of the additional MWCNTs and GnPs that were high in contrast in aspect ratios and surface areas, 312 and 150 m^2 g^{-1}, respectively,[147,148] causing non-uniform nucleation during polymer precipitation. The denser polymer structure of the outer shell containing the TPU of 1185A was likely the result of a faster solvent exchange process caused by the higher solvent concentration gradient and higher polymer chain entanglements, as observed in the high viscosity of its spinning dope. In contrast to the middle layer, the pores in the inner layer showed a more uniform distribution with an average pore diameter of 12 ± 3.4 µm, which could result from a slower solvent concentration gradient than the outer layer polymer channel (Figure 6a_3) and lower molecular interactions. Although larger solvent exchange channels were observed across

the radial direction in the outer layer, the surface was observed to be pore-free due to the polymer gelation and skin formation during coagulation,[44] sufficiently preventing the surrounding environment effects (e.g., moisture, contamination, dust) from the VOC influences (Figure 6a$_4$). The inserted image demonstrates the flexibility of the sensor. Under a 180° buckling with a centimeter-scale bending radius, no collapse of the hollow core layer was observed.

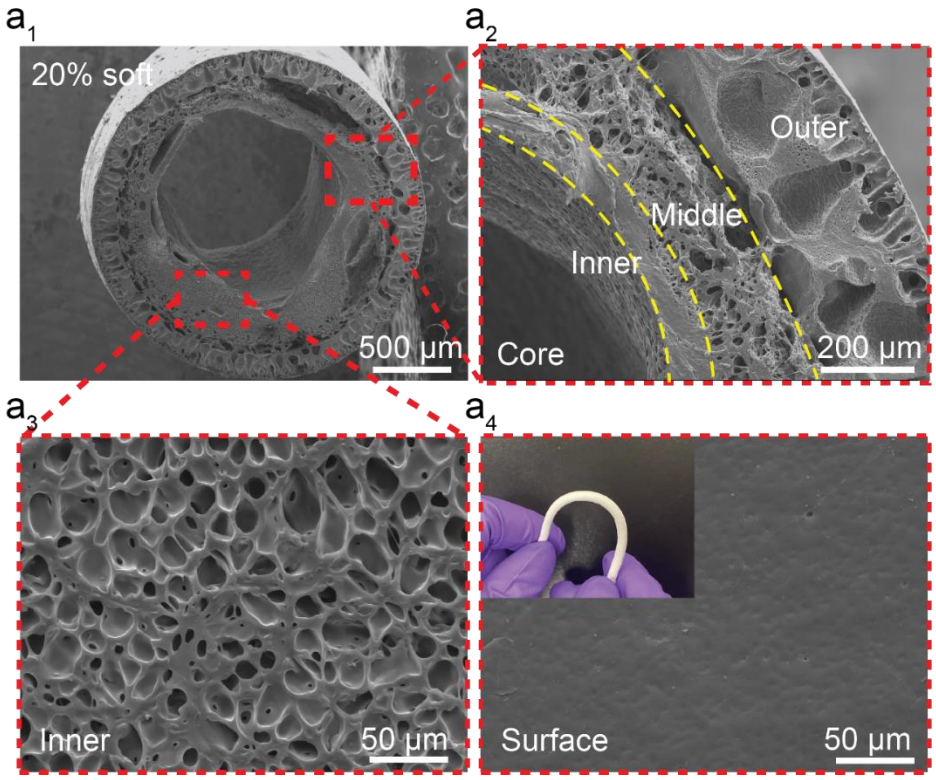

Figure 6. Fiber morphology characterization. (a$_1$) The cross-section of 20wt% TPU Soft35 with magnified images showing (a$_2$) across layers, (a$_3$) interior surface, and (a$_4$) exterior surface morphology with the inserted photo showing the fiber flexibility.

The formation of the self-induced hollow core was dependent on the rheological behavior of the spinning dope (Figures 7a and 7b). For polymer gels with concentrations of 40 wt% TPU Soft35 and 50 wt% TPU 1185, no continuous core formation was observed. This is likely due to the higher degree of polymer chain entanglement, resulting in higher storage and loss moduli and hindering their tendency to migrate beyond the polymer-solvent system (Figure 7c). For the 20 wt% TPU Soft35 solution, its lower storage and loss moduli favored polymer chain movement driven by the solvent concentration gradient. As a result, during the coagulation process, the polymer chains would migrate toward the more mechanically robust middle layer (i.e., TPU composites reinforced by the MWCNTs/GnPs), resulting in the formation of a hollow core.

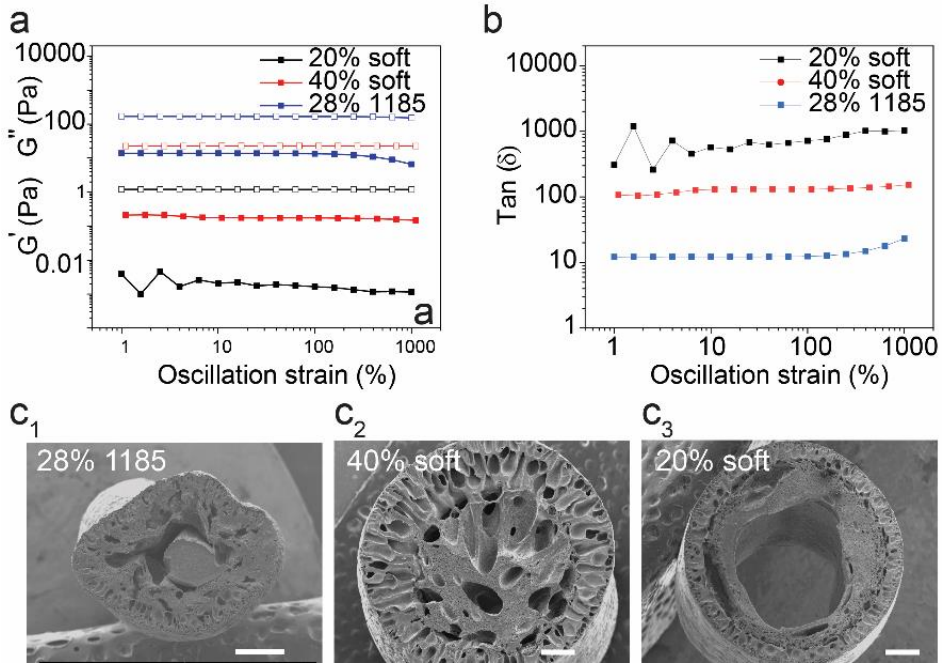

Figure 7. (a) The relationship between storage and loss moduli with increasing oscillation strain for 20 wt%, 40 wt%, and 50 wt% TPU Soft35, and (b) their corresponding tan delta

values. The cross-section SEM image of the multi-layered fiber with (c_1) 28 wt% 1185, (c_2) 40 wt% Soft35 and (c_3) 20 wt% Soft35 as the core layer.

2.4. Optimization of the Middle Chemiresistive layer

The composition of the middle sensing layer is critical to the sensor's sensitivity. It was optimized based on electrical conductivity, fiber spinnability, mechanical durability, and chemiresistivity. 3wt% of MWCNTs was chosen as the filler concentration for its high conductivity and minimum impact on the flexibility of the TPU polymer chains.[149,150] By maintaining a total of 3 wt% nanoparticles, combining *x* wt% of MWCNTs with (1-*x*) wt% of GnPs, named 1-Phase*x*%CNTs, showed a similar synergistic effect for enhanced electrical conductivity in single-phase fibers (Figure 8a).[151,152] As expected, the tan delta values of all solutions were inversely proportional to their conductivities, with 1-Phase95%CNTs having the lowest value at 100 Pa (Figure 8b). The more elastic behavior of the spinning dope was likely due to its improved nanoparticle dispersion quality, as the elastic nanoparticles more uniformly disrupted the viscoelastic polymer chains. The unique 2D geometry of the GnPs has shown a positive influence on preventing MWCNTs re-agglomeration,[49] while the tortuous shape of MWCNTs prevents GnPs from re-stacking (Figure 9).[47] Mechanical strength is crucial for freestanding sensors, especially with inline transportation applications. Uniaxial tension testing was conducted for the 1-Phase40, 65, 80, 95, and 100%CNTs fibers with a constant linear rate of 500 μm s^{-1}. The tension displacement was maximized to instrumental limitations, and all fibers showed extreme high stretchabilitiy with demonstrated strain values of >600% without any breakage

(Figure 8c). Based on models such as the Halpin-Tsai and the Mori-Tanaka,[153,154] the improved dispersion quality and high CNTs content contributed to the highest Young's modulus and strength.

The VOC sensitivities of all 1-Phase*x*%CNTs fibers were tested under continuous methanol vapor flow at 420 ppm for 15 mins. The response was calculated by dividing the change in resistance (ΔR) over the initial resistance (R_0). The 1-Phase95%CNTs fiber showed the highest response among all fibers. The mechanisms of polymer composite VOC sensing are well recognized. They are mainly attributed to the swelling of a polymer matrix that disrupts the electron pathway.[142,155] At the same time, a small portion of the analyte detection is contributed by the MWCNTs adsorption of organic molecules mainly based on hydrogen bonding, electrostatic interactions, and hydrophobic interactions.[123,156] All reaction curves showed three segments, including an initial reaction range (~0 to 250s), a linear reaction range (~250 to 450s), and a saturation reaction range (~450 to 900s) (Figure 8d). The slower rate of change in the initial reaction range was likely a result of methanol adsorptions onto the surface-exposed MWCNTs. The shape of the curve showed a strong resemblance to relative pressure versus surface area in Brunauer-Emmett-Teller (BET) surface area analysis on porous polymer composites,[157] which could further correlate ΔR with methanol diffusion rate. The remaining curve was similar to polymer swelling behavior with a linear swelling range following a plateau region, which could result from equal adsorption and desorption rates and the reaching of a maximum swelling degree.[155]

Based on low percolation threshold, shear-thinning behavior, high mechanical stiffness, and high VOC sensitivity, TPU Soft35 matrix with a total of 3 wt% of nanofillers composed of 95% MWCNTs and 5% GnPs was selected as the composition for the middle layer. Therefore, the overall multi-layered sensor consists of four phases: a hollow core, a porous plasticized TPU Soft35 inner layer, an MWCNTs/GnPs/TPU Soft35middle layer, and a polyether TPU 1185A based outer supporting layer, which will be named as 4-Phase95%CNTs.

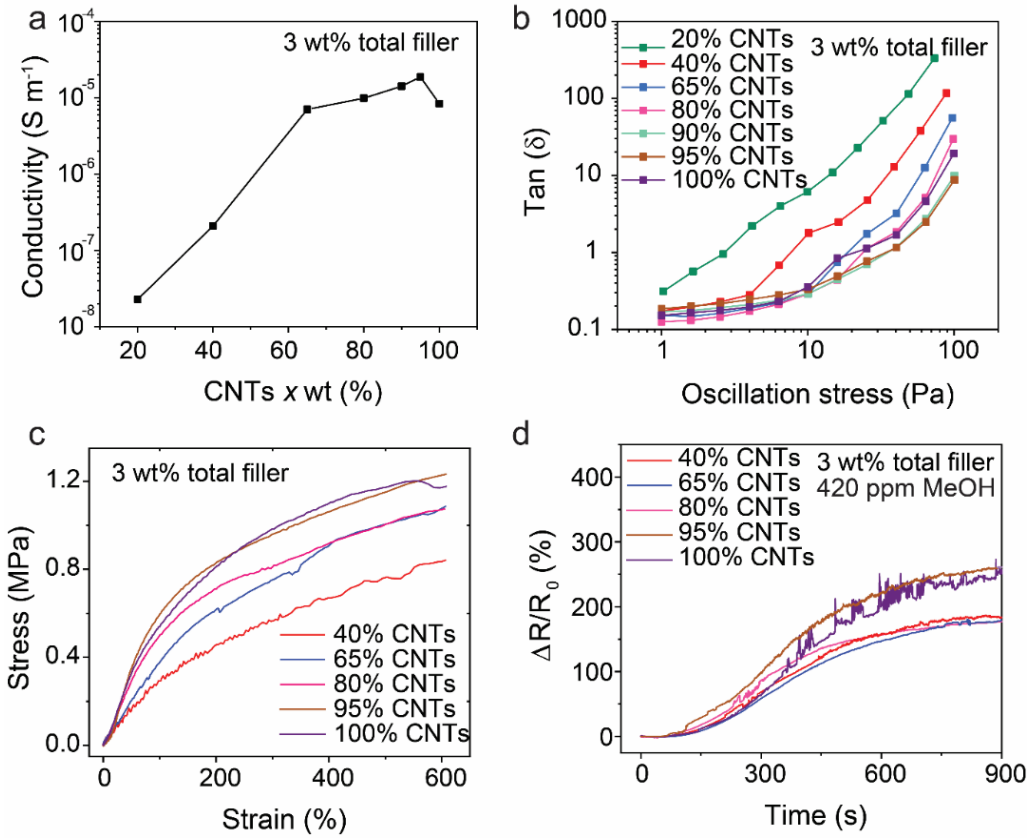

Figure 8. Optimization of the middle sensing layer. (a) The electrical conductivity of 1-phase fibers with 3 wt% nanofillers at different ratios of MWCNTs. (b) The tan delta values for the spinning solution under stress sweep oscillation. (c) Uniaxial stress and strain curves

for 1-Phase*x*%CNTs fibers, and (d) electrical responses for 1-Phase*x*%CNTs fibers under 420 ppm of methanol.

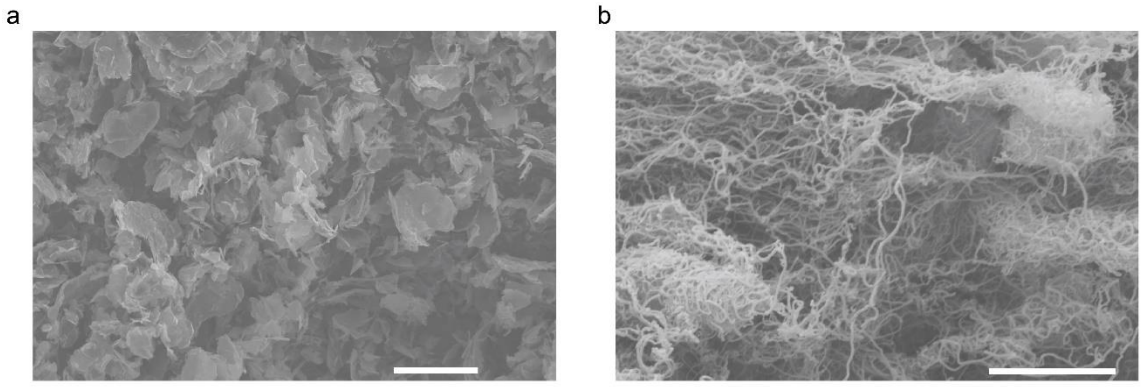

Figure 9. SEM images of (a) GnPs and (b) multi-walled CNTs with scale bars of 2 µm.

2.5 Multilayer Multimaterial VOCs Sensor

The properties between 1-Phase95%CNTs and 4-Phase95%CNTs fibers were compared in VOC sensitivity, pore distribution, humidity resistance, and temperature resistance. In terms of chemiresistivity, despite equal nanoparticle loading, the response of the 4-Phase95%CNTs fiber was approximately 600% higher than that of the 1-Phase95%CNTs fiber, and the response time was also faster during both methanol vapor absorption and desorption (Figure 10a). Axial cross-sectional SEM images of the 4-Phase95%CNTs fiber show optimized porosity, ensuring both efficient diffusion rate and a high surface-area-to-volume ratio, which are closely related to sensitivity (Figure 10$b_{1\text{-}2}$).[142] As a comparison, SEM images of the 1-Phase95%CNTs fiber showed drastic skin formation due to fast coagulation (Figures 10$b_{3\text{-}4}$)

The ability to operate under different humidity and temperature environments is one of the key requirements for inline measurement systems. The effects of humidity level on both 1-Phase and 4-Phase sensors are shown in Figure 10c with a homemade set-up shown in the insert schematic. The pores-free surface of the outer TPU layer (Figure 6a$_4$) in the 4-Phase95%CNTs sensor dramatically reduced water absorbance of the interior porous layer, which showed a 0.8% change in resistance from 30% to 65% humidity level in 40 minutes (Figure 10c). Meanwhile, the unprotected 1-Phase95%CNTs sensor showed a 4.6% change in resistance with an abnormal peak profile resulting from non-uniform adsorption. The recovery speed is also faster in the multi-layer than in other fibers, where it retained 99.94% of the initial response in under 45 minutes. On the contrary, the 1-Phase fiber only retained 25% of the initial response over 90 minutes. For temperature dependency, the 4-Phase95CNTs% sensor shows high reversibility at 2 hours of relaxation across a temperature gap of 25 °C (Figure 10d). After the fiber was stabilized for two cycles, the percentage changes in the resistance values were -0.511, -0.511, and -0.512%, respectively, at 50 °C. The stable behavior at this temperature range allows accurate calibrations for practical application.

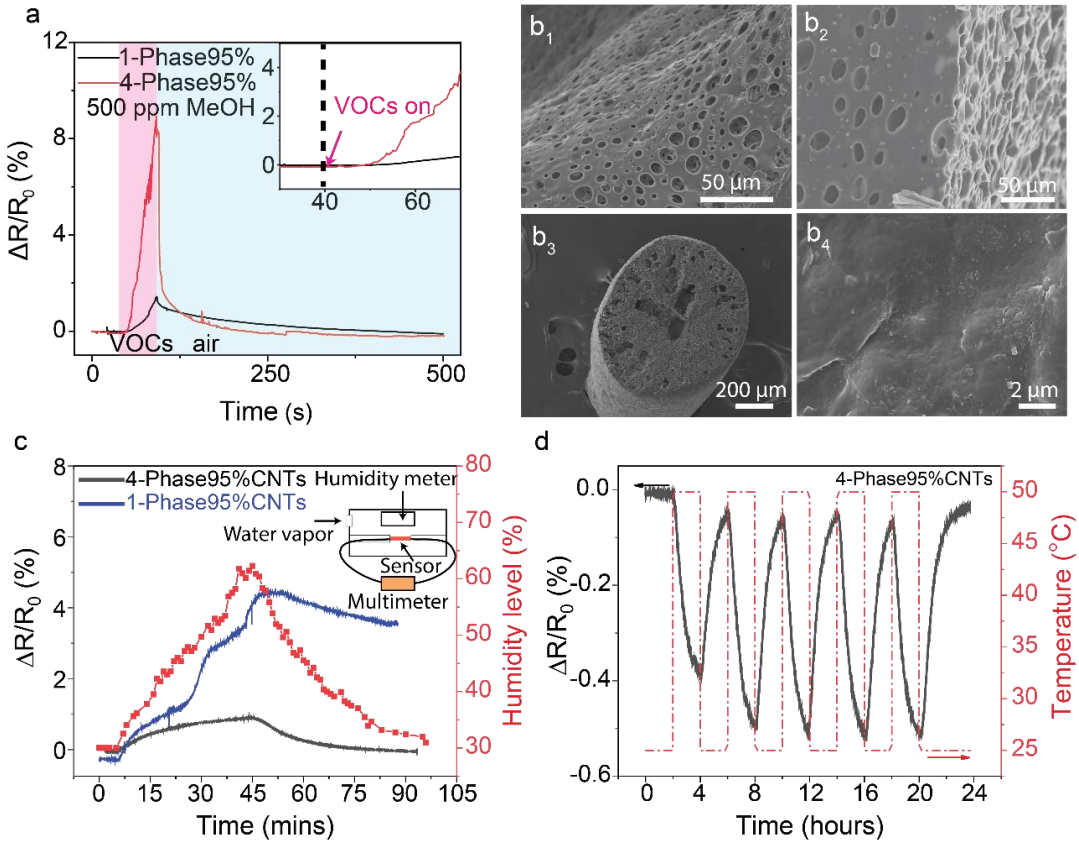

Figure 10. VOCs sensor comparison between the 1-Phase95%CNTs and 4-Phase95%CNTs sensors in (a) chemiresistive response, structure morphologies of (b_{1-2}) 1-Phase and (b_{3-4}) 4-Phase fibers, (c) humidity influence on the electrical stability, and (d) cyclical temperature influence on 4-Phase95%CNTs.

2.6 Sensitivity and Selectivity of Multilayered VOCs sensor

Next, the sensitivity and selectivity of the 4-Phase95%CNTs fiber were tested based on the experimental set-up shown in Figure 11a**,** where alternating air with and without VOC vapors was transported directly through the fiber for inline measurement. Figures 11b_{1-4} shows the response of hexane, methanol, ethanol, and xylene, respectively, which were

selected from aliphatic hydrocarbons, alcohol groups, and aromatic hydrocarbons with different concentrations. After 30 seconds of resistance stabilization, different VOC concentrations at 200 ml min^{-1} were blown through the fiber for 30 seconds, followed by 200 ml min^{-1} air purging. Obviously, the resulting resistance changes are proportional to the vapor concentrations, and each inserted image shows high linearities of the response from 30 to 60 seconds. Signal-noise ratio (SNR) was calculated based on the ratio between the response change and their electrical noise, and a minimum of 5 was determined as the threshold for a clear, differentiable signal. Based on this calculation, the LoD for hexane, methanol, ethanol, and xylene were determined at 200, 120, 120, and 15 ppm, respectively, and their corresponding SNRs were 6.9, 8.1, 11,4, and 20. Recovery time showed significant differences across solvent types. The recovery time for hexane, methanol, ethanol, and xylene at the LoD was 120 s, 180 s, 150 s, and 1300 s, respectively. Furthermore, the 4-Phase sensor showed high reversibility as the responses returned to initial levels for hexane at all concentrations and other VOCs at lower concentrations. The restored responses for 580 ppm of methanol, 530 ppm of ethanol, and 50 ppm of xylene were 2%, 3%, and 2.5% after one cycle, respectively. Polymer swelling is usually reversible with no breaking of the polymer chains, but the irreversible resistance at higher VOC concentrations, even after 8 hours, indicated that the structure of the conductive nanoparticle network was not reversible. This could result from the weaker van der Waal forces between the non-functionalized MWCNTs/GnPs and the polymer chains.

Overall, the 4-Phase95%CNTs sensor showed high sensitivities towards different types of solvent and had one of the lowest LoD for composite-based sensors. The sensitivity of our

fiber is not yet comparable to rigid and brittle devices composed of thin-film, metal oxide, graphene, or Mxenes-based sensors with LoD values of several parts per million or parts per billion. However, the LOD values of our fiber are still well below the regulatory limits of the Occupational Safety and Health Administration (OSHA), where the 8-hour time-weighted averages for hexane, methanol, ethanol, and xylene are 500, 200, 1000, and 100 ppm, respectively. Thus, our fiber sensors have broad applications for detecting potential solvent or chemical feedstock hazards in laboratories and chemical plants.

Based on the aforementioned sensing mechanisms and previous studies on the swelling degree between methylene diphenyl isocyanate (MDI)-based TPU with different types of organic solvents,[8,61] the 4-Phase95%CNTs fiber sensor showed different resistance changes and recovery time toward different groups of VOCs (Figure 11c). As the middle sensing layer is exposed to different types of solvents, the polymer matrix swells up, disrupting the conducting filler network and changing the electrical resistivity. The degree of swelling is related to the Flory-Huggins interaction parameter, X_{12}, which describes interactions between the solvent and the polymer following Equation (2.2)[89]

$$\chi_{12} = \frac{V_{vol} \times (\delta_{Tpol} - \delta_{Tsol})^2}{RT} \quad (2.2)$$

where R is the ideal gas constant, 8.314 J K^{-1} mol, T is temperature, V_{vol} is the molar volume of solvents, δ_{Tpol} is the solubility parameter for TPU, and δ_{Tsol} is the solubility parameter for solvents. Lower X_{12} values predict stronger interactions, resulting in a higher swelling degree which further correlates to the LoD as plotted in Figure 12.

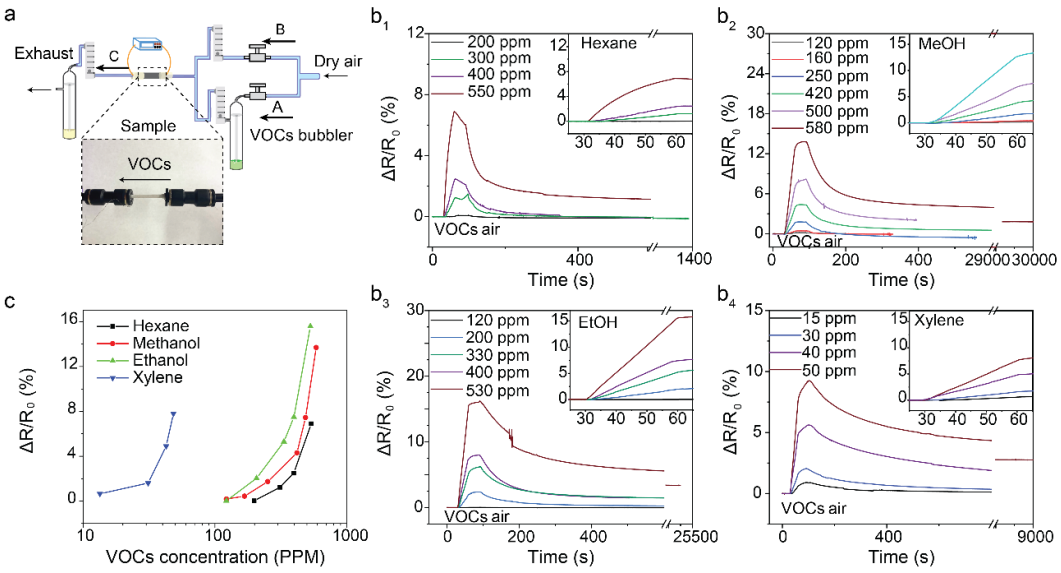

Figure 11. Sensing characterization of the 4-Phase95%CNTs fiber as VOCs pass through the hollow core. (a) A schematic of the experimental setup. ($b_{1\text{-}4}$) The response characteristics to hexane, methanol, ethanol, and xylene at different concentrations for 30 seconds. (c) Summarized relationship between output response and input vapor concentrations for different solvents.

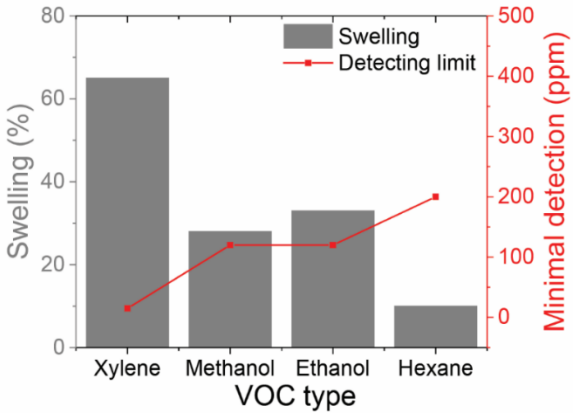

Figure 12. The swelling degree of the polymer under different types of solvents with their observed LoD.

2.7 Piezoresistive Sensing

The additional outer TPU layer also improves the sensor's mechanical stability, one of the crucial criteria for inline VOC sensors. For demonstration, the 4-Phase95%CNTs sensor was first investigated at 10% strain for 80 cycles with a strain rate of 0.1% s^{-1}. The stress and strain curves of six selected cycles are shown in Figure 13a. The Young's moduli of the first and last cycles were calculated to be 0.74 and 0.75 MPa, respectively, showing no decrease in the overall mechanical properties. The corresponding resistance change was also simultaneously recorded, and a decreasing trend was observed with increasing cycles (Figure 13b). The insert image shows a gradually increasing resistance tail at the end of each cycle, indicating a higher relaxation time is required for the electron pathways to restore their initial inter-bridging network. A similar cyclic stabilizing effect has also been observed for other piezoresistors.[158] The chemiresistive response before and after 80 cycles of 10% strain is shown in Figures 13c and 13d. After 5 minutes of 200 ml min^{-1} air for purging, 130 ppm of ethanol was blown into the fiber fixed on the tensile tester for 30 seconds, as shown in the experimental setup in Figure 14. Before any strain was applied, a gradual decrease in resistance was observed while the efficiency of each $\Delta R_x/R_{0\text{-}x}$ value compared to the first cycle gradually changed from 100% to 140%. After 80 cycles of deformation, the response was stable, and the cyclic efficiency increased from 100% to 120% (Figures 13c and 13d). Since the mechanisms of both the chemiresistive and piezoresistive behaviors are dependent on the network of MWCNTs/GnPs, it is not surprising that cyclic performance during VOCs sensing did not deteriorate but followed a similar stabilizing trend.

The electrical response was then investigated in the presence of both strain deformation and VOC vapors. The 4-Phase95%CNTs sensor was elongated with stepwise strains of 0%, 3.5%, 6%, 8%, 10%, 20%, 30%, and 50% at 0.25 Hz. The cyclic response of 130 ppm of ethanol was investigated at each fixed strain. Figures 13e and 13f show the overall responses where the baseline gradually increased due to mechanical deformation. Since both piezoresistive and chemiresistive properties depend on the nanofiller conducting network disturbance, an increase in mechanical deformation also resulted in a linear increase of the chemical response, which was fitted with a slope of 0.012 and an R-squared value of 0.96 (Figure 13). Furthermore, strain deformation could be measured based on the baseline of the VOC sensing cycles and could be further modeled based on the tunneling theory by Simmons.[159] Nevertheless, the stability of the response gradually decreased at approximately 30% strain and showed obvious degradation at 50% strain. This was likely due to the creep behavior of the polymer/nanoparticle network at long strain deformation. The decrease in the VOC response baseline could be further calibrated using the well-established piezoresistive models, such as the Nutting Equation, for the time-dependent electrical response.[160] Overall, the sensor shows strong mechanical flexibility and stability. It can also detect and measure the degree of mechanical deformation based on the response from both piezoresistive and chemiresistive behaviors.

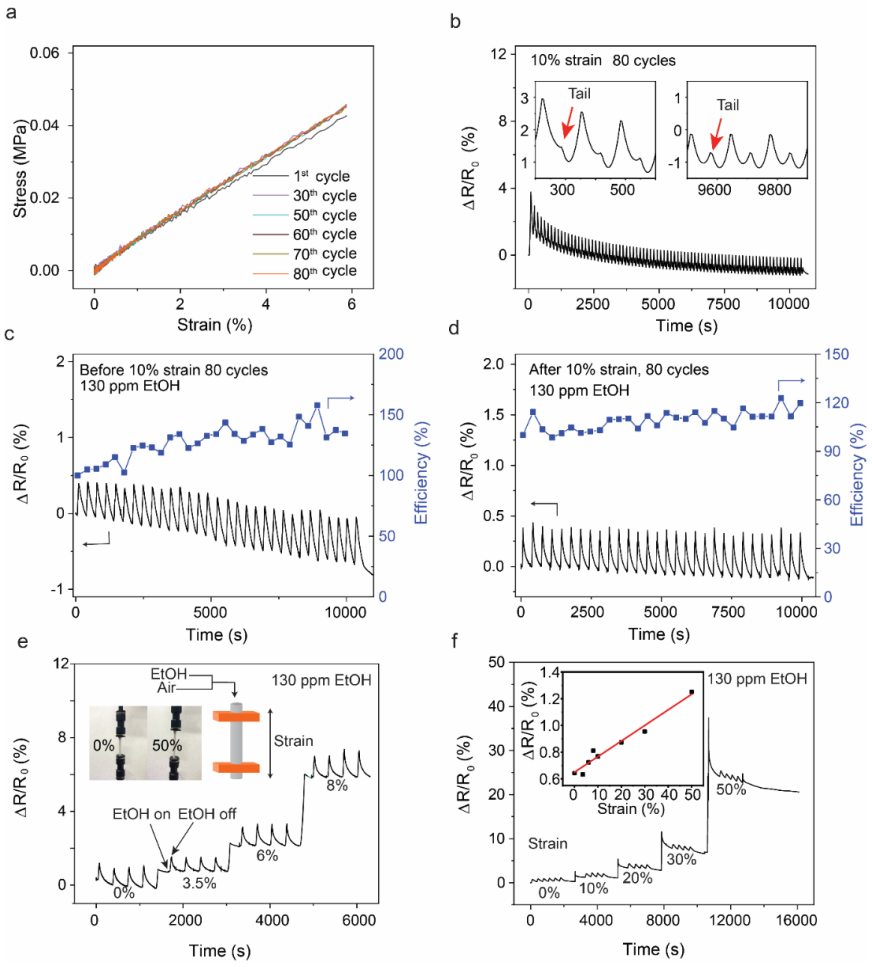

Figure 13. Chemiresistive behavior of the 4-Phase95%CNTs sensor under the influence of strain deformation. (a) Selected stress-strain curves of the 4-Phase95% fiber for 80 cycles at 10% strain, and (b) the corresponding piezoresistive behavior of the 4-Phase95%CNTs sensor with magnified beginning and end regions. Cyclic performance of the 4-Phase95%CNTs fiber (c) before and (d) after 80 cycles of 10% strain with 130 ppm of ethanol. Chemiresistive behavior as responses to 130 ppm ethanol flow during (e) 0% to 8% small strain and (f) 0% to 50% large strain with chemiresistor amplitude response increase linearly with strain.

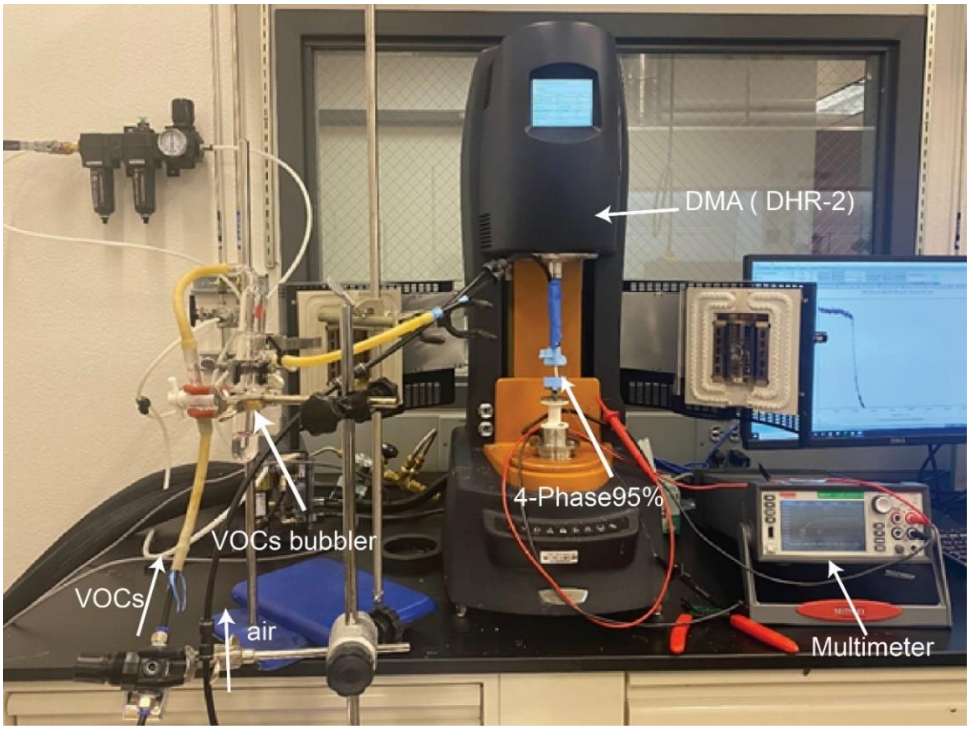

Figure 14. The in-house testing setup combines a dynamic mechanical analyzer (DMA) with the chemiresistor. Ethanol vapors are passed through the core of the 4-Phase95%CNTs sensor, which is constrained on the DMA axial tension fixer. DMA is used to control the strain and strain rate during uniaxial elongation.

Apart from the stability of the sensor under strain deformation, the ability to detect vibrational motion is also a critical factor in general inline measurement systems. To better demonstrate this interrelatedness between piezoresistive and chemiresistive properties and expand the sensor's application, DMA was further conducted, as shown in Figure 15. The 4-Phase95%CNTs sensor was attached to a DMA to simulate vibrations with a 0.1% strain deformation at a 2 Hz frequency. Continuous ethanol flow of 130 ppm started after 1 hour of vibration for a continuation of 8 hours. Figure 15 shows the synchronized storage

modulus ($G^{'}$) and the resistance behavior in response to ethanol vapor. G' shows a 36% decrease, from 0.85 MPa to 0.54 MPa, while $\Delta R/R_0$ increased 75% during the first hour. As the polymer is saturated with ethanol, both G' and $\Delta R/R_0$ stabilize at 0.55 MPa and 75% for 7 hours with no deuteriation. As the ethanol stops, $G^{'}$ was restored to 100% in 10 minutes as $\Delta R/R_0$ recovered to 28% after 200 minutes. The fast-reversible mechanical property of the sensor is primarily due to the fast desorption of ethanol in the outer TPU layer, which has a $G^{'}$ that is five times higher than the core and middle layer. Figure 15b shows the zoomed-in circled regions in Figure 15a, corresponding to the resistance response at stabilization, initial ethanol flow, saturated ethanol, and air response. While the fiber shows chemiresistive behavior in the larger time scale, the piezoresistance response with distinct jagged peaks successfully captures vibrational motion at a 0.1% strain rate with highly consistent patterns. However, the response due to 0.1% oscillation from sections 1 to 4 increased from 0.025% to 0.045%, indicating a less stable conductive nanoparticle matrix due to long-term ethanol exposure.

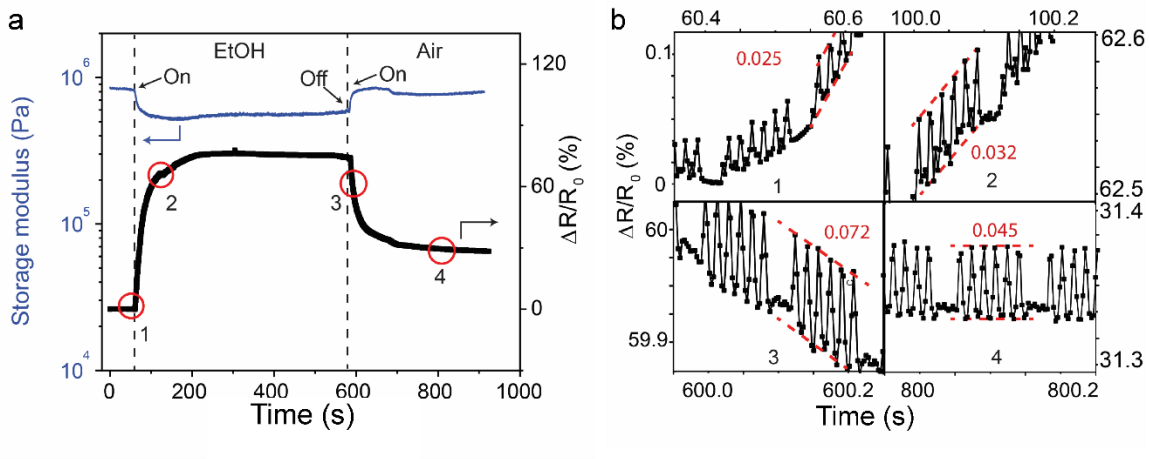

Figure 15. Long-term mechanical stability of the sensor. (a) The sensor's storage modulus and electrical response during and after constant 130 ppm ethanol flow for 8 hours. (b) The zoomed-in response of the corresponding sections demonstrates the detection of 0.1% strain during and after VOCs sensing.

Furthermore, the mechanical stability of the sheath layers plays an important role in gas transportation. To test the mechanical durability and sensitivity of the sensor in the presence of air pressure in a close system, PDMS was used to seal off one end of a 2 cm long 4-Phase95%CNTs fiber while the other end was tightly connected to a high precision pressure regulator with dry airflow (Figure 16). Figure 17a demonstrates the relative resistance changes with increasing air step pressures. The increase rate at each step was set at 6.89 kPa (1 psi) per second, following a 5-second hold before increasing to a higher step pressure. The lowest detectable range was 1 psi with an SNR of 14.2. The highest tolerable pressure was around 100 kPa, where a gradual decrease in resistance occurred at a constant pressure of 138 kPa. With increased air pressure, the middle MWCNTs/GnPs/TPU layer

experienced a radial expansion, disrupting the electron pathways and changing resistance. The fiber showed consistent cyclic performances for 6.89 kPa (1 psi), 13.79 kPa (2 psi), and 20.68 kPa (3 psi) in eight cycles, with 0.092%, 0.336%, and 0.532% degradation per cycle, respectively. Similar to the previous decreasing response shown in Figure 17b, the gradually decreasing response with cycle number and increasing pressure was likely the result of insufficient relaxation time, which was more obvious with 34.5 kPa (5 psi).

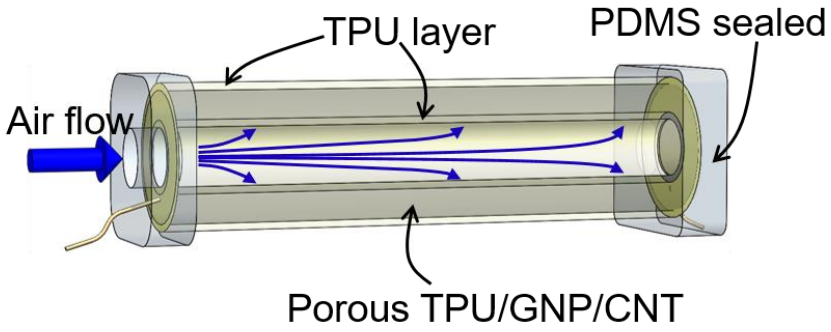

Figure 16. The experimental set-up for pressure sensing.

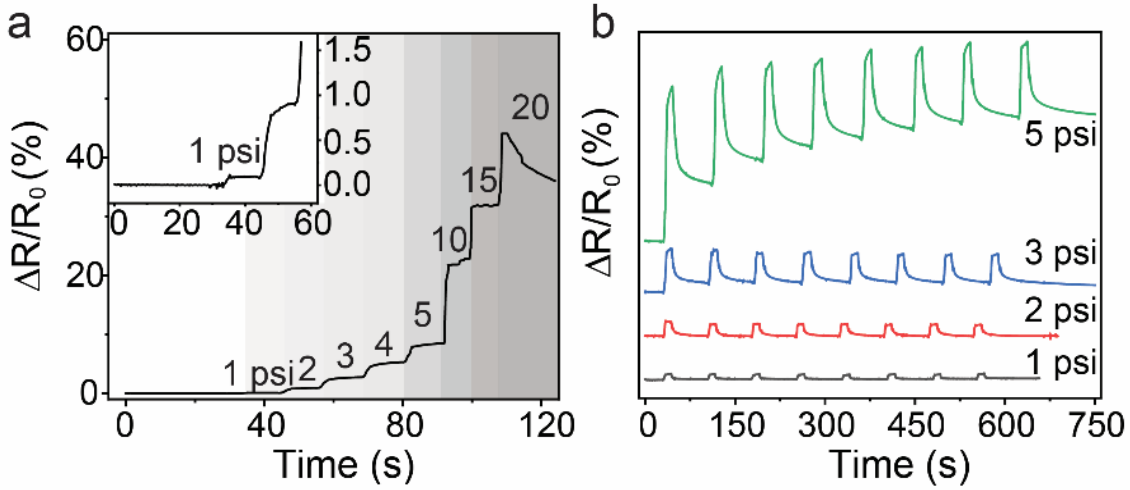

Figure 17. Piezoresistive effect under air pressure of the 4-Phase95%CNTs fiber with (a) stepwise increase of pressure and (b) cyclic performances.

2.8 Conclusion

An MWCNTs/GnPs/TPU multi-layered sensor was fabricated through an in-house designed spinneret and unique manipulations of material compositions. Through a solvent-exchange-driven polymer partition, a self-induced hollow-core and porous inner and middle layers were formed in a single step, which is scalable for manufacturing. As VOCs were transported through the inner core to the middle layer, the highly porous structure enhanced their diffusion into the sensing layer, resulting in a 600% signal-to-noise ratio increase compared to single-layered composite sensors. It should be noted that the sensitivity of the current micro-porous sensor is not yet comparable to most rigid and brittle solid-state sensors; however, further studies with nano-level porosity control and better management of nanocarbon configurations would significantly narrow this gap. Apart from VOC sensitivity and selectivity, the 4phase95% sensor also showed high stability before, during, and after uniaxial strain deformation. In addition, it was able to differentiate between deformation and VOCs due to changes in the baseline as responses. The hierarchical and multi-layered design in composite fiber microstructures significantly enhanced VOC sensing, complex strain conditions, and air pressure. This multifunctional fiber indicates potential applications, including detecting toxic gases at solvent production sites, examing chemical reactions, remotely monitoring human health and respiratory diagnostics, and discovering the characteristics of releases from soils in the oil-gas industry.

CHAPTER 3

IN-SITU ALIGNMENT OF GRAPHENE NANOPLATELETS VIA COAXIAL FIBER SPINNING

3.1 Introduction

As introduced in Chapter 2, a coaxial nozzle was designed to accommodate the single-step multimaterial fiber spinning process, resulting in different layers of material composites and morphologies, ultimately leading to a multifunctional VOC sensor. Chapter 3 aims to follow a similar process-structure-property approach, and at the same time, explores a 3-phase fiber structure for nanoparticle orientation control.

1D CNTs and 2D graphene are two of the most promising nanoparticle reinforcement fillers for superior mechanical and functional properties.[161] Numerous attempts have been made toward fabricating conductive polymer fibers via homogeneously mixing between the nanoparticles and the polymer matrices to achieve an interpenetrating network, also known as the percolation threshold.[162] Excellent dispersion quality and high nanoparticle aspect ratio are some of the most critical factors.[163] Nevertheless, a similar technique has rarely been reported for high-performance polymer composite fibers with semi-crystalline structures. Unlike bulk composites, these fibers require post-treatment, such as hot drawing, which requires a minimum amount of foreign particles.[164] Any addition of the nanoparticles could severally deteriorate the long-range order structure of the polymer chains.

Chapter 3 focuses on a unique 3-phase fiber where continuous conductive nanoparticles are sandwiched between the inner and outer polymer layers (Figure 18). Poly (vinyl alcohol) (PVA) was chosen as the polymer matrix for its excellent chemical resistance, biocompatibility, hydrophilicity, and processability.[165] GnPs are stacked graphene layers without exfoliation and were selected as the nanofillers for their relatively low cost. Unlike the traditional percolated network, the conductive GnPs are continuously connected, exfoliated, and aligned during the hot drawing process. This configuration enables the insulative PVA with an electrical conductivity up to 0.38 S m^{-1}, while maintaining high mechanical properties better than the dispersed GnPs/PVA and PVA fibers.

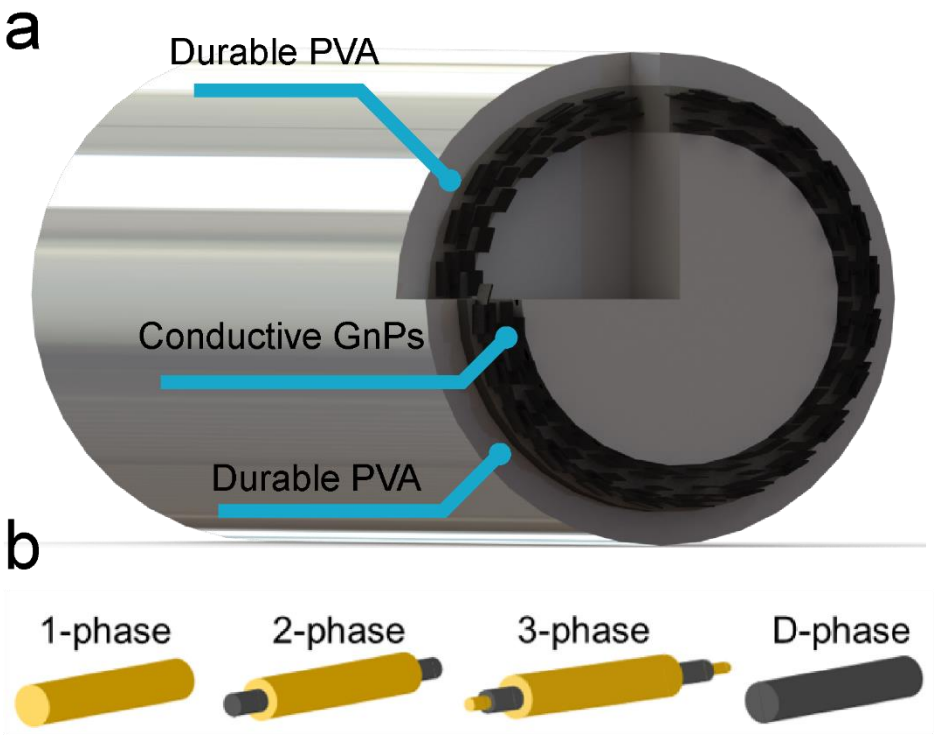

Figure 18. Schematic of the (a) 3-phase GnPs/PVA fiber and (b) 1-phase, 2-phase, 3-phase, and D-phase fiber structures.

3.2 Experimentation and Characterization

Materials: GNPs, grade C-750, were purchased from Sigma Aldrich with a specific area of 750 m_2 g^{-1}. PVA 28–98 was obtained from Kuraray with a molecular weight of ~145,000 g mol^{-1} and 98-99% degree of hydrolysis. Methanol (ACS reagent, 99.8%, 179337), dimethyl sulfoxide (DMSO, ACS reagent 99.9%, 472301), DMF, (ACS reagent, 99.8%, 319937), xylene (ACS reagent, 214736), and toluene (anhydrous, 99.8%, 244511) were purchased from Sigma-Aldrich (St. Louis, MO, USA) and used as received.

3-phase fiber spinning: 20 wt% of PVA polymer pellets were added to DMSO at 120 °C under mechanical stirring for 120 minutes until a clear solution was obtained. 20 wt% of GNPs was added to DMSO and was stirred and tip sonicated for 10 minutes at room temperature. A similar dry-jet wet spinning process to Chapter 2 was used with methanol as the coagulant. Syringes containing PVA, GNPs, and PVA were connected to the inner, middle, and outer inlets. An airgap of 1 cm and a take-up speed of 8 m min^{-1} were maintained. After 24 hours of soaking in methanol, the DMSO-free fiber was drawn between two winders at different speeds under stepwise temperatures of 100 °C, 150 °C, and 200 °C. A maximum draw ratio was recorded for each drawing stage.

2-phase fiber spinning: only the middle and outer channels of the spinneret were used. The inner channel was connected to the 20 wt% GNPs/DMSO dispersion, and the middle channel was connected to the 20 wt% PVA/DMSO solution. Spinning and drawing techniques were used as previously stated.

1-phase and D-phase fiber spinning: Only the outer channel of the spinneret was used. 20 wt% PVA/DMSO was used for 1-phase fiber. For D-phase fiber, 3.5 wt% of GNPs was

dispersed and stirred for 2 hours in 20 wt% PVA/DMSO solution, following 2 hours of mild sonication. Spinning and drawing techniques were used as previously stated.

Figure 18b shows the structures of each fiber type, and the draw ratios and fiber diameters after drawing at each temperature stage are shown in Table 3.

Characterization: Fiber morphology was studied using SEM on XL30 ESEM-FEG. Fibers were soaked in liquid nitrogen for 5 minutes before cutting the cross-sectional areas. In addition, 15 nm thick gold nanoparticle layers were deposited on the surface to improve conductivity. Thermogravimetric analysis (TGA, LABSYS EVO) was conducted for 1-, 2-, and 3-phase fibers. The chamber was purged with helium gas at 0.5 °C min-1 for 30 minutes, then heated at a rate of 10 °C min^{-1} up to 600 °C. Differential scanning calorimetry (DSC, TA instruments) was used to investigate the melting entropy of the fibers under a nitrogen atmosphere with a heating rate of 10 °C min^{-1}. A Wide-Angle X-ray diffractometer (XRD, Kristallo-Flex 710D X-ray generator, Bruker D5000, Siemens) was used with Cu Kα radiation (40 kV, 40 mA). The scanning range of the Bragg angle 2θ for XRD ranged from 5° to 70° under a scanning rate of 2° min^{-1}. Polarized Raman spectroscopy was used with a green laser (532 nm) in the VV configuration, in which a backscattering light intensity analyzer is set parallel to the polarized incident laser. The polarized laser beam was scanned from parallel to perpendicular with fiber axial direction. The tensile test was performed with Discovery HR-2 (TA instruments) at room temperature for 10 samples of each fiber type. The gauge distance was kept at 10 mm and the head-cross speed was set to 100 μm s-1. Electrical conductivity was measured using a multimeter at room temperature, with the test material length set to 2 cm for each fiber. For 3-phase

and 2-phase fibers, PVA polymer was scratched at the end to expose the GNPs channel. The silver paste was added to all fiber ends to increase the contact area with the multimeter probe.

Table 3. Fiber drawing conditions and diameters.

Draw ratio and diameter		3-phase	2-phase	1-phase	D-phase
		PVA-GnP-PVA	PVA-GnP core-shell	PVA	PVA/GnP mixtures
Draw ratio (DR)	DR_{-100}	8.47	7.74	7.55	6.87
	DR_{-150}	1.59	1.44	1.30	1.26
	DR_{-200}	1.21	1.33	1.30	1.16
	DR_{-total}	16.29	14.82	12.76	10.04
Diameter (μm)	D_{-100}	111.2	124.2	138.1	124.8
	D_{-150}	88.9	103.7	103.8	110.9
	D_{-200}	80.3	89.8	91.1	102.9

3.3 Multilayer Morphology and Nanoparticle Orientation Studies

The cross-sectional SEM image of the as-spun 1-phase fiber before the post-heat treatment shows a clean cross-section (Figure 19a), while the 2-phase and 3-phase fibers show distinction phases that indicate different layers of composites (Figures 19b-19c). GnPs in both fibers exhibit voids formed during the evaporation of DMSO and methanol. D-phase fiber shows inferior GnPs dispersion quality with aggregated GNP particles (Figure 19d). This could result from their relatively higher layer numbers and inconsistent morphologies.

After the hot drawing process, the 2-phase fiber shows uneven GnPs distributions and aggregates while the 3-phase fiber shows continuous GnPs. This can be observed based on the optical microscope images (Figure 19e). TGA analysis on the weight percentage of GnPs at various draw ratios confirmed the exfoliations of large GnPs aggregates for 3-phase fibers (Figure 19f). With increasing draw ratio, the weight residue of GnPs decreased from 6.5 wt% to 3.3 wt%. On the contrary, the weight residue of 2-phase fiber increased from 16.2 wt% to 19 wt%, indicating a lower tendency of the GnPs channel to exfoliate than the pure PVA polymer.

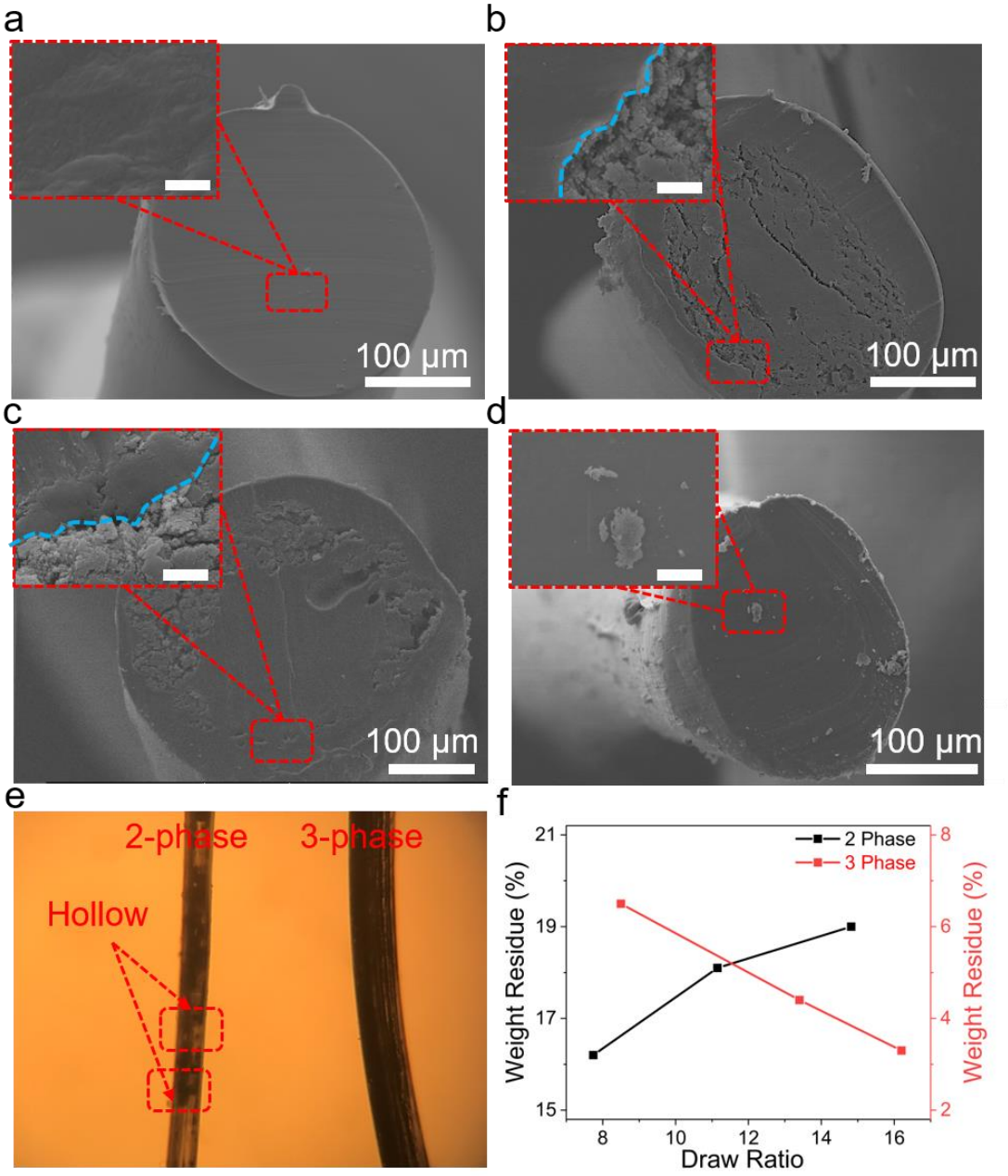

Figure 19. Cross-sectional SEM images of the as-spun (a) 1-phase, (b) 2-phase, (c) 3-phase, (d) D-phase fibers. (e) Optical microscope image of 2-phase and 3-phase fibers. (f) TGA weight residue with respect to drawing ratios.

After drawing, cross-sectional SEM images of the 3-phase fiber show densified GnPs channel (Figure 20a with the zoomed-in regimes in Figures 20b_{1-3}) with undisrupted PVA inner and outer channels. This distinct separation between the nanoparticles and polymers promotes better polymer crystallinity than 2-phase and d-phase fibers, where nanoparticles disrupt the polymer chain continuity. Figure 21a shows the calculated crystallinity, X_c, based on DSC measurements of the enthalpy of fusion (ΔH_f) at the melting point and Equation 3.1,

$$X_c = \frac{\Delta H_f(T_m)}{\Delta H_f^0(T_m^0)} \tag{3.1}$$

where ΔH_f^0 = 138.6 J g^{-1} is the enthalpy of fusion for a 100% crystalline sample.[166] For confirmation, XRD was also used to determine the crystallinities of 1-, 2-, and 3-phase fibers, and were calculated based on Equation 3.2 for their corresponding (1 0 1) planes located at ~19.7°, 19.8°, 19.8°, respectively (Figure 21b).

$$\text{Crystallinity} = \frac{A_{crystalline}}{A_{crystalline} + A_{amorphous}} \times 100 \tag{3.2}$$

Crystallinity is a critical factor in determining the uniaxial mechanical properties of polymeric fibers. Crystallinity degree values of the PVA matrix were measured to be 68% and 66% for 1-phase and 3-phase fibers, respectively, based on XRD. Similarly, crystallinity degrees of the PVA matrix were calculated as 64.1% and 63.6%, respectively. On the contrary, 2-phase and D-phase fibers show significantly lower crystallinity degrees which are likely due to the aggregated GnP defects as they promote fiber fractures during the drawing process, inhibiting the polymer chains from being drawn to the maximum (Table 3).

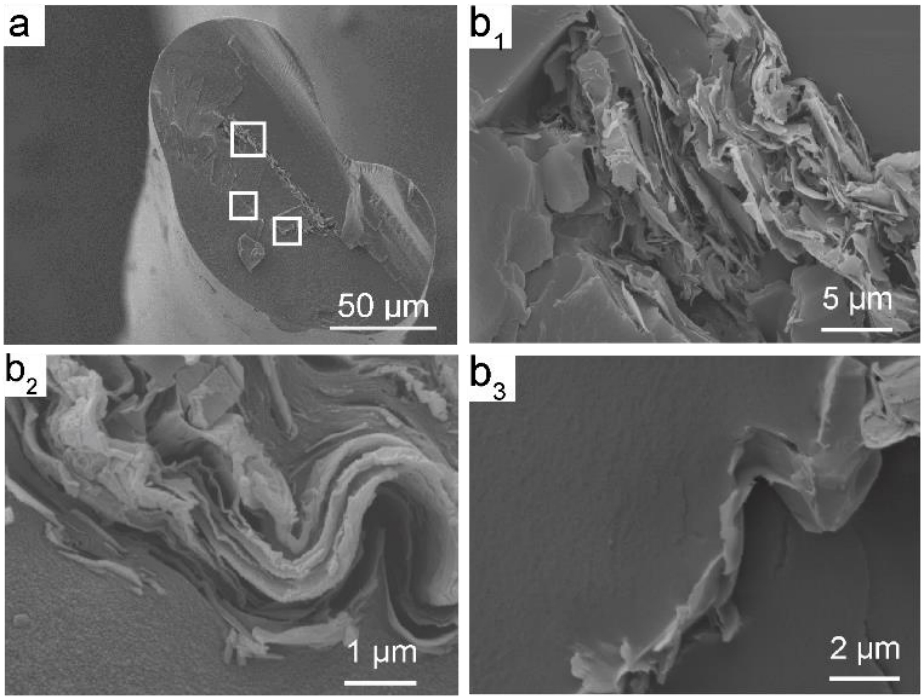

Figure 20. Cross-sectional SEM images of the (a) 3-phase fiber after drawing with corresponding (b_{1-3}) showing zoomed-in sections.

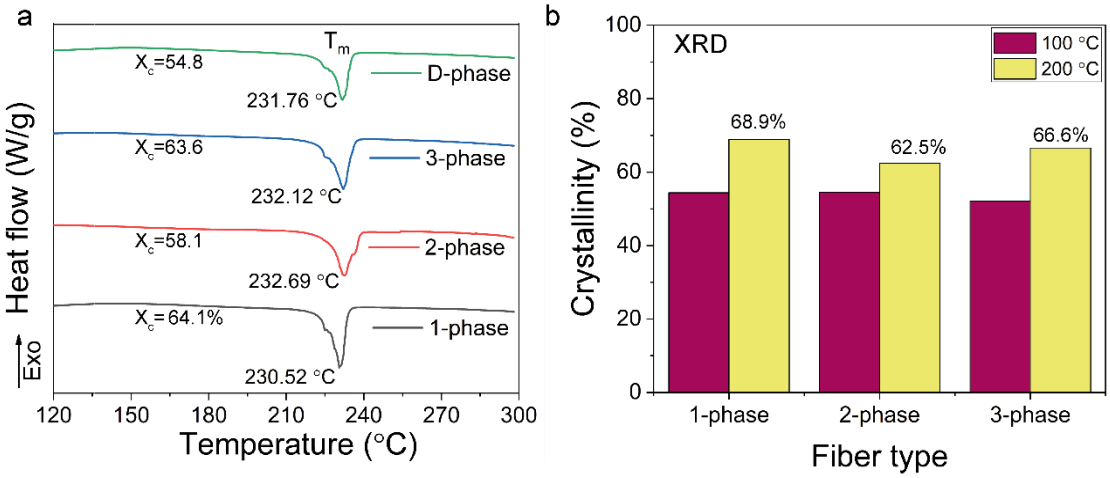

Figure 21. Crystallinity based on (a) DSC measurements of enthalpy of fusion and (b) XRD fitted area.

From Figures 20b$_{1-3}$, the 2D GnPs are highly aligned in the axial direction. Nanoparticle alignment is crucial for high load transfer efficiency, lower interfacial resistance, and faster in-plane electron transfer for GnPs.[73,113,167] Raman spectroscopy was used to quantify the spatial orientation of GNPs. Previous studies suggest that the 2D band intensity (I_{2D}) of graphene-based materials shows strong angular dependency as a function of the incident light angle.[95] A 3-phase fiber sample was set up with a polarized laser focusing on the middle and side sections of the GNPs channel, as shown in Figures 22a$_{1}$-a$_{2}$. By rotating the angle, ϕ, between the fiber axis and the polarized Raman laser from 0° to 90°, 2D band intensities, I_{2D}, at~ 2750 cm^{-1} were collected and normalized (Figures 22b and c). No angular dependency is observed for laser-focused on the middle fiber section, indicating that the laser is perpendicular to the 2D GnP plane. On the other hand, the I_{2D} indicates a decrease in intensity as ϕ increased from 0° to 90° when focused on the side section. The normalized intensity was fitted into an orientation distribution function (ODF),[168] as shown in Figure 22c and Equation 3.3:

$$I_{GNPs}(\phi) = I_0 \left\{ \frac{8}{15} + \langle P_2(\cos\theta) \rangle \left(-\frac{16}{21} + \frac{8}{7}\cos^2\theta \right) + \langle P_4(\cos\theta) \rangle \left(\frac{8}{35} - \frac{8}{7}\cos^2\phi + \cos^4\phi \right) \right\} \quad (3.3)$$

where ϕ is the angle between the fiber axis and the incident laser. $\langle P_2(\cos\theta) \rangle$ and $<P_4(\cos\theta)>$ are the second- and fourth-ordered Legendre polynomials with fitted values of 0.55 and 0.67. Usually, $<P_2(\cos\theta)>$ is the primary orientation parameter, while the $<P_4(\cos\theta)>$ term reconstructs the complete ODF.[168] Since the GnP has a plate/spherical shape, the ODF expression assumes the nanoparticles are uniaxial symmetric, explaining the

mismatches between the data and the fitted curve.[169] The Krenchel factor η_0 measures the orientation of the nanoparticles, with η_0=1 indicating perfect alignment and 1/5 indicating random 3D orientation. By integrating the ODF over all space, η_0 is shown as:

$$\eta_0 = \frac{8}{15} + \frac{8}{21}\langle P_2(cos\theta)\rangle + \frac{3}{35}\langle P_4(cos\theta)\rangle \tag{3.4}$$

By substituting the second- and fourth- Legendre polynomial, η_0 is determined to be 0.8.

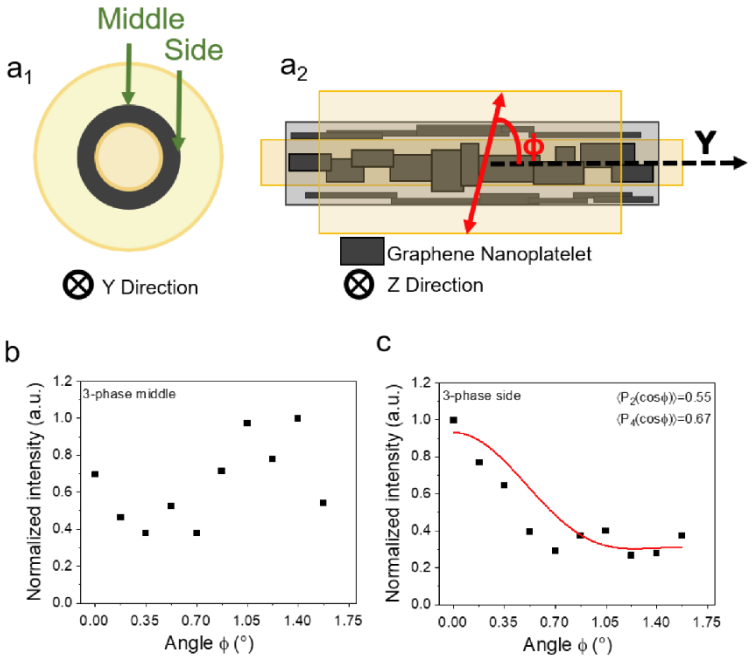

Figure 22. Raman spectroscopy data and illustration of the alignment process. (a_1) Cross-sectional view (along the fiber axis, y-axis) of the 3-phase fiber showing middle and side sections for Raman spectroscopy tests. (a_2) Top view (perpendicular to the y-axis). Normalized 2D band intensity for (b) middle and (c) side sections.

A microstructure model shown in Figure 23 is proposed to show the mechanism for the GnPs alignment. Before the drawing, PVA chains at the interfaces between the

inner/middle/outer layers are in a low crystalline state, surrounded by misaligned GnPs. During the drawing process, the temperature gradient across the fiber radial direction would result in shear stress generated by the mismatched mechanical properties of the inner and outer PVA channels. The outer polymer chains closer to the heat zone would be stretched when stress is applied at temperatures above the glass transition point (i.e., 85 ^{o}C for PVA). The transfer of this shear stress and extension trends from exterior polymers to the middle GnP channel caused the step-wise exfoliations of stacked GnPs and oriented them in the axial direction. On the other hand, the shear stress generated in the 2-phase and D-phase fibers is insufficient to either constrain the GNPs channel or rotate individual GnP.

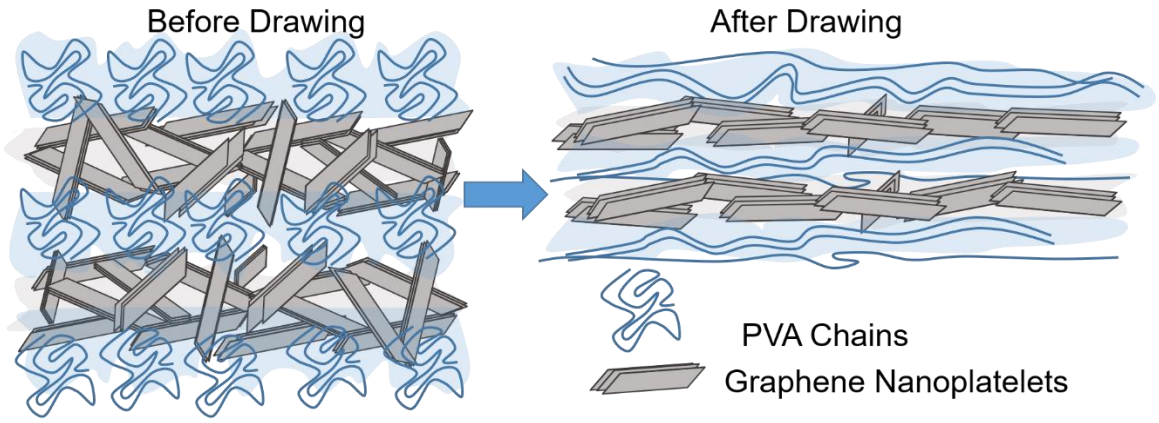

Figure 23. Schematic of the GnP alignment process.

3.4 Mechanical and Electrical Properties

The stress-strain curves of the 1-phase, 2-phase, 3-phase, and D-phase fibers after heat-drawing are shown in Figure 24a. The 1- and 3-phase fibers show lower strain compared to 2- and D-phase fibers. This is likely the result of higher crystallinity, representing more elongated polymer chains during the fiber drawing process. For 3-phase fibers, the average

Young's modulus and tensile strength are 38.8 GPa and 962.9 MPa, respectively, 73.5% and 17.3% higher than the 1-phase fiber values (i.e., 22.4 GPa modulus and 821.0 MPa strength). On the other hand, 2-phase fibers show inferior modulus and strength of 17.5 GPa and 518.1 MPa. Higher standard deviations in their strength generally indicate a correlation between the mechanical performance and the probability of defects presented within the gauge length. SEM images suggest that fractures mainly occurred around the voids of the 2-phase fibers, as previously discussed, whereas 1-phase and 3-phase fibers show brittle fracture cross-sections (Figures 25a-25c). The Young's modulus and strength for the D-phase fiber are 16.7 GPa and 603.2 MPa, respectively. During the hot drawing process, large GnP aggregates would promote fractures and constrain and reduce the mobility of the polymer chains, resulting in a much lower draw ratio and limited crystallinity. Consequently, one of the research goals of homogeneously mixed graphene-based conductive fiber is to achieve the percolation threshold with minimum nanoparticle loading, which rarely exceeds ~2 wt%, according to literature reports.[170]

After hot drawing for the homogeneously mixing method, conductive nanoparticles usually lose their interconnected network structure.[171] In contrast, the proposed sandwiched GnPs channel promotes superior electrical conductivity with increased draw ratios. Resistance was measured for all fiber types, and conductivity was calculated based on Equation 3.5,

$$\sigma = \frac{L}{R\pi r^2} \tag{3.5}$$

where σ, R, r, and L are electrical conductivity, resistance, fiber radius, and fiber length, respectively. Figure 24b shows that both Young's modulus and electrical conductivity

increase with an increased draw ratio for the 3-phase fiber, and the conductivity ultimately reaches 0.38 S m^{-1} while maintaining a modulus of 38.8 GPa. This indicates that the alignment of GNPs also enhances the interactions between each platelet, creating more efficient pathways for electrons. On the other hand, 1-phase, 2-phase, and D-phase fibers showed electrical insulation behaviors due to the insulating nature of PVA polymer and discrete nanofiller network.

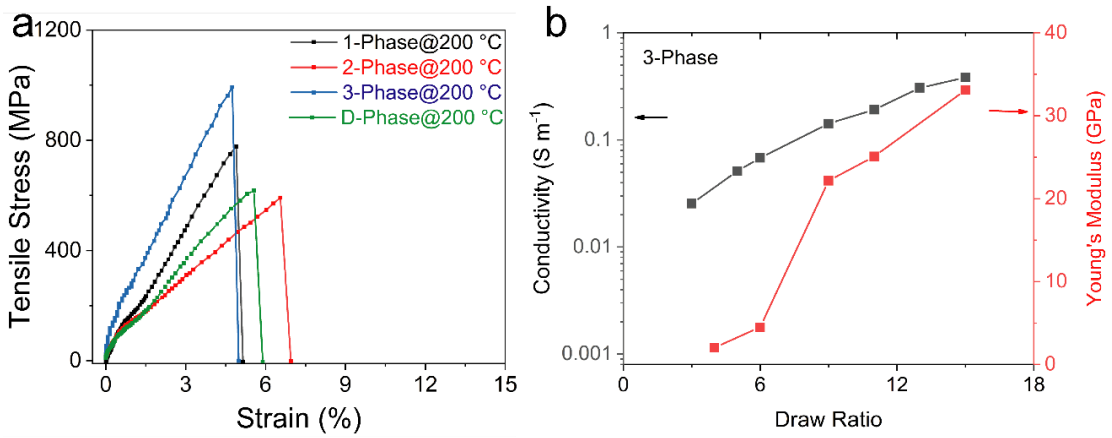

Figure 24. Mechanical and electrical properties. (a) stress-strain curves fiber different fibers. (b) Relationship between modulus and electrical conductivity of 3-phase fiber.

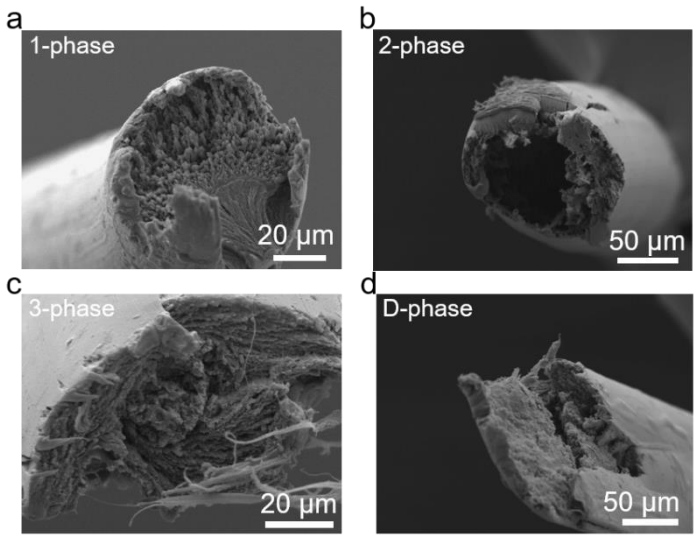

Figure 25. Fracture surface morphology of (a) 1-phase, (b) 2-phase, (c) 3-phase, and (d) D-phase fibers.

3.5 Conclusion

In Chapter 3, the multilayered spinneret not only shows applications in multiphase material fiber spinning, but also demonstrates that the inclusion of interfaces would promote better anisotropic nanoparticle orientation. The resulting 3-phase fiber shows 73.5% and 17.3% enhancements in Young's modulus and tensile strength, respectively, compared to pure PVA fiber. At the same time, the fiber possesses an electrical conductivity of 0.38 S m^{-1}. We believe such microstructure can be further applied to align 2D materials beyond graphene, including boron nitride (BN), molybdenum disulfide (MoS_2), and MXene layers rise to functional properties such as electrical and thermal conductivities.

CHAPTER 4

MICROSCALE PATTERNING OF NANOPARTICLES FOR ANISOTROPIC PROPERTIES

4.1 Introduction

As introduced in Chapter 3, coaxially structured composite fibers have shown advantages in achieving highly conductive GnPs channels. Nevertheless, fiber with a 0.38 S m^{-1} conductivity has limited real-world applications, aside from static-dissipative parts or piezoresistive sensors. One of the major causes is the low volume percentage of the conductive channel compared to the overall fiber. As shown in Figure 20, the GnPs channel with a 2 to 10 μm layer thickness is the only electron transport channel, whereas the rest of the fiber consists of insulative PVA. Increasing the number of the continuous GnPs channel is a reasonable strategy. However, precise manipulation of the GnP conformation and morphology is significantly limited by the tooling resolution and material compatibilization to fine-resolution tools. Increasing the GnPs channel numbers would inevitably increase spinneret diameter, and fiber diameter would inevitably increase simultaneously. In Chapter 4, a different multilayered nozzle design is introduced to selectively arrange and continuously assemble patterned nanoparticles within the composite fiber.

As previously mentioned, homogeneous mixing between the nanoparticles and polymer matrices for synergistic and hybrid properties has been the most adopted strategy for fabricating composites with isotropic properties.[172] On the other hand, processes such as

ice-templating,[173,174] layer-by-layer casting,[175,176] additive manufacturing,[177–180] field-assisted nanoparticle patterning,[71,181] and particle self-assembly,[89,182] have been developed to achieve a higher degree of freedom in particle morphology and conformation control. These procedures usually generate organized microstructures or hierarchies of nanoparticles tailored to specific applications rather than a homogeneous mixture between the fillers and the polymer matrices. For example, directional ice-templating can generate a myriad of microstructures and microarchitectures where particle fillers are arranged in lamella, radially aligned, or honeycomb structures, just to name a few. These composites are usually applied to areas requiring structural or property anisotropy, such as unidirectional ionic conductivity in the composite electrolyte or cell alignment in tissue scaffolds.[85,183]

Here, a combination of the forced assembly process and the dry-jet-wet fiber spinning is investigated towards generating multilayered composite fiber where nanoparticle pattern resolution is not limited by tooling engineering (Figure 26a). Through flow behavior-driven layer multiplication process, microscale feature size could be achieved while the spinneret dimension is maintained at the centimeter scale. Kenics static mixer is a commercialized technique for in-situ mixing of two or more liquids or gases with applications varying from tissue engineering, cell growth, heat transfer, and chemical synthesis.[64,184,185] Instead of forming a uniform mixture of multiple components, the modified layer multiplication technique aims to form controllable nano to microscale features between two feedstocks. The working principle is shown according to Figure 26b. As two precursor solutions enter one multiplier, they are split horizontally and are

rearranged vertically, transforming two adjacent layers into four alternating layers. Figure 27 shows the 3D printed spinneret (Figure 27a) and the multipliers with and without polymer flow (Figure 27b). By connecting an additional multiplier, the layers are again multiplied, resulting in eight total layers (Figures 27$c_{1\text{-}3}$). Equation 4.1 describes the relationship between layer number, L, and the number of multipliers, n:

$$L=2^{n+1} \tag{4.1}$$

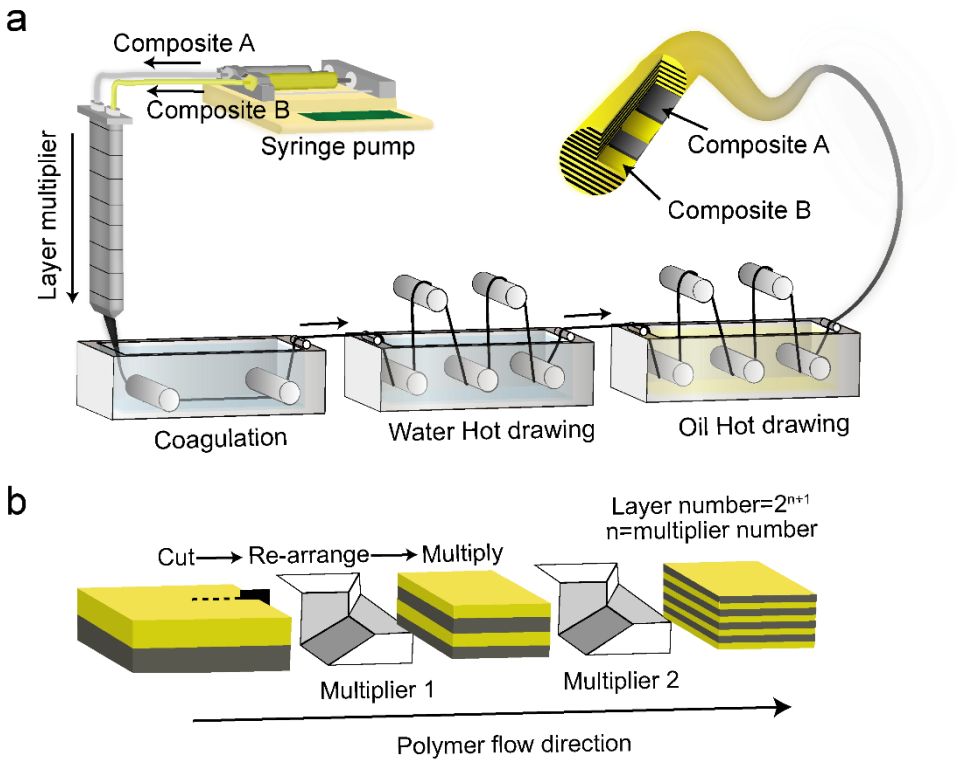

Figure 26. The experimental design and setup. (a) The combination of dry-jet-wet spinning and force assembly process for the fabrication of multilayered fiber. (b) The working mechanism for the force assembly process.

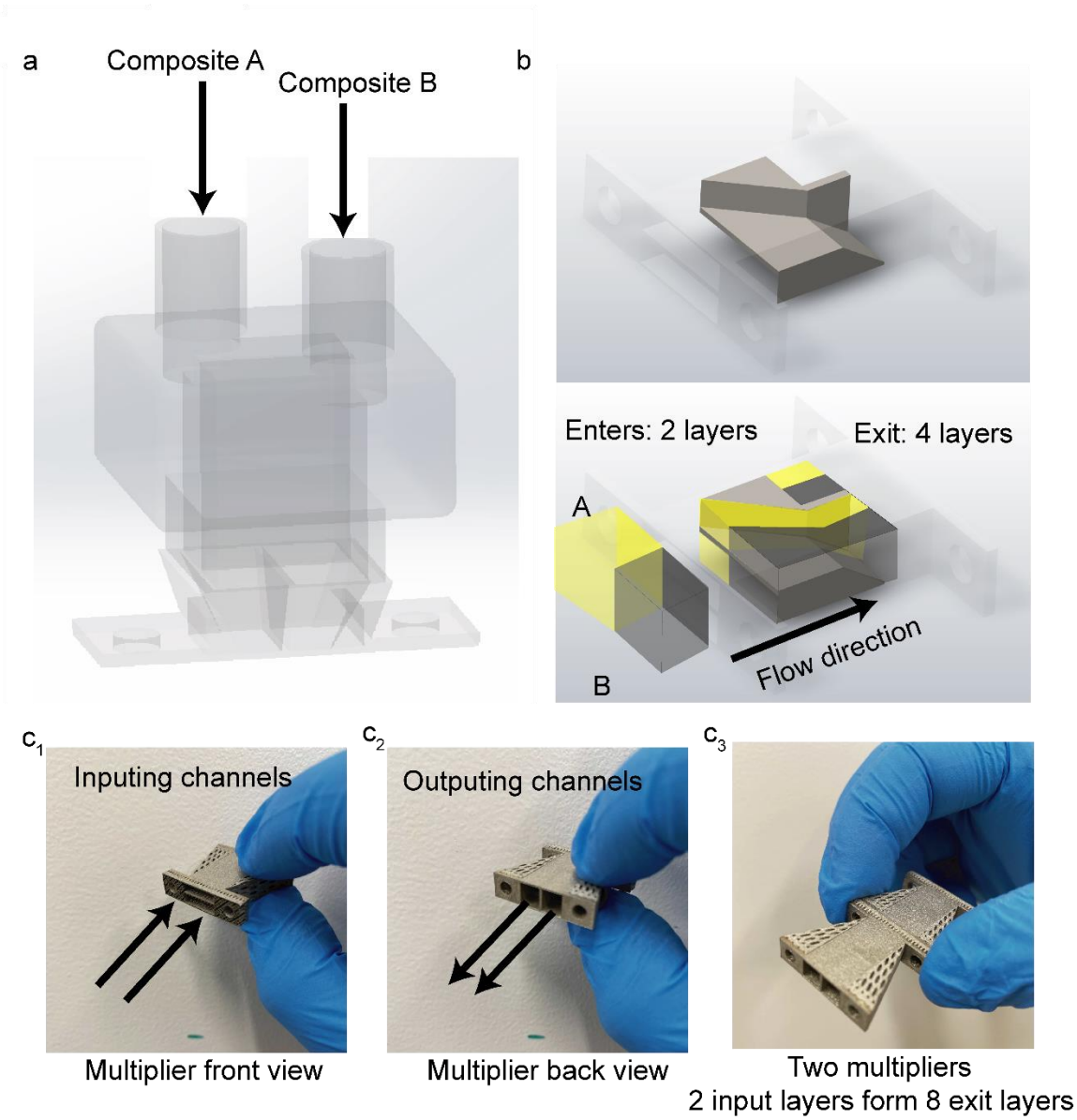

Figure 27. Design of the multilayered spinneret. (a) Spinneret head where composites A and B are first injected. (b) CAD design of the multiplier with and without polymer flow indication. The 3D-printed multiplier with (c_1) front view, (c_2) back view, and (c_3) two multipliers connected.

To explore the process-structure-application relationship based on this technique, alternating layers of thermally conductive BN nanoparticles and PVA polymer is fabricated for passive thermoregulating textiles.[186] Many theoretical models have suggested that thermal conductivity is heavily dependent on the microstructure of nanoparticles and polymer matrices.[187–189] For example, Figure 28a shows the thermal conductivity differences among Maxwell-Eucken, Series, and Parallel models, where k_1, k_2, and k_c represent the thermal conductivity parameters for polymer, nanoparticle, and composite materials, respectively. For thermal insulating composite, $k_1/k_2 > 1$, the Series model shows a much lower k_c, whereas, for thermal conductive composite, $k_1/k_2 < 1$, the Parallel model shows a much higher k_c.[190,191] Previous studies on passive thermoregulation composite fibers primarily reflect the Maxwell-Eucken model since complex microstructure control in textile fibers remains a challenge due to the microscale fiber dimension and production continuation requirements.[45,86,192,193] Through our unique flow behavior-driven layer-multiplying process, the layer domain size was controlled on the micrometer scale (depending on nanoparticle dimensions and geometry). This research demonstrates the potential of fabricating anisotropic fibers with highly hierarchical laminating structures. Nanoscale boron nitride (BN) (Figure 28b), based on covalently bonded boron and nitride layers known for their high thermal conductivity,[72] is selected as the first example to examine layer manufacturability and heat dissipation capabilities. As a result of the nanoparticle assembly and alignment, conductive pathways are formed along continuous BN channels within polymeric fibers that were flexibly woven as textiles for passive thermoregulation control on the macroscale (Figure 28b). Furthermore, the obtained

nanoparticle patterns display an ordered lamella structure consistent with the Parallel model, with mechanical and thermal properties investigated experimentally and validated computationally. The demonstrations of two other polymer/particle combinations also suggest broad applications of our facile and effective fiber spinning strategy in porous media and high-performance composite/hybrid systems.

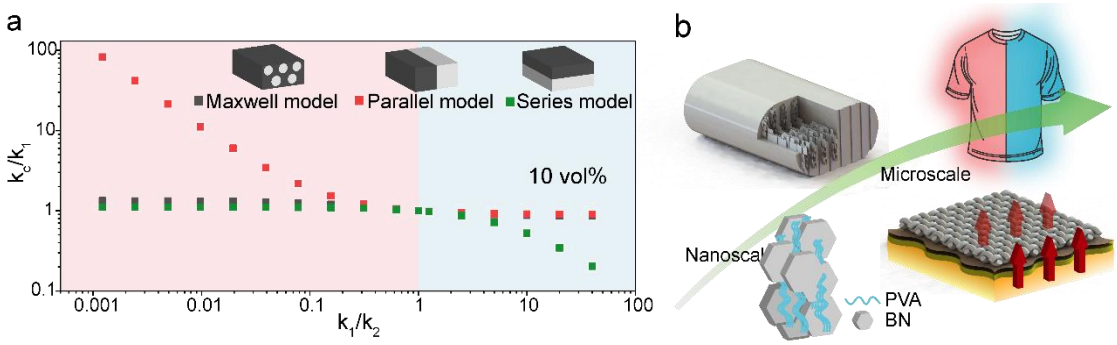

Figure 28. (a) Comparisons among the Maxwell-Eucken, Parallel, and Series models (insert illustrations).[187] (b) Schematic illustrations of the hierarchically structured composites, from nanoscale layers to microscale fibers to macroscale fabrics.

4.2 Experimentation and Characterization

Materials: PVA (28-98) pellets were obtained from Kuraray, Japan, with a molecular weight of ~145,000 g mol^{-1} and 98-99% degree of hydrolysis. Polyacrylonitrile (PAN) powder (230,000 g mol^{-1} and mean particle size 50 µm with the copolymer content of 99.5% acrylonitrile (AN)/0.5% methyl acrylate (MA)) was purchased from Goodfellow Corporation, US. Hexagonal BN nanoparticles (99.5%) were purchased from Skyspring Nanomaterials Inc., US. Aluminum particles (99%, 15 µm particle size), GnPs (xGnP M-5, 5 µm particle size, 120 $m^2 g^{-1}$ surface area), DMSO (ACS reagent 99.9%), DMF (ACS

reagents, 99.8%), methanol (ACS reagent, 99.8%), and hydrochloric acid (HCl) (ACS reagents, 37%) were purchased from Sigma Aldrich, US.

Layered composites from BN/PVA fiber spinning: The multilayered spinneret was 3D printed using Concept Laser M2 Cusing (GE Additive, US) with metallic powders of Inconel 718. For PVA spinning dope, desired weight concentrations of PVA powder (e.g., *x* wt%) was fully dissolved in DMSO at 100 °C. For BN/PVA spinning dope, 10 wt% of the desired PVA powder was first dissolved in DMSO, then mixed with desired BN nanoparticles for 30 minutes. The mixture was then sonicated in a sonication bath for 1 hour. Next, the remaining PVA powder was added to this solution and mechanically stirred for three hours at 100 °C. Next, pure PVA and BN/PVA spinning dopes were deaerated under vacuum for 1 hour at 80 °C. Subsequently, the bubble-free spinning dopes were transferred into two separate stainless-steel syringes and extruded at 1.5 ml min^{-1} through the customized spinneret into a methanol coagulation bath at room temperature with an air gap distance of 1 cm. After 24 hours, the fibers were drawn at room temperature, followed by drying for 12 hours in a vacuum at 50 °C. Finally, these dried fibers were drawn at 100 °C and 180 °C, respectively.

Porous PAN fibers from Al/PAN fiber spinning: For the pure PAN layer, 15 wt% of PAN was added to DMF and was mechanically stirred at 80 °C for three hours. For the hollow layers, 20 vol% of Al powder was added to 12 wt% PAN/DMF solutions, followed by three hours of mechanical stirring at 80 °C. Then, these spinning dopes were deaerated under vacuum at 80 °C for one hour before being injected via the in-house developed spinneret (same conditions as the BN/PVA fiber spinning). The collected fibers were drawn

immediately in water at 80 °C before forming gelled fibers in methanol and dried in a vacuum oven at 50 °C. At last, the dried fibers were placed into a 5 M HCl solution for 36 hours for Al etching.

Layered multi-material hybrids from BN/GnPs fiber spinning: The desired wt% of GnPs and BNs were separately mixed with 1g of PVA in DMSO, followed by 1 hour of bath sonication. The remaining PVA powder was added and was mechanically stirred for 3 hours at 100 °C. After the same spinning conditions, the collected fiber was kept immersed in a methanol bath for 24 hours, then dried at room temperature.

Characterizations: Rheological behaviors and uniaxial tensile tests were conducted using Discovery HR-2 (TA Instruments). For viscosity tests, a 40 mm, 2° Peltier plate was used with a truncation gap of 100 μm. For tensile tests, ten samples of each fiber type were tested with a gauge length of 2 cm and a gauge speed of 150 μm s^{-1}. SEM images were taken using Auriga FIB-SEM, Zeiss, Germany. To increase the conductivity, all samples were coated with 15 nm thick Au/Pd. 800 nm thick samples of the BN/GnPs fiber were obtained from a microtome (Leica RM2235, Germany) for SEM analysis. TGA was conducted in air at a heating rate of 10 °C min^{-1} (TGA 550, TA Instruments). DSC was conducted (DSC 250, TA Instruments) in N_2 with a scan rate of 10 °C min^{-1}. X-ray tomography was conducted using Xradia Versa 620 (ZEISS) with the dual-energy scanning method to enhance the contrast between layers having similar densities. An accelerating voltage of 40 kV and 150 kV were used. Voxel resolutions of 4.6 μm and 6.3 μm were obtained for the 8L10% and 16L10% fibers, respectively. Segmentation and rendering were done using the Dual Scan Contrast Visualizer (DSCoVer) (ZEISS) and Avizo 9.0

(FEI, Thermo Fisher Scientific), respectively. Thermal images were taken via infrared camera E8-XT (Flir) with 320×240 pixel resolution.

4.3 Rheological Behavior Study

The rheological properties play a vital role in forming controllable layer morphologies during fiber spinning. For example, different PVA and BN combinations were studied for optimized rheology (Figure 29). Based on SEM analysis, the BN nanoparticle used in this work has an average lateral dimension of 340 nm ± 140 nm. The measured viscosities at a shear rate of 1 s^{-1} and the damping parameter (tan(δ)) values are shown in Figures 30a and 30b, with indicated green regions corresponding to the spinnability window because of the fiber gelation capability and solidification kinetics. Firstly, uniform layers need to be formed via a low Reynolds number (*Re*) where the inertia is negligible compared to viscous and pressure forces (e.g., *Re* = 0.05).[184] By fixing the characteristic linear dimension (*L*, m) and fluid density (ρ, kg m^{-3}), a minimally required liquid viscosity (η, Pa·s) of 5 Pa·s was calculated based on Equation 4.2,

$$Re = \rho v L \, \eta^{-1} \tag{4.2}$$

where *v* is the flow speed (m s^{-1}). Due to syringe pump power, the upper viscosity limit was set to 100 Pa·s. Secondly, the polymer chains must form strong enough entanglement within each constrained and size constantly changing channels during layer multiplying to avoid interlayer diffusions. As a simple demonstration, Figure 30c shows the fiber pulling effects of 20 wt% PVA and 5 wt% PVA/50 vol% BN solutions, both with a zero-shear viscosity higher than 10 Pa·s followed by a viscosity plateau, favoring fiber gelation and layer retention in separate channels during fiber spinning.[194] PVA's high viscosity also

prevented the transport of the adjacent BN nanoparticles across the layer interfaces, with a stable solution/suspension interface.

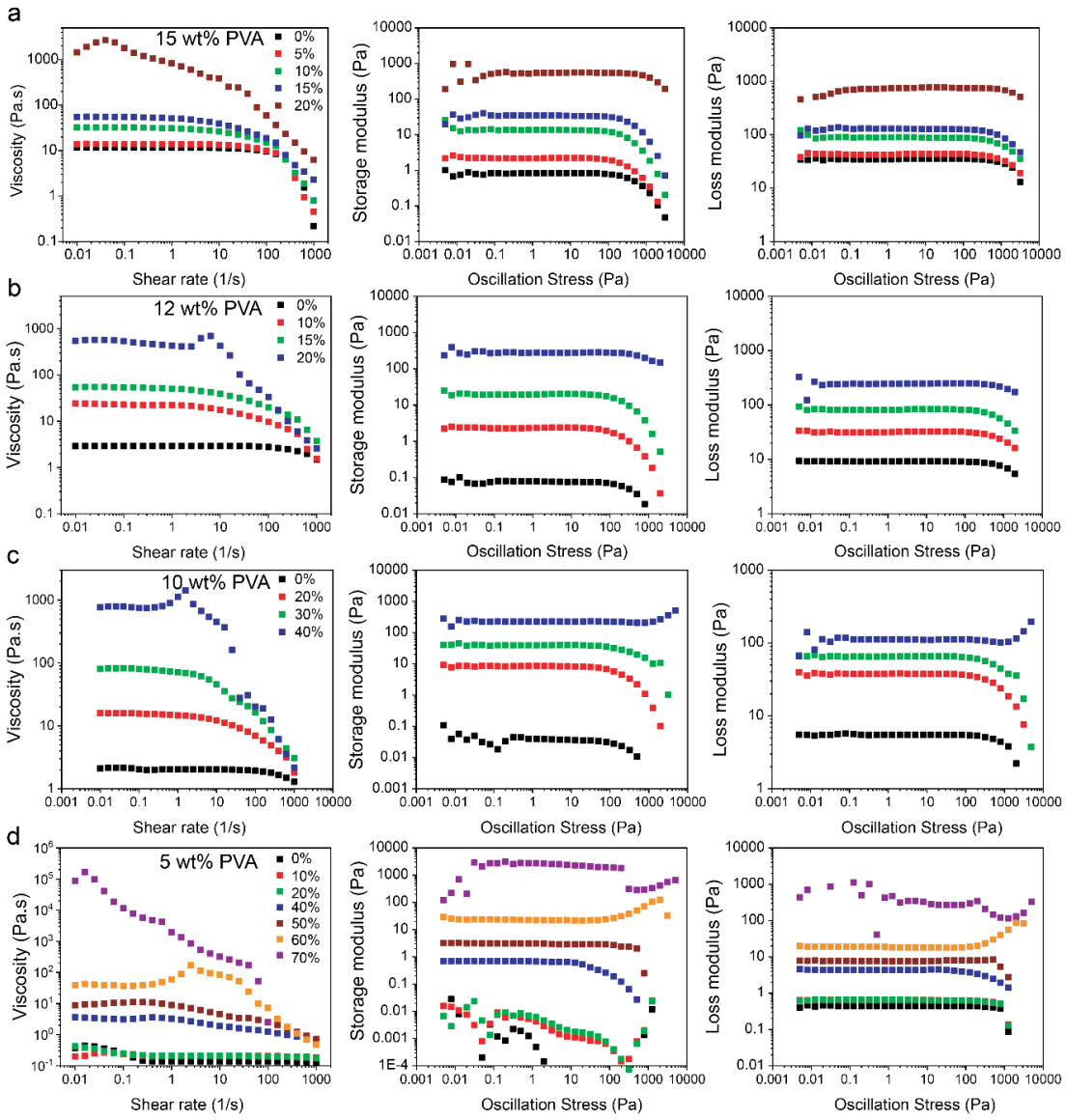

Figure 29. The flow behaviors (i.e., viscosity, storage modulus, loss modulus) of different BN volume concentrations with (a) 15 wt%, (b) 12 wt%, (c) 10 wt% (d) 5 wt% PVA/DMSO.

Thirdly, as a feature of viscoelasticity, shear-thinning behavior is essential to colloidal dope spinnability.[195] As rigid BN nanoparticles can be assumed to be perfectly elastic,[196] their increased concentration in viscous PVA solutions would penetrate between the polymer chains and lower their networking/entanglement, reducing their flowability, especially within a shear field that may cause nanoparticle alignment.[197] At a certain point, the excessive BN would change the solution's flow behavior from pseudoplastic to dilatant (i.e., shear-thickening) (Figure 29), unfavorable for shearing-involved extrusion and injections.[197] As a result, the gelation point where tan*(δ)* equals one was used as one of the criteria for the least-satisfying flow behavior (Figure 30b). By varying the polymer or nanoparticle concentrations of each spinning dope system, a phase diagram of the PVA/BN system is shown in Figure 30d, with the green dots illustrating the spinnable window; the highest achievable BN concentration was determined at 50 vol% within the 5 wt% PVA/DMSO solutions.

Last but not least, the viscosity matching between alternating layers is critical to achieving intact and distinct layering (Figure 31a). As a comparison, optical images suggest a high viscosity-mismatch of 40 pa·s would result in non-uniform layer thicknesses and layering disruptions (Figure 31b) under the same spinning parameters (e.g., injection/collection rates, coagulation environment). The computational fluidic dynamic (CFD) simulation was used to visualize the layer multiplying efficiency with different viscosity combinations (Figures 31c-31e). The gradual increase in the layer thickness mismatch with respect to layer viscosity differences indicates that layer disruption is a gradual process that deteriorates with increased viscosity mismatch (Figures 31f-h). Figure 32 shows the CFD

simulation of a 16L10% fiber where the top figure shows a view perpendicular to the major axis and the bottom figure shows a view perpendicular to the minor axis, respectively. Uniform layers were successfully formed by matching the viscosity between 18 wt% PVA and 20 vol% BN in 10 wt% PVA (i.e., 60 Pa·s and 58 Pa·s, respectively, at a shear rate of 1 s^{-1}, as shown in Figure 29a). Via four multipliers, two adjacent PVA and BN/PVA layers were multiplied into 16 layers across the major axis, and the composition remained the same across the minor axis. Table 4 summarizes the compositions and terminology of various fiber types, with the rest of the samples studied in the following sections. Layer A and layer B have the same composition for fibers with uniform structure. For example, U10% represents uniform structured fibers with 10% BN. However, for fibers with a multilayer structure, layer A is pure PVA and layer B is BN/PVA, with x representing the number of layers. For example, 4L20% represents 4 alternating layers within fibers with 20 vol% BN (Table 4). All wt% values are weight percentages of polymers with respect to the solvent, and vol% values are volume percentages of solid BN powders with respect to the polymer content.

Table 4. Summary of the spinning dope compositions and fiber terminology

Structure	Overall BN concentrations (vol%)	Layer A composition	Layer B composition	Terminology
Uniform	0	20 wt% PVA		U0%
	5	5 vol% BN, 18 wt% PVA		U5%
	10	10 vol% BN, 15 wt% PVA		U10%
	20	20 vol% BN, 10 wt% PVA		U20%
	30	30 vol% BN, 10 wt% PVA		U30%
	40	40 vol% BN, 8 wt% PVA		U40%
Multilayer	5	20 wt% PVA	10 vol% BN, 15 wt% PVA	xL5%
	10	18 wt% PVA	20 vol% BN, 10 wt% PVA	xL10%
	20	15 wt% PVA	40 vol% BN, 8 wt% PVA	xL20%

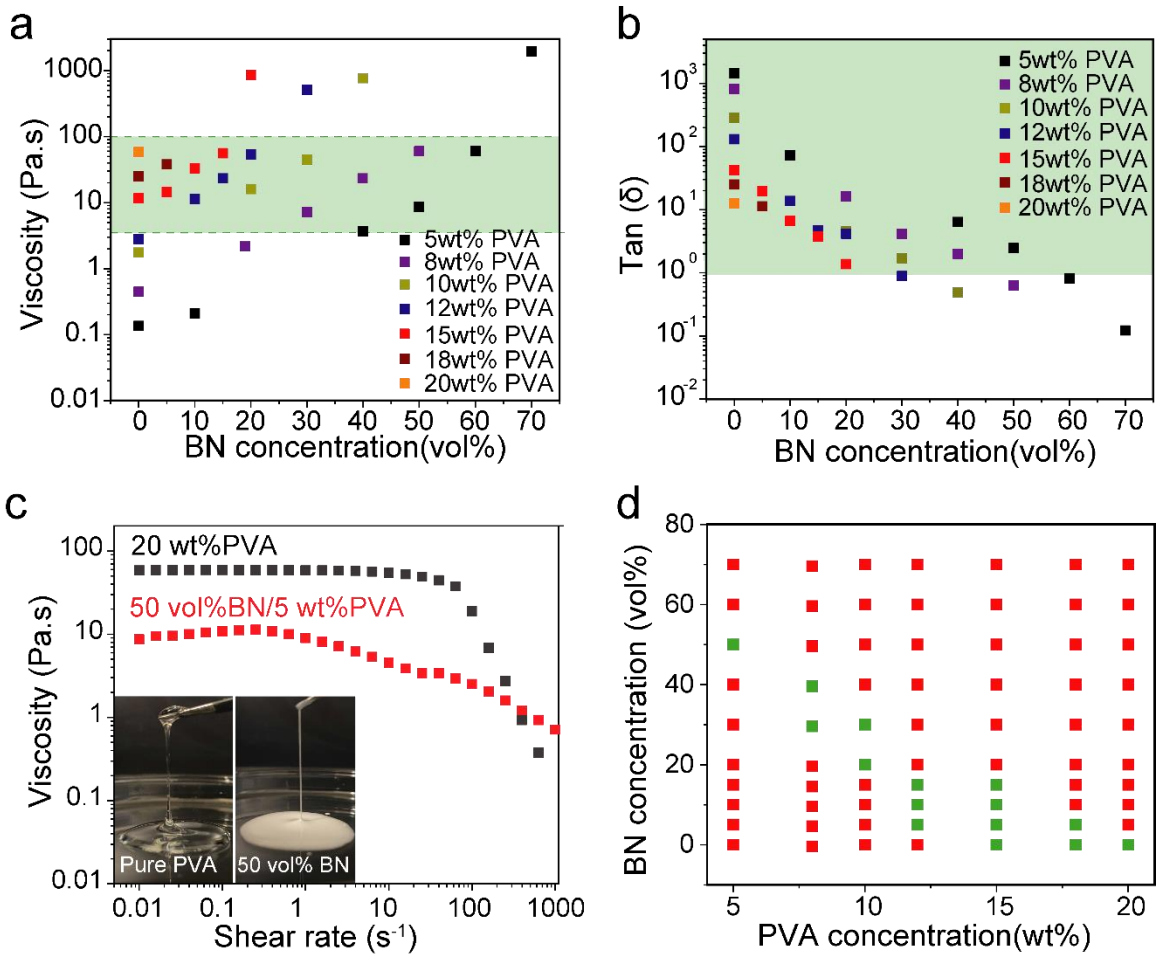

Figure 30. Composition optimization for spinnability and layer formation of (a) viscosity (b) tan(δ) at different BN and PVA concentrations. (c) Viscosities of pure PVA and BN/PVA suspensions, with inserts showing the fiber-pulling effects. (d) The fiber composition spinnable window where the green regime indicates success and red indicates failure.

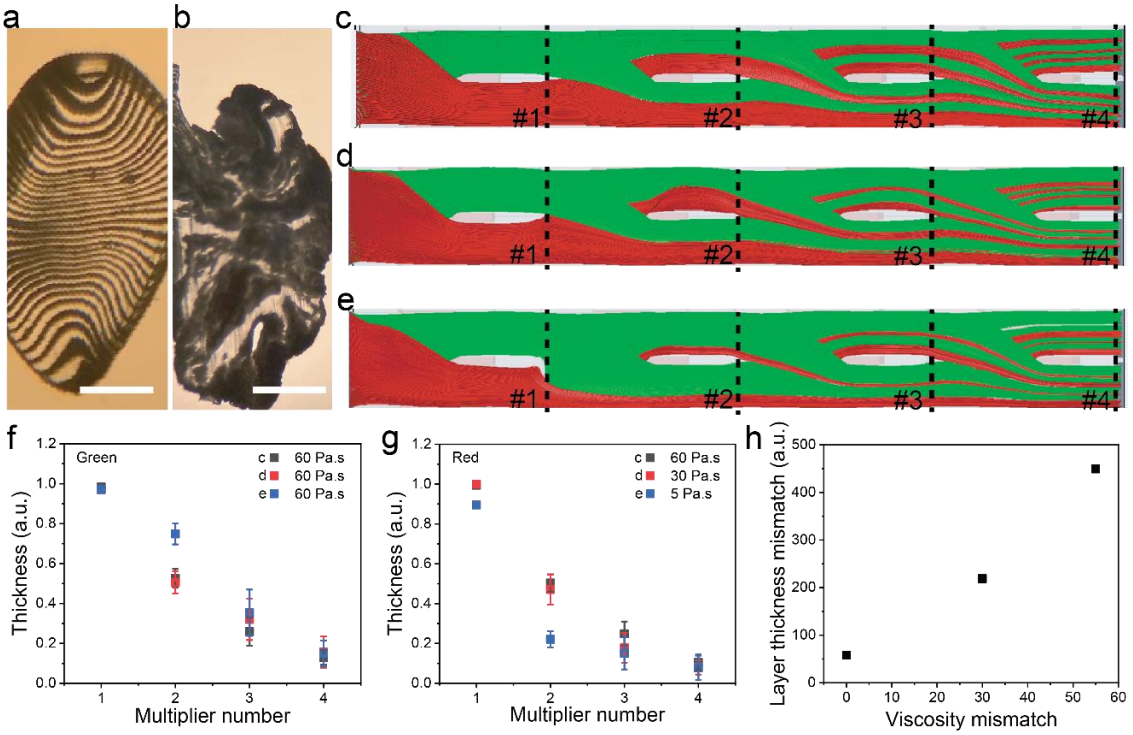

Figure 31. Layer formation morphology studies of a 64-layered composite with (a) distinct layers and (b) disrupted layers. Scale bars are 100 μm. (c-e) CFD simulation for different spinning dopes with viscosity mismatch of 0, 30, and 55 Pa·s. Measured layer thickness after each multiplier for (f) layer-1 (green) and (g) layer-2 (red). (h) Total layer thickness mismatch with respect to viscosity mismatch.

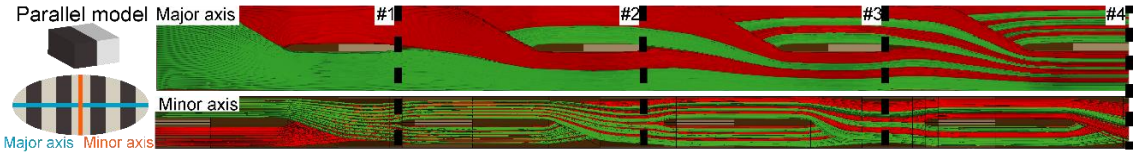

Figure 32 CFD simulations of the layer formability of the 16L10% fiber going through four multipliers (#1-4) as an example to produce layers consistent with the parallel model.

Green and red regimes indicate the PVA/DMSO solution and the PVA/BN/DMSO suspension, respectively.

DSC results show that the glass transition temperature (T_g) consistently increases with higher BN concentrations with uniform dispersion quality (Figure 33a). Peak T_g occurs at 30 vol% BN at 75.8 °C, which is 16 °C higher than the pure PVA. Due to the constraining effect at the polymer/nanoparticles interface, the addition of BN nanoparticles increases the rigidity of the PVA polymer chains and their resistance to thermal transitions (e.g., T_g). At 40 vol%, T_g slightly decreases, indicating a less efficient constraining effect. This weakened glass transition point could be caused by the increase of the BN to BN interfaces caused by particle agglomeration. Under the air atmosphere, BN is highly stable at elevated temperatures, and PVA would degrade at 800 °C. These conditions make TGA an accurate technique to measure the actual fiber composition. Figure 33b shows the degradation curves of 5 vol% (i.e., ~10wt%) fibers with layer numbers ranging from 4 to 64. Their weight residues have an average value of ~10wt% and a standard deviation of ±1.1%, showing high composition consistency during the layer multiplication and fiber spinning process. Based on the weight residue profile, there are mainly three degradation sections, i.e., evaporation of water molecule residue before 200 °C, decomposition of the PVA side chains starting at 300 °C, and decomposition of the PVA backbone chains starting at 550 °C.[198] Figure 33c shows the TGA curves of BN powder, pure PVA, 32L5%, 32L10%, and 32L20% fibers, and Figure 33d shows the slight differences between measured weight

residue with theoretically-predicted values, indicating precise layer composition control and structural consistency.

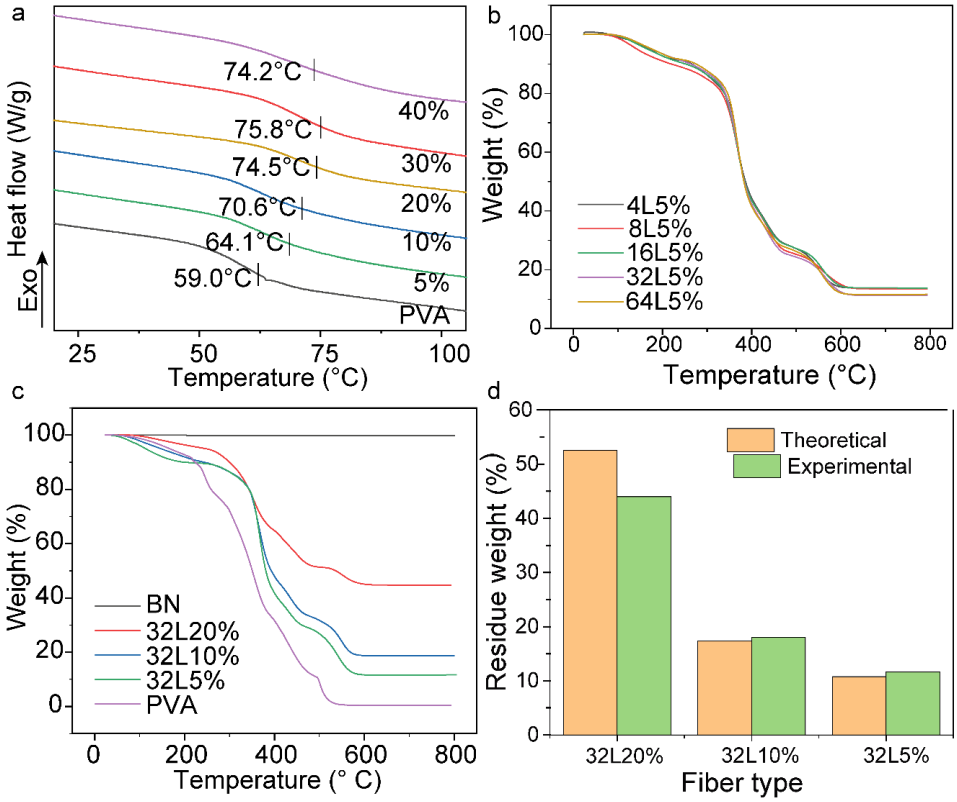

Figure 33. (a) DSC of T_g with increased BN vol%. TGA of fibers with (b) different layer numbers and (c) different BN vol%. (d) A weight residue comparison between the experimental and theoretical values of the 32-layered fibers.

4.4 Multilayer Morphologies

The thickness of the BN layer was reduced to half with each multiplier addition during fiber spinning. Figure 34 shows the experimentally measured and theoretically calculated layer thicknesses across the middle dotted line for the 4 to 64 layered undrawn fibers. The standard deviation gradually improves with increased layer numbers. After fiber drawing,

the layer thickness decreased further, reaching as small as 2 μm for the 128L10% fibers. After spinning, the designed rectangular nozzle enables an elliptical fiber shape with major and minor axes due to the drawing effects (Figure 35a). The cross-sectional SEM images of the 64L10% fiber confirm such a morphology after the hot drawing (Figure 35b). The size aspect ratio of the ellipse is ~1.5, where the lengths of the major and minor axes are 350 and 235 μm, respectively. This aspect ratio can be controlled by the nozzle shape design readily accessible via our 3D printed spinning setup; photographs of exiting nozzles with aspect ratios 1, 2, and 10 and their corresponding fiber cross-sectional SEM images with aspect ratios of 1, 1.5, and 2.5 are shown in Figure 36. For the 64L10% fiber, BN layers follow a periodic pattern across the major axis, with individual layers aligning along the minor axis (Figure 35c). Each layer's thickness approximately equals 4 μm, as shown in the colored regimes in Figure 35c. Within each layer, BN nanoparticles of sizes varying from 300 nm to 1 μm are interconnected to form thermally conductive pathways (Figure 35d). To further examine the fiber morphology and their channel continuity, micro-X-ray microtomography (micro-CT) was used for the undraw 8L10% (Figures $35e_1$-$35e_2$) and 16L10% (Figures $35f_1$-$35f_2$) fibers. Note that layer thickness smaller than 20 μm could not be observed via micro-CT due to voxel resolution and contrast limit. The continuous BN channels are highlighted in blue and purple, while the pure PVA channels are transparent (Figures 35e and 35f). The continuous channels indicate layer continuity and composition consistency along the fiber axial direction, consistent with the TGA characterizations (Figure 33b).

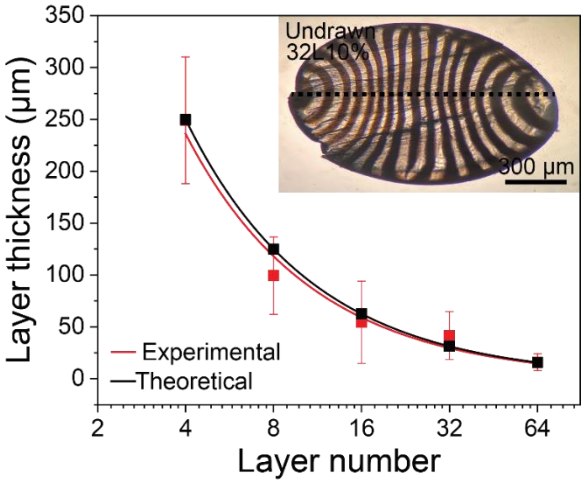

Figure 34. Experimentally measured and theoretically predicted layer thickness along the dotted black line with increased layer numbers.

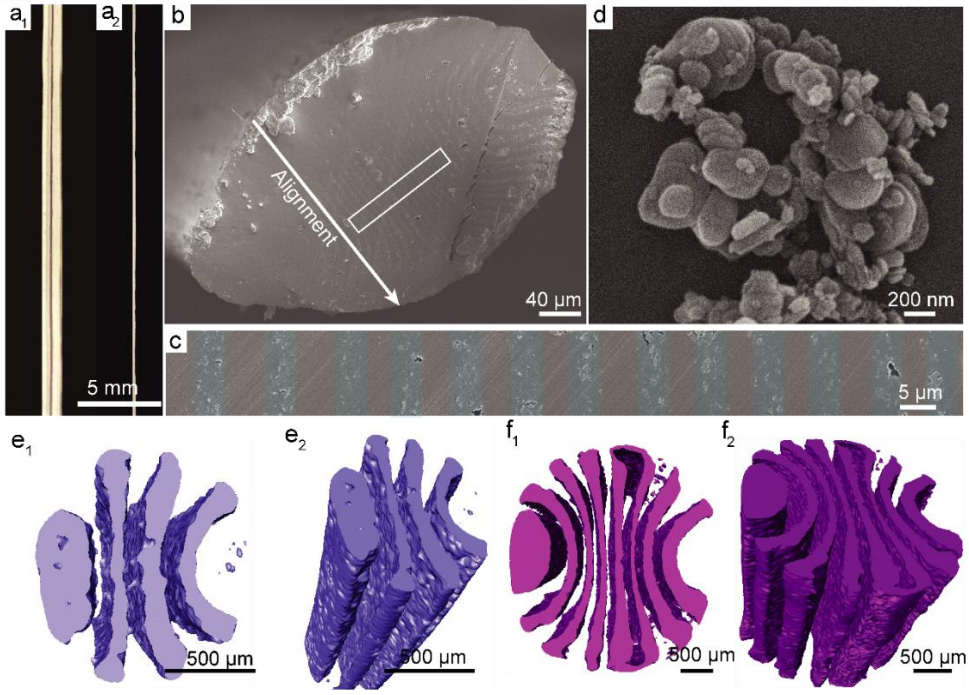

Figure 35. ($a_{1\text{-}2}$) Optical images of the as-spun 64L10% fiber from the major and minor axis, respectively. Cross-sectional SEM images of (b) the post-drawn 64L10% fiber with zoom-in regions showing the (c) BN layers with falsified coloring and (d) BN nanoparticle

morphology. Micro-CT images of the 3D continuous BN channels for (e_{1-2}) 8L10% and (f_{1-2}) the 16L10% fibers from the top and oblique views.

Nevertheless, the BN/PVA layers are curled the further they are from the central axis. It is believed that this curling of the layers could affect the fiber performance and is caused by the solvent exchange process during the coagulation of the fiber. Before the polymer gels exit the nozzle, the PVA and BN/PVA layers display well-defined layer-by-layer vertical patterns. As they exit the nozzle and enter the coagulation bath, the concentration gradient-driven solvent exchange process between the solvent (DMSO) and non-solvent (methanol) reshapes the fiber from rectangular to elliptical, which results in layers curling. The higher solvent concentration gradient at the fiber edge results in more layer curling, and the lower solvent concentration gradient at the fiber middle section results in less layer curling (Figure 34).

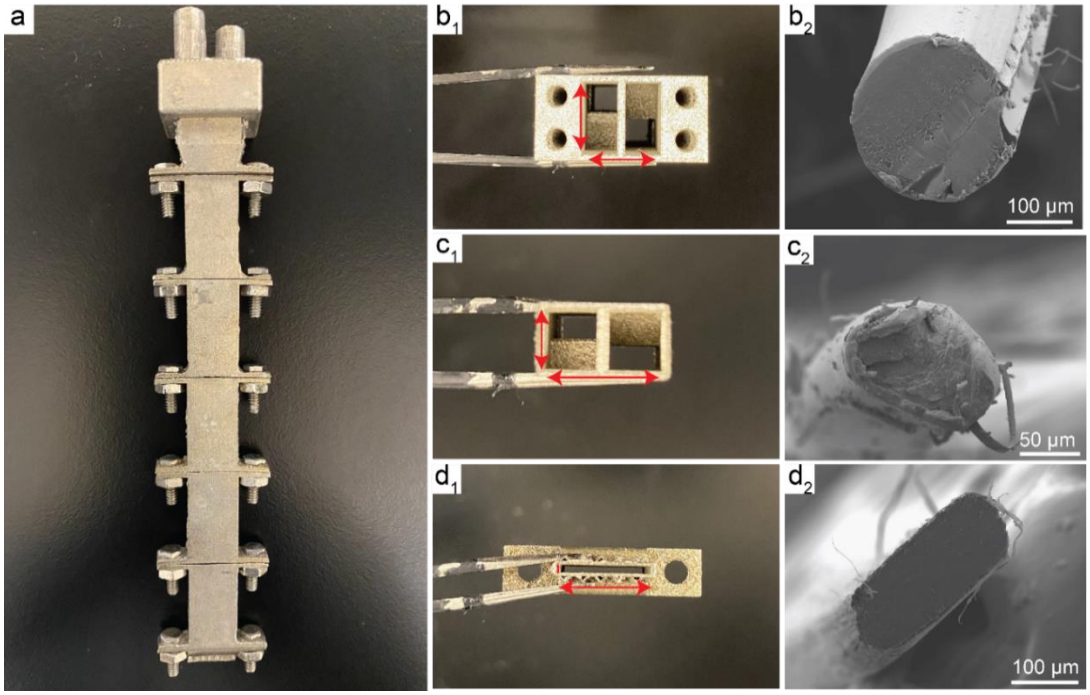

Figure 36 (a) Assembled nozzles with 5 multipliers. Exiting nozzle geometries with aspect ratios of (b_1) 1, (c_1) 2, and (d_1) 10, and their corresponding fiber cross-sectional SEM images with aspect ratios of (b_2) 1, (c_2) 1.5, and (d_2) 2.5.

4.5 Mechanical Properties

Hot drawing the fibers above their T_g is commonly used to align the polymer chains, reduce the fiber diameter (i.e., better size effects due to lower defect density), and increase structural properties.[20] During the fiber drawing process, the polymer chains reoriented themselves along with the fiber axial direction and increased their chain density, promoting better uniaxial mechanical properties (e.g., better anisotropic modulus and strength at 180 ^{o}C than 25 ^{o}C and 100 ^{o}C drawing, respectively).[199] Figure 37a shows the stress-strain curves for the post-drawn uniform fibers. The addition of BN, even at a 5% concentration,

results in weaker ultimate tensile strength performances; at a 40% loading, the tensile strength is reduced by about 77% (i.e., PVA vs. U5%-40% composites, Figure 38a). Note that the BN inclusion in this research (e.g., volume percentage 5%-40%) is higher than most literature reports,[200] and we do not expect higher mechanical properties as BN-BN interfaces do not transfer stress efficiently according to composite mechanics.[201] Similarly, fracture strain values also decrease with increased BN particle loading (Figure 37a). Micro-CT scan imaging shows trails of voids along the fiber axial direction after the drawing process (Figure 39), which are likely the leading cause of lowered tensile strength (Figure 38a). Their formations have resulted from the polymer chain movement when the shear stress generated during the fiber drawing process could not overcome the momentum needed to exfoliate/redistribute the large BN clusters. Another cause could be the higher T_g of BN-containing fibers as their polymer chain mobilities are more resistant to drawing temperatures. Therefore, an additional drawing step at 180 °C was used (Figure 38b). As a result, for pure PVA fibers, the percentage increase in strength from 100 °C to 180 °C is almost negligible; however, for the U10%, U20%, and U30% fibers, the increments are 19.7%, 54.7%, 80.5%, respectively (Figure 38b). Although the performance gaps between the BN-containing and pure PVA fibers become narrower at higher drawing stages, additional loading of BN nanoparticles still deteriorates fiber strength. Young's modulus is less affected by the addition of BN; a 10% increase is observed for the U5% fiber, and a 25% decrease is observed for the U30% fiber (Figures 38c and 38d). A noticeable 64% decrease is observed as BN volume concentration increased to 40%, which was expected as previous DSC data suggested the higher BN/BN interfaces, resulting in lower load

transfer efficiency.[202] Through the multilayering process, selective spatial deposition of the BN nanoparticles was controlled as they occupy half of the fiber volume. At equal BN loadings of 10 vol% and 20 vol%, layered composites show lower Young's modulus and ultimate tensile strength than uniformly structured fibers (i.e., U-type fibers, Figure 37b). For example, 32L10% fiber's mechanical properties, in terms of Young's modulus and ultimate tensile strength, are 7.2% and 21.3% lower than that of the U10% fiber, respectively, which is consistent on the rule of mixture calculations.[96,203]

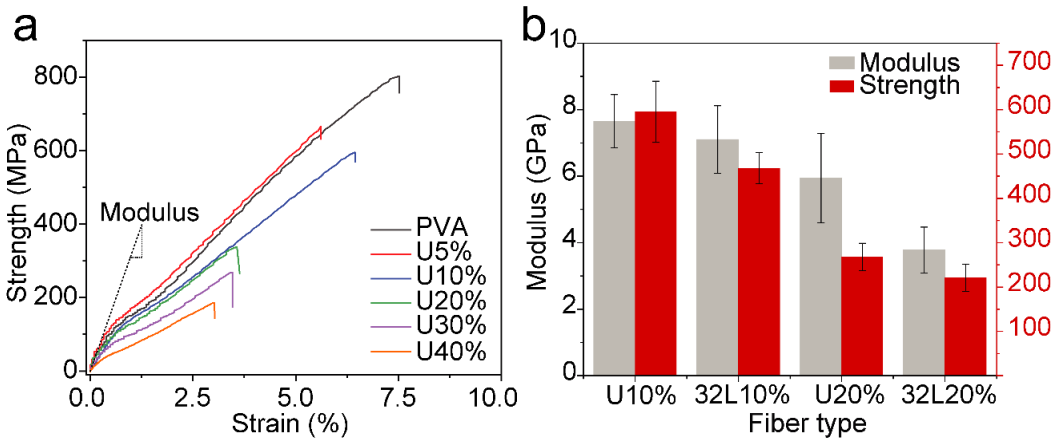

Figure 37. Mechanical properties of uniform and layered fibers (a) Stress-strain curves of uniform fibers after drawing at 100 °C. (b) Young's modulus and ultimate tensile strength between the uniform and 32-layered fibers after hot drawing at 100 °C.

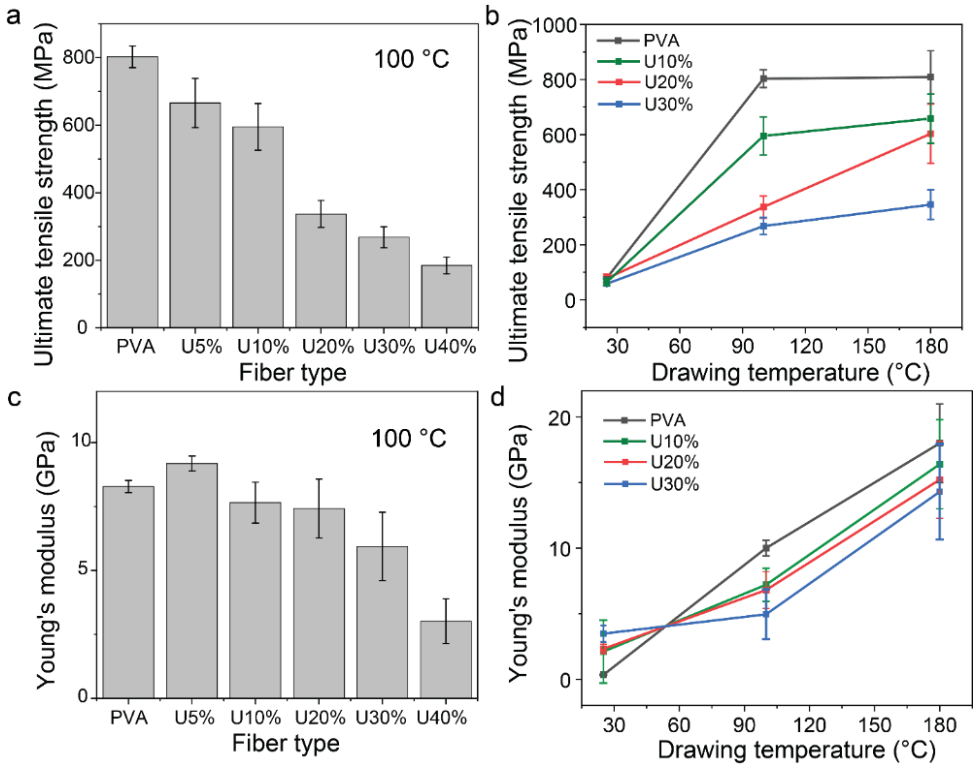

Figure 38. Mechanical properties of uniformly structured fibers drawn at 25 °C, 100 °C, and 180 °C. (a and b) The ultimate tensile strength and (c and d) Young's modulus.

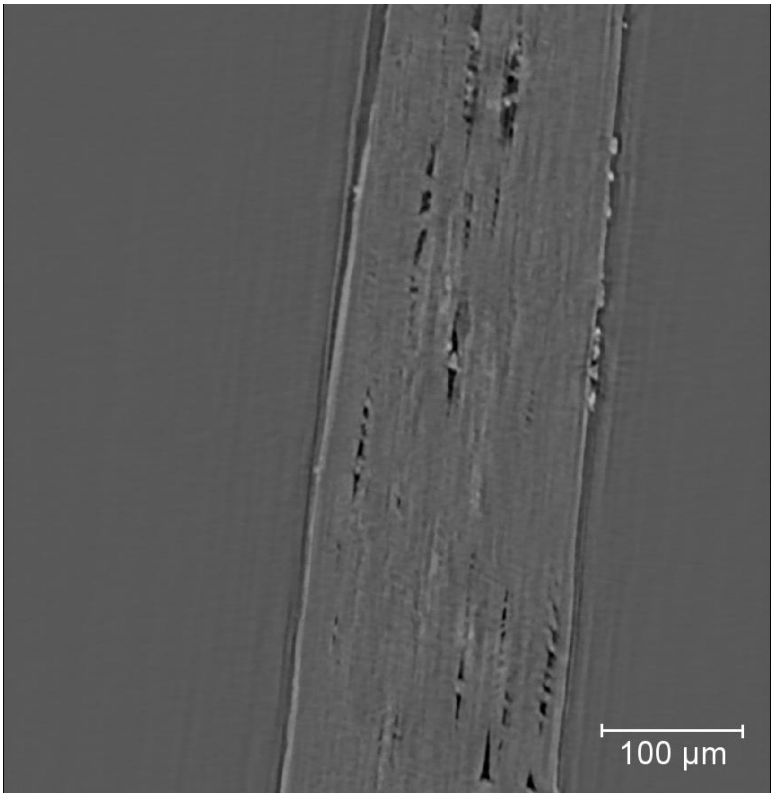

Figure 39. Micro-CT scan for the U20% composite fibers with voids as defects after hot drawing.

The relationship between layer numbers and mechanical properties was further investigated; the 32L10% fiber peaks both modulus and strength performances by 68% and 5% increases compared to the 4L10% fiber, respectively (Figure 40a). Finite element modeling (FEM) simulation was conducted on a composite consisting of alternating layers with different stiffnesses, fixed bottom layers, and uniformly distributed force on the top surface (insert figures in Figure 40b). Since both layers consisted of PVA as the polymer

matrix, their interface was assumed to be perfectly bonded at the initial deformation. The simulation results show that the total deformation on the surface reduces with reduced layer thicknesses (Figure 40b), inferring an increased interfacial interaction would increase the composite stiffness. Similar mechanical behaviors have been observed in previous composite laminates with varying thicknesses of metal alloys.[204]

Moreover, the stress-strain profiles for the 32L10% fibers show stepwise fracture behavior (Figure 40c and 40d) at both fibers drawn at RT and 100 °C, respectively. The stress-strain profiles of the layered fibers show a significant difference from the U10% fibers, where a linear elastic response is observed until a catastrophic failure (Figure 37a). SEM images show two distinct types of fractures. For instance, for the 32L10% fiber, the BN/PVA layer fails in a brittle fashion showing a clean-cut cross-section, while the PVA layer fails in a ductile fashion with a fiber bridging phenomenon (Figure 40e). Figure 41 shows similar behaviors for the 4L10% and 8L10% fibers compared to pure PVA fiber. Based on this observation, it can be concluded that the BN/PVA layers are subjected to the mechanical tension within the elastic regions at first, followed by an extension of the PVA layer in a plastic zone until the complete fracture. This alternating layered structure could be one of the ways to increase the pseudo-ductility of high modulus fibers. Moreover, the alternating layered structure also shows crack deflection behavior. An initial crack was introduced manually to both pure PVA and 32L10% fibers, and upon 4% strain, two fibers show noticeable differences (Figure 42a_1-42a_3). Unlike PVA fiber, 32L10% fiber inhibits crack propagation by deflecting its direction in the axial direction rather than across the fiber. It is worth mentioning that for the 32L10% fiber drawn at room temperature, approximately

24% of the total energy absorbed is succeeding from the beginning of the stepwise fracture (Figure 40c). This enhanced fracture resistance is likely due to the different mechanical properties between the layers, resembling the previously reported interlayer technique in laminates for toughness improvement.[203] Interestingly, as layer number increases, the percentage of fibers under tensile test showing step-wise fracture characteristic decreases, 100% for 4L10%, 60% for 32L10%, 20% for 64L10%, and 0% for 128L10% (Figure 43). This implies that the fiber gradually transformed from a multilayered composite with increased layer numbers to a more uniformly-phased composite.

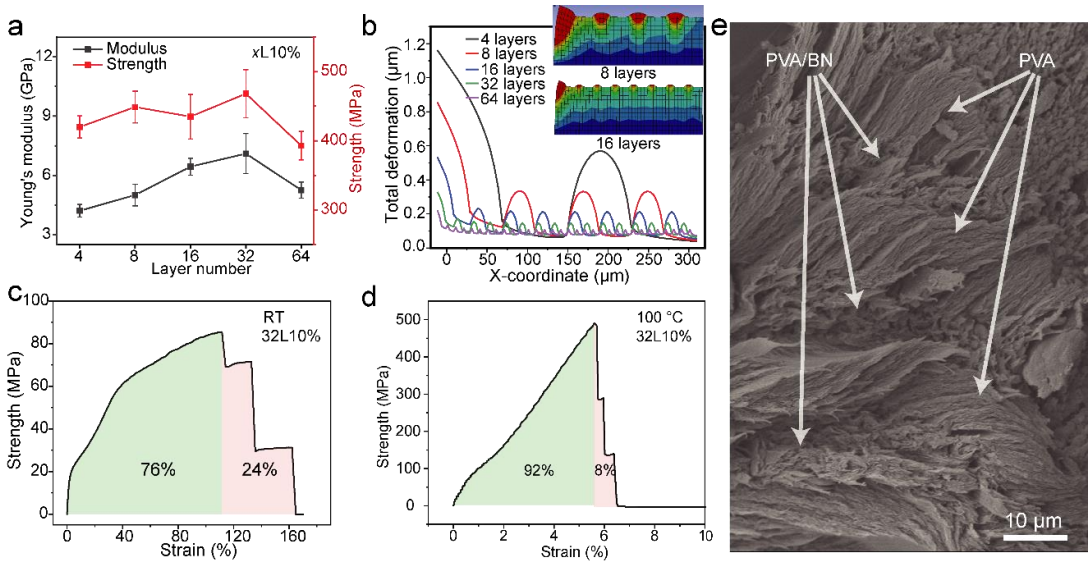

Figure 40. Mechanical properties of layered fibers. (a) Relationships of Young's modulus and ultimate tensile strength values with different layer numbers. (b) Deformation simulations of fibers with different layer numbers via FEM. The stress-strain curve of 32L10% fibers drawn at (c) room temperature and (d) 100 °C with stepwise fractures. (e) SEM images of the 32L10% fibers showed distinct surface morphologies within the PVA and PVA/BN layers during fracture.

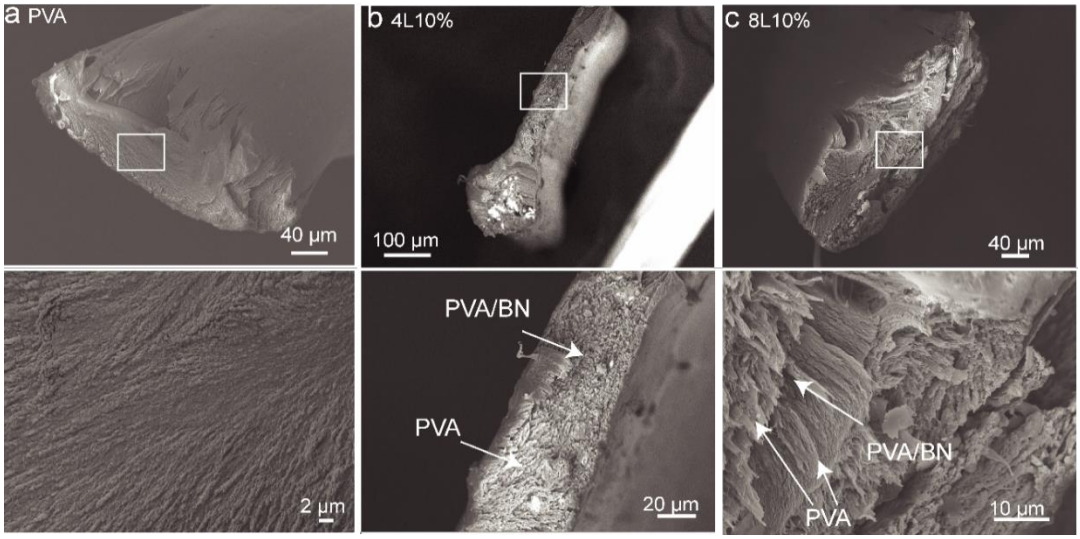

Figure 41. Fractured fiber morphologies of the (a) pure PVA, (b) 4L10%, and (c) 8L10%, fibers (top) with zoomed-in sections (bottom) showing the brittle and ductile fracture morphologies.

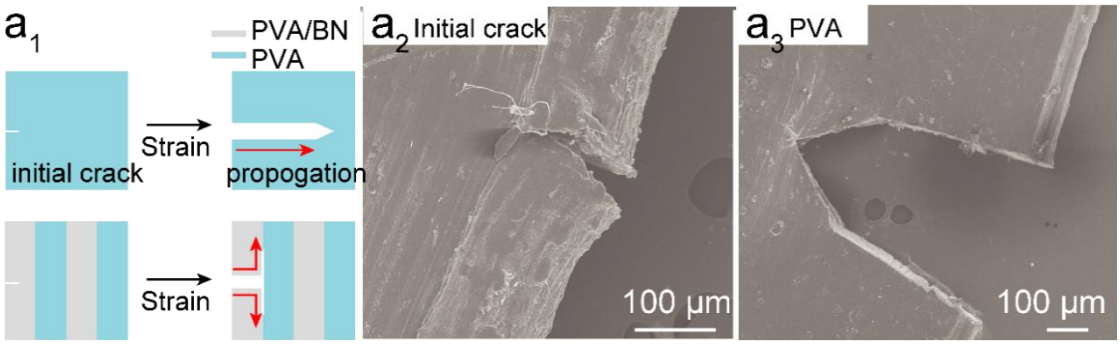

Figure 42. (a_1) Schematics showing the crack propagation route with (a_{2-3}) the SEM images of propagated cracks in PVA and 32L10% fibers, suggesting that the BN-containing layers served as crack barriers or reflectors.

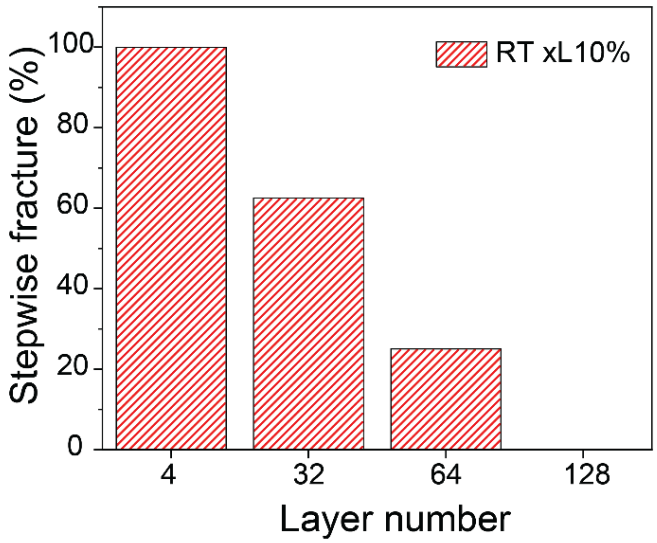

Figure 43. 10vol% BN loaded fibers with their stepwise fracture probability.

4.6 Parallel Model for Thermal Conductivity

The unique layers can facilitate directional heat dissipation or conduction. By assuming that the BN/PVA composite phase follows the Maxwell-Eucken model, a Parallel-Maxwell-Eucken model for the thermal conductive composite was proposed according to 4.3 and 4.4 (Figure 44a) because of the parallel combinations of layers, where k_p, k_m, k_n, k_2 are the thermal conductivities of the composite layers, polymer matrix, nanoparticle, and polymer/nanoparticle phase, v_n is the volume fraction of the nanoparticles, and v_2 is the volume fractions of polymer/nanoparticle phase which was assumed to be 0.5.[187]

$$k_p = k_m(1 - v_2) + k_2 v_2 \tag{4.3}$$

$$k_2 = k_m \frac{2k_m + k_n - 2(k_m - k_n)v_n}{2k_m + k_n + (k_m - k_n)v_n} \tag{4.4}$$

The overall composite's highest nanoparticle volume concentration was limited to 50%, corresponding to a 100% theoretical nanoparticle volume in the composite phase.

Experimentally, only 40 vol% nanoparticle loading was achieved, corresponding to 20 vol% loading in the overall fiber. The calculation shows that layered fibers are 34% higher in thermal conductivity than uniform fibers at this concentration. Due to the challenges in experimentally measuring the thermal conductivity of anisotropic fibers, a transient plane source (TPS) method was used to estimate the thermal conductivity of rectangular bulk composites with different BN loadings,[205] followed by finite element analysis (FEA) to validate the relationship between thermal response and layer numbers computationally.

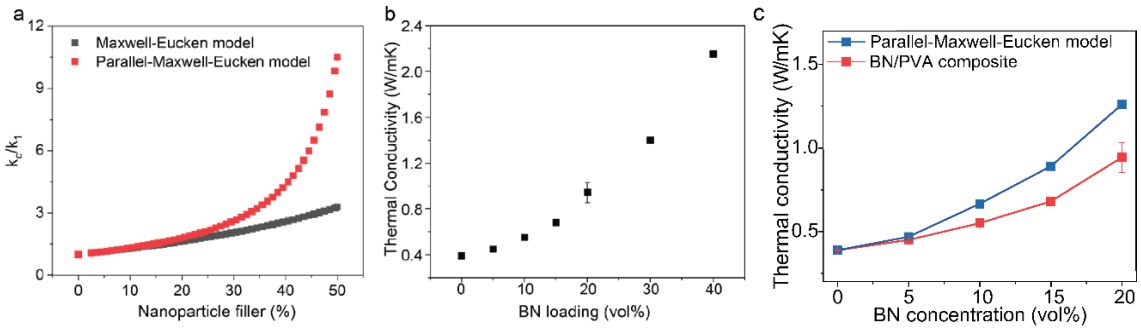

Figure 44. Thermal conductivity calculation and measurements. (a) The thermal conductivity is predicted based on the Maxwell-Eucken and Parallel-Maxwell-Eucken models.[2] (b) Measured thermal conductivity of the bulk samples with increasing BN vol% from the TPS method. (c) Theoretical thermal conductivity calculation of layered structure compared to experimental values in (b).

The TPS method uses a thin metal film sandwiched between two identical composite samples to generate Joule heat and records the transient temperature response to estimate the thermal conductivity.[205] According to the measurement, the thermal conductivity increase monotonically and non-linearly with BN volume concentrations from 0%, 5%,

10%, 15%, 20%, 30%, to 40% (Figure 44b). The thermal conductivities between uniform (i.e., along with the channel directions, red in Figure 44c) and layered composites (i.e., from the Parallel-Maxwell-Eucken model as plotted blue in Figure 44a) show a more efficient heat dissipation for layered structures. For example, the thermal conductivity of the uniform BN/PVA and layered samples at a 20% BN loading is 0.94 W m^{-1} K^{-1} and 1.26 W m^{-1} K^{-1}, respectively; a 34% increase for the layered structures. Similarly, to achieve a conductivity of 0.94 W m^{-1} K^{-1}, 20% BN is required for a uniform composite, while only 15% BN is required for a layered structure (Figure 44c). The thermal conductivity of a two-phase system depends not only on nanoparticle loading but also on the microstructure. After sintering the fibers at 800 °C, Figure 45 shows a clear image of the bare BN layers, consistent with the micro-CT images (Figures 35e-f); the preferentially aligned BN channels act as high-ways for phonons to transport with a reduced scattering across boundaries.[188,189] On the other hand, homogeneously dispersed BN nanoparticles can be pictured as randomly distributed networks intercepted with local junctions, posing thermal dissipation and structure densification challenges.[206] Furthermore, the non-linear relationship between the BN concentration and thermal conductivity predicts that such microstructure would be exponentially more effective as BN content increases.

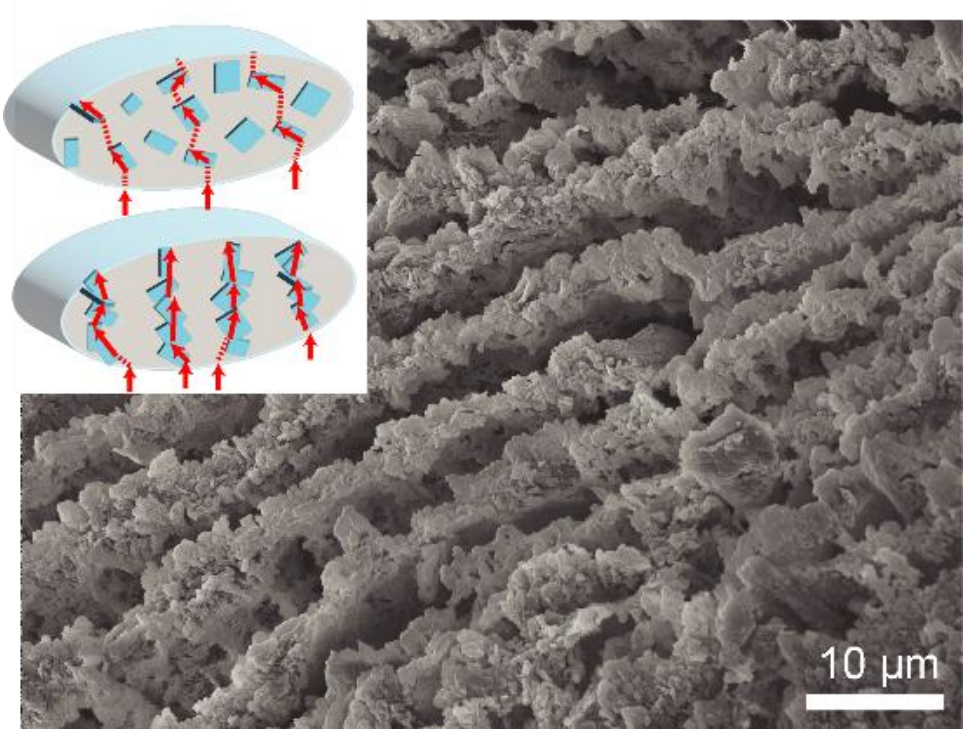

Figure 45. Schematic illustration of the proposed thermal conductive pathways for uniform (the top insert) and layered (the bottom insert and the SEM image) fibers.

FEA was used for layered composites to better understand the thermal profiles influenced by layer numbers. The experimentally measured thermal conductivity values of bulk PVA (0.38 W m^{-1} K^{-1}) and 40 vol% BN/PVA (2.15 W m^{-1} K^{-1}) were used for the alternating composite layer simulations. For comparison purposes, the bulk conductivity of 20 vol% BN/PVA was selected as the uniform composite. Under equal heating power (i.e., thermal field applied to the bottom fiber surfaces) and convection occurring on all other three edges, a higher thermal conductivity would result in a lower temperature difference across the conduction path; in other words, a higher surface temperature in this FEA simulation correlates to higher thermal conductivity.[207] Figure 46a shows the simulation results as

thermal contour maps, and Figure 46b shows the profiled top-surface temperature along with the x-coordinate. As layer number increases, additional interfaces would replace the previous PVA-PVA interconnections with new BN-PVA interconnections, hence increasing the interfacial conductivities (Figure 46d). In addition, the decreased layer thicknesses also result in a more uniform top surface temperature profile across alternating layers (e.g., 64L20% vs. 4L20%, Figure 46b). The average fiber body temperatures of 5 vol%, 10 vol%, 15 vol%, and 20 vol% layered BN/PVA fibers are compared with the uniformly structured fibers as summarized in Figure 46c. Layered structures show an apparent temperature increase at all BN concentrations, especially at higher BN vol%. Interestingly, the temperature increase eventually smoothed out with increased layer numbers. One possible explanation is that the new interfaces not only create BN-PVA interconnections from PVA-PVA interconnections but also destroy BN-BN interactions to form BN-PVA networking, causing a decrease in the thermal conductivity of the replaced BN/PVA layers (Figure 46e). As a result, the minimum temperature increases for the PVA layers with increasing layer numbers and the maximum temperature decreases for the BN/PVA layers.

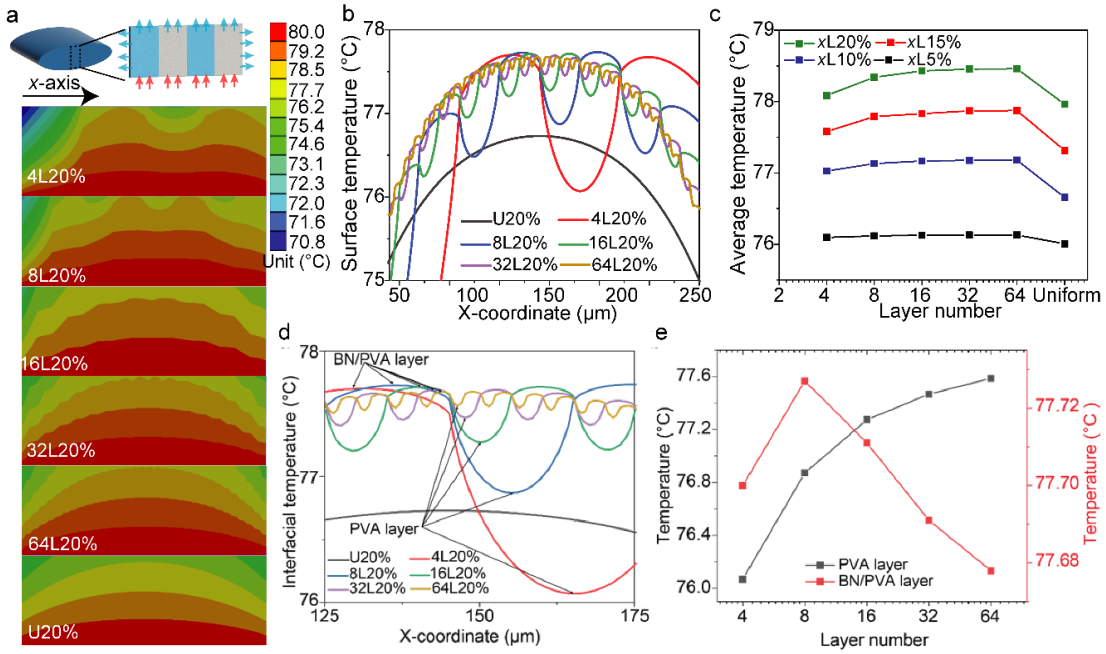

Figure 46. FEA of thermal behaviors of the multilayered fibers. (a) Simulation result of 20 vol% BN/PVA fibers with different layer thicknesses with (b) top surface temperature profiles and (c) averaged overall fiber temperatures. (d) A zoomed-in section of b with arrows indicating the minimum and maximum temperatures of the PVA and BN/PVA layers, respectively, and (e) shows the temperature changes with layer numbers.

For application demonstration purposes, pure PVA and 32L20% fibers were handwoven into fabrics (5 cm by 5 cm in size) (Figure 47a) and placed on a Peltier plate as a heat source to test their time-temperature responses in an ambient environment. All fibers maintained a stable structure as their major axes were in contact with the heat source, aligning the BN heat pathways with the conducting direction (Figure 45). The high aspect ratio of the fiber ensures such geometry after weaving without any additional precautions (Figure 36). After the temperature stabilized, a series of infrared images were taken from

0 °C to 50 °C at a temperature step of 10 °C min^{-1} (Figure 47b). The 32L20% fiber surface shows a lower starting temperature and a higher final temperature, and its absolute temperature difference between the heat source is lower than the pure PVA textile, indicating improved thermal conductivity. Moreover, the PVA, 32L10%, and 32L20% fabrics were tested under 1, 2.5, 5, and 10 °C min^{-1} heating rates to test the dynamic thermal conduction property. Three layers of each fabric were stacked together with a thermocouple attached on the topmost surface with silver paste to increase their temperature contrast (bottom schematic in Figure 47c). The heat source profile was programmable (top schematic in Figure 47c) with a 10 min steady-state period after each heating ramp. The thermal responses show that slower heating rates and higher BN concentration result in faster responses and vice versa (Figure 47d). Furthermore, the responses of single layer pure PVA and 32L20% fabrics under cyclic heating also show that the process is highly reversible between 0 to 80 °C (Figure 47e), indicating a large working window with mechanical robustness and material sustainability.

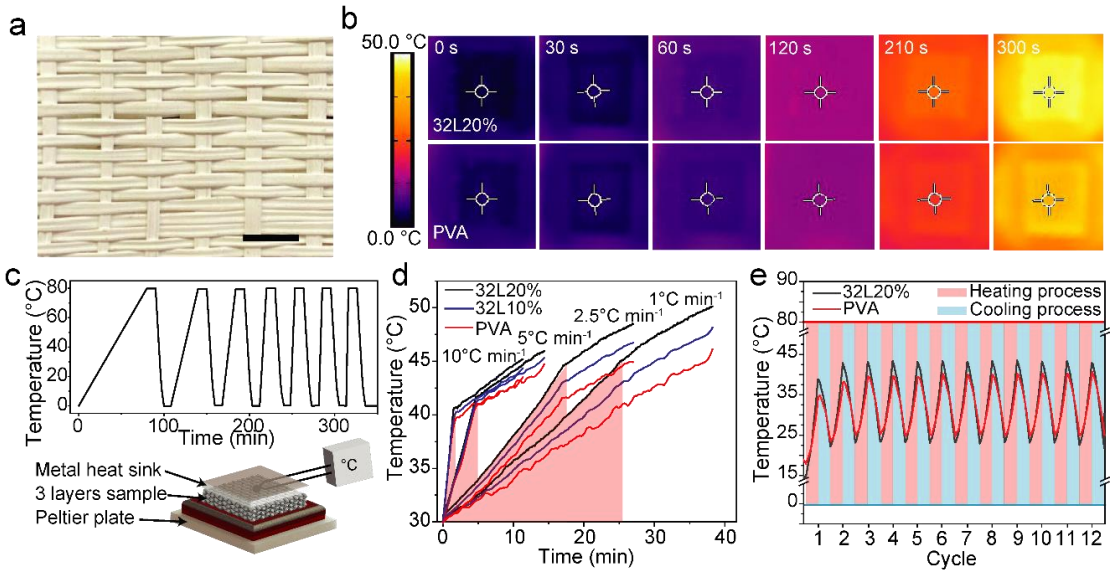

Figure 47 (a) Handwoven 32L20% fiber fabric (scale bar 2 mm) showed the thermal response differences between (b) 32L20% fabrics (top) and pure PVA fabrics on a Peltier plate (bottom). (c) An experimental setup (bottom schematic) with programmable heating rates (top figure) for measuring (d) static and (e) dynamic thermal responsiveness of the 32L20% and PVA fabrics.

4.7 Further Application Demonstrations

The layer multiplying technique applies to different material systems with varying manufacturing resolutions or versatile functionality. In addition to forming parallelly-packed, thermally-conductive pathways with BN nanoparticles, two other applications were briefly explored to show the general compatibility of our method with composite or hybrid materials. First, the alignment of channels can be controlled to construct parallel layers and series layers (the left schematic in Figure 48a) with potential for thermal insulation applications as predicted by Figure 28a. A CFD simulation shows that by

reversing the injection direction of feedstock A and B across four multipliers, 16 alternating layers can be generated perpendicular to the minor axis direction (the right contour mapping in Figure 48a). As an example demonstration, material A was chosen as polyacrylonitrile (PAN), and material B was chosen as aluminum (Al)/PAN. After patterning the Al particles in a series sequence (Figure 28b$_1$), these metal powders were etched away to form pores aligned along the fiber major axis (Figure 28b$_2$) with a layer thickness between 5-10 μm (Figure 28b$_3$). Similar to the Parallel/Maxwell-Eucken coupled model, a Series-Maxwell-Eucken model was proposed based on Equation 4.5,

$$k_s = \frac{1}{(1 - v_2)/k_m + v_2/k_2} \tag{4.5}$$

where v_2 is the volume fractions of pores/polymer phase, k_m is the thermal conductivity of the polymer matrix, and k_2 is the thermal conductivity of the pores/polymer phase based on Equation 4.4.[187] With varied porosity that introduced the insulation space, Figure 48b$_4$ shows the thermal conductivities of fibers with pore-patterning (Series-Maxwell-Eucken model) and uniform pore distributions (Maxwell-Eucken model), implying greatly improved insulation efficiency via forming a higher porosity or concentrated pores within layers.

Apart from forming multilayered composites based on a single type of nanoparticle, the bi-nanoparticle laminate structure can also be feasible with the layer multiplication strategy, such as in cellulose nanocrystal (CNC)/ cellulose nanofiber (CNF) stack films for structural coloration,[208] BN/graphene as dielectric nanocomposite,[209] or carbon nanotube (CNT)/BN for electromagnetic shielding application.[210] For a brief demonstration, BN

and graphene nanoplatelets (GNPs) were mixed with PVA polymers as a binder to form 8 alternating layers (Figure 48c$_1$), with each layer thickness of 20 μm (Figure 48c$_2$). Higher GNPs concentrations increase the electrical conductivity after reaching the percolation threshold (5 wt%) along the fiber axial direction (Figure 48c$_3$). On the other hand, the electrically insulative BN nanoparticles prevent electron transport across the fiber (Figure 48c$_3$), resulting in over seven orders of magnitude difference in electrical conductivity between the along-fiber and perpendicular-to-fiber directions. Furthermore, previous research suggests that instead of forming a homogenous mixer, a bilayer structure of graphene and BN results in enhanced thermal conductivity due to the higher interfacial thermal conductance between the homogeneous nanoparticle interfaces, such as BN/BN or graphene/graphene, than that of the BN/graphene interface, based on molecular dynamics simulations.[209,211]

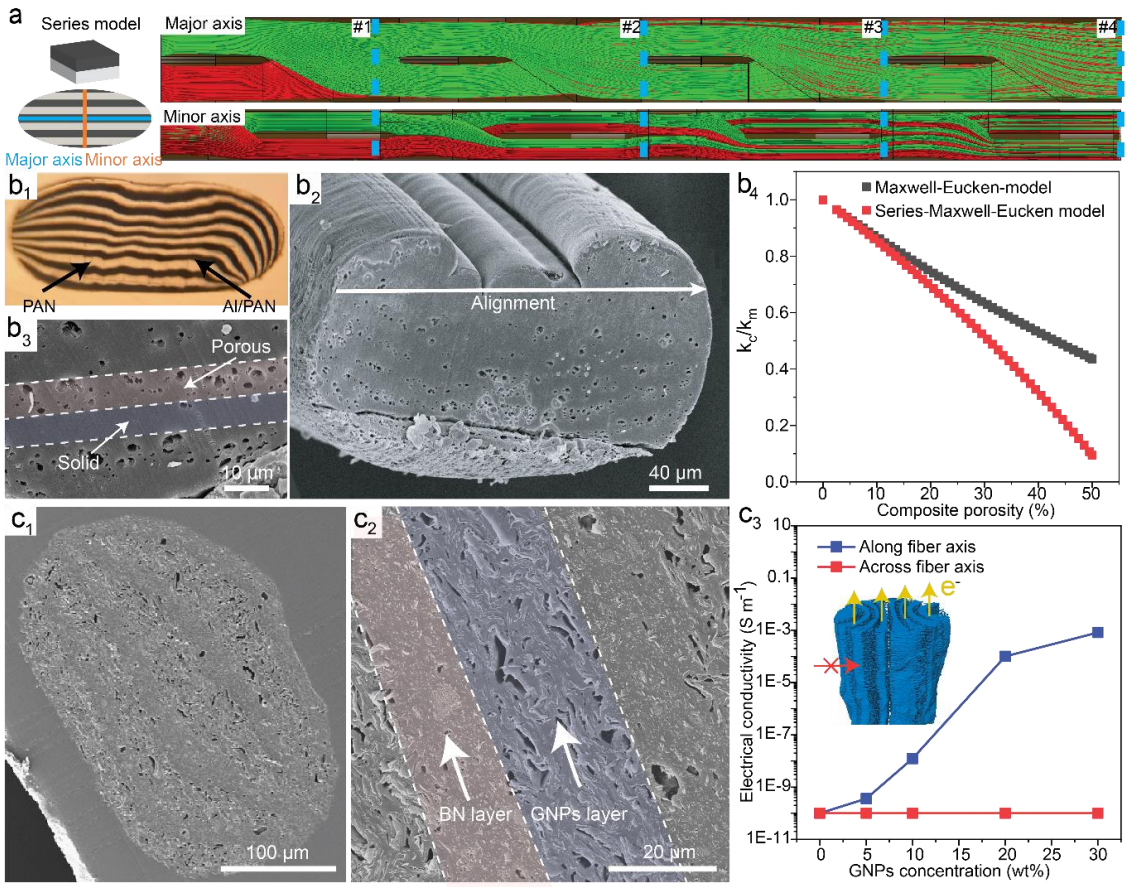

Figure 48. Potential applications of the fiber layering technique. (a) A CFD simulation of layer formability in the Series model. (b_1) An optical image of the layered Al/PAN fiber, (b_2) SEM imaging of the porous PAN fiber where the pores created by etching Al metals are aligned along the major axis direction. (b_3) A zoomed-in SEM image of the pores-aligned layer and solid layer regions. (b_4) Predicted thermal conductivity values based on the Series-Maxwell-Eucken model.[187] (c_{1-2}) SEM images of alternating layers in BN/GnPs composite fibers. (c_3) Measured anisotropic electrical conductivity of the thermally conductive fiber along and across the fiber axial direction.

4.8 Conclusion

This research reports the first time use of a new fiber spinning technique for the simultaneous nanoparticle assembly to enhance structural patterning or functional properties in nanocomposites. With rapidly prototyped components in an in-house designed layer multiplying technique, this research demonstrated the feasibility of alternating layers containing different nanoparticles (e.g., BN, Al, BN/GNPs) selectively distributed with preferential alignment. With well-controlled flow behaviors, microscale layered structures are fabricated for versatile applications. Composite layers can be designed with enhanced resistance to crack propagations (e.g., the PVA-BN/PVA layers). These nanocomposites show programmable and directional heat dissipation capabilities by simply controlling layer number and thickness (i.e., 2 μm to 65 μm). Second, the alternating layers' composition (e.g., different polymer/nanoparticle combinations) and structure (e.g., horizontally packed or vertically laminated) can be tailored depending on specific applications. For example, porous channels are selectively created via etching metal powders within specific layers, and ceramic hybrids are readily prepared as anisotropic conductors. At last, this manufacturing technique establishes a new mechanism in textile engineering that can be easily transferred and combined with other fabrication methods, such as knitting/weaving, coating/extrusion, direct ink writing, or fused deposition modeling, for scalable devices or systems, as demonstrated in our thermal-regulating fabrics.

CHAPTER 5

NANOSCALE PATTERNING AND MORPHOLOGY CONTROL OF CARBON NANOTUBES IN COMPOSITE FIBER

5.1 Introduction

Chapter 4 introduces utilizing fluidic materials' rheological behavior to generate microscale features beyond the resolution limitation of 3D printed nozzles. In this Chapter, the same layering technique is explored further with finer nanoparticle pattern resolution and the ability to control individual nanoparticle orientation at the nanoscale.

Nanoparticle-filled polymer composites have been extensively researched in the past few decades due to their unique functional properties, durability, and chemical stability. Among these, carbon nanotubes (CNTs) have garnered attention for their high flexibility, large aspect ratio (>1000), high intrinsic elastic modulus (~1000 GPa) and strength (~100 GPa),[212] and high electrical (1800 s cm^{-1})[213,214] and thermal conductivities (3000 W $m^{-1}K^{-1}$).[215,216] The combination of these properties makes CNTs the ideal nanofillers for various polymer composites for diverse applications, including, but not limited to, mechanically reinforced fibers and films, sensors, actuators, electronics, additive manufacturing, and energy storage devices.[202,217–222]

The performance of functional CNT-composite materials is heavily dependent on the control of the CNTs' microstructure, including location deposition, dispersion quality, and nanoparticle alignment at the nanoscale. The precise alignment of individual nanotubes or their bundles remains a challenge within current mainstream strategies of simple blending

or mixing for nanoparticle dispersion.[223] In particular, the presence of strong interaction forces in CNTs leads to the formation of clusters and aggregates. Traditional methods of physically dispersing the CNTs via mechanical protocols, such as sonication and mixing, have been used in the past mostly for polymer composites due to their simple setup and procedures. In these methods, the amount of energy applied had to be slightly higher than the binding energy between the CNTs and lower than a level severe enough to fracture them.[224] As a result, an improved dispersion quality is often accompanied by a lower nanoparticle aspect ratio, limiting the reinforcing efficiency.[225,226] In addition, due to the anisotropic properties of CNTs, their functionalities can be fully exploited only if their long-range locational and orientational orders are delicately controlled. Due to the impurities from various synthesis methods (e.g., metal catalyst residue from chemical vapor deposition), commercially used CNTs are usually curled and twisted, resulting in further challenges in controlling their orientation inside soft macromolecules.[227] As previously mentioned in Chapter 1, techniques such as electrical field,[228] magnetic field,[84] acoustic,[229] shear flow assistance,[82] and self-assembly,[89] have been recently developed for nanotube anisotropy in 2D films or 3D composites. However, in the case of 1-D polymer composite fibers, most nanoparticle alignment methods are still limited to traditional polymer drawing or stretching.[81,230]

Carbon fiber is a vital and excellent reinforcing material for composites because of its higher strength, higher modulus, and relatively lower density. PAN has been the most frequently used precursor to carbon fibers, including those used in CNT-reinforced and PAN-based carbon fibers. However, the high loading of CNTs often results in defects due

to limited orientation and nanoparticle aggregation, so it is necessary to develop a better method to control CNT conformations.

In this study, The same layering technique as Chapter 4 is applied to fabricate hierarchically structured CNT/PAN composites with highly aligned nanotubes (hierarchy level 1, ~20 nm) and alternatively packed nanolayers (hierarchy level 2, ~170 nm) in microscale fibers (hierarchy level 3, ~80 μm). Our innovative fiber spinning technique uses the forced assembly method where the two polymer solutions (i.e., PAN and CNT/PAN) first enter a 3D-printed multiplier die side-by-side and then are physically separated along the horizontal direction (top-down) and repositioned along the vertical direction (right-left). Ultimately, the nanoscale-patterned geometry has successfully led to highly homogeneous CNT distributions through their physical confinement by the adjacent polymer channels. Furthermore, with the increase of layer interface areas, CNTs between adjacent layers have also shown enhanced alignment due to shear stress. The resulting fiber with 512 layers demonstrated the best mechanical properties, including a 27.4% increase in modulus and a 22.2% increase in strength compared to the traditional CNT/PAN mixing method and a 46.4% increase in modulus and 39.5% increase in strength compared to pure PAN fiber. The introduction of the multilayer pattern contributes to the overall hierarchal structure, bridging the gap between molecular-level bonding and macroscale fiber reinforcement in traditional fabrics or laminates (hierarchy level 4, ~ 1 m) (Figure 49).

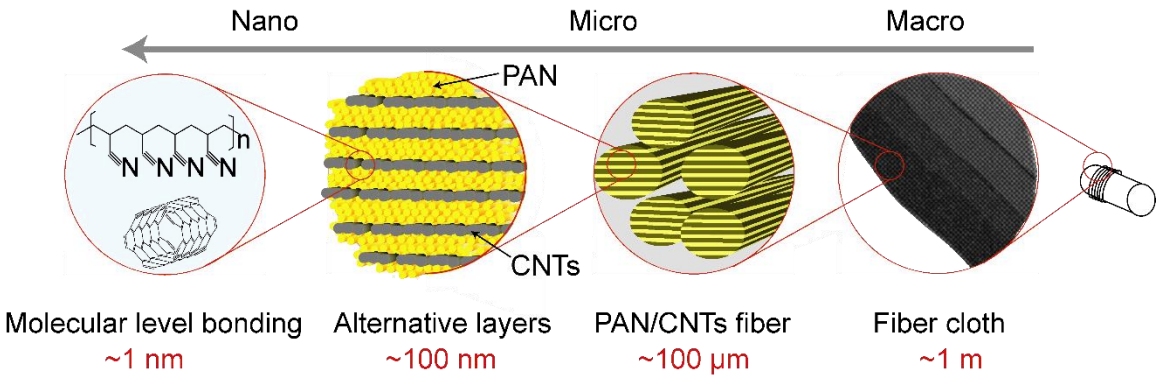

Figure 49. Schematic of the carbon fiber hierarchal structure from nano to macro scales.

5.2 Experimentation and Characterization

Materials: Polyacrylonitrile powder (230,000 g mol^{-1}, mean particle size 50 µm; copolymer, 99.5% acrylonitrile (AN)/0.5% methyl acrylate (MA)) was purchased from Goodfellow Corporation, USA. Industrial-grade, commercialized multi-wall CNTs (MWCNTs), NC7000, with an average diameter of 9.5 nm and length of 1.5µm, were purchased from Nanocyl, Belgium. DMF (anhydrous, ≥99.8%), methanol (HPLC, ≥99.9%), and silicone oil were purchased from Sigma Aldrich, USA.

Nanoparticle dispersion and preparation of spinning dope: For multilayer-structured spinning dope, 0.075 g of multi-walled CNTs in 50 ml DMF was first sonicated in a bath sonicator at room temperature for 8 hours. Then, 1 g of PAN powder was added to the MWCNTs dispersion and stirred for 2 hours at 80 °C. The solution was sonicated for 8 hours, followed by the addition of 6.5 g PAN powder. The resulting 50 ml DMF with 7.5 g PAN powder and 0.075 g of MWCNTs was stirred at 80 °C for 8 hours using a mechanical stir as the CNT/PAN layer solution. Next, 8 g PAN was dissolved in 50 ml of DMF and was stirred at 80 °C for 2 hours as the pure PAN solution. The final

CNT(1wt%)/PAN and PAN solutions were further deaerated for 1 hour at 80 °C under a vacuum. For the D-Phase fiber spinning dope, 0.0375 g of MWCNTs, was used in the nanoparticle dispersion process to maintain 0.5 wt% equal nanoparticle loading of the overall nanocomposite fiber while all other procedures were maintained the same. The density of CNTs and PAN was 2.2 g cm^{-3} and 1.184 g cm^{-3}, respectively, leading to a 0.27 vol% CNT concentration in all composite fibers.

Fiber spinning: The spinning dopes of PAN and PAN/CNT for the multilayer fibers were quickly transferred to two stainless-steel syringes, and the syringes were connected to the two inlets of the 3D printed multilayer spinneret (Concept Laser M2 Cusing, GE Additive). For the D-Phase fiber, the same PAN/CNT spinning dopes were connected to the two inlets of the spinneret. Next, all spinning dopes were injected at 2 ml min^{-1} speed into a coagulation bath of methanol at room temperature. The airgap was fixed at 4 cm and a constant take-up speed was set at 30 cm s^{-1}. The collected fiber was then immediately drawn and washed in water at 80 °C with a draw ratio of 5. The resulting fiber was collected and dried overnight in a vacuum oven at 50 °C. The dried fiber was then further drawn in silicone oil at 130 and 150 °C until reaching a maximum draw ratio.

Characterization: The optical images of the fiber cross-sections, cut using a microtome (Leica RM2235), were taken using transmitted light microscopy (MX50, Olympus). ImageJ was used for the analysis of particle distribution. Rheological behavior, fiber tensile test, and DMA were conducted using Discovery HR-2 (TA instrument). For viscosity tests, a 40 mm, 2° Peltier cone plate with a 100 μm gap at 25 °C was used. For the tensile tests, ten samples of each fiber type were tested with a gauge distance of 1 cm and a gauge speed

of 150 μm s^{-1}. For dynamic mechanical analysis, a bundle of 10 fibers was tested at 1 Hz frequency with a minimum force of 1 N. 0.25% pre-strain and a 0.2% oscillation strain were used with a temperature ramp of 3 °C min^{-1}. SEM was employed for microstructural morphology analysis using XL30 ESEM (Phillips). All samples were coated with 15 nm thick gold/palladium (Au/Pd) to increase conductivity. XRD was conducted using an Aeris X-ray diffractometer (Malvern Panalytical) from 5° to 70°. Raman spectrum and Raman mapping were obtained using confocal Raman-AFM microscopy with a 532 nm laser in the VV configuration (alpha300 RA, WITec). The sample was manually rotated every 10° from 0° to 90° for each polarized angle while the laser polarization configuration was kept fixed. For fiber diameter measurement, 5 sections with 60 cm in length were randomly selected from the collected fibers and weighted for calculating the fiber diameters. With the known relationship, $m=V\rho=\pi r^2 l\rho$, and the parameters of l (length), ρ (density), m (weighed mass), the diameter (r) can be calculated. Density was calculated based on a simple rule of mixture. The density of CNTs and PAN was 2.2 g cm^{-3} and 1.184 g cm^{-3}, respectively.

5.3 CNTs Dispersion Quality

The thin layer thickness during composite-making is critical as it selectively distributes fillers in each layer and achieves optimal dispersion quality and reinforcement effects (e.g., thin-ply structure in traditional laminates). An example of the 32-layered solution exiting the spinneret is shown in Figure 50a, with the transparent and black layers representing the PAN and CNT/PAN solutions, respectively. Through an air gap of 4 cm, the layered spinning solution goes through a methanol coagulation bath and forms the as-spun fiber,

with the cross-sectional area shown in Figure 50b. The alternating layers (i.e., compositions of PAN and CNT/PAN solutions) have similar viscosity properties, and viscosity matching is a crucial factor for forming uniform layers (Figure 50c$_1$).[60] The PAN and CNT/PAN solutions demonstrated the shear thinning behavior necessary for fiber spinning in the range between 1 to 10^3 s^{-1}.[44]

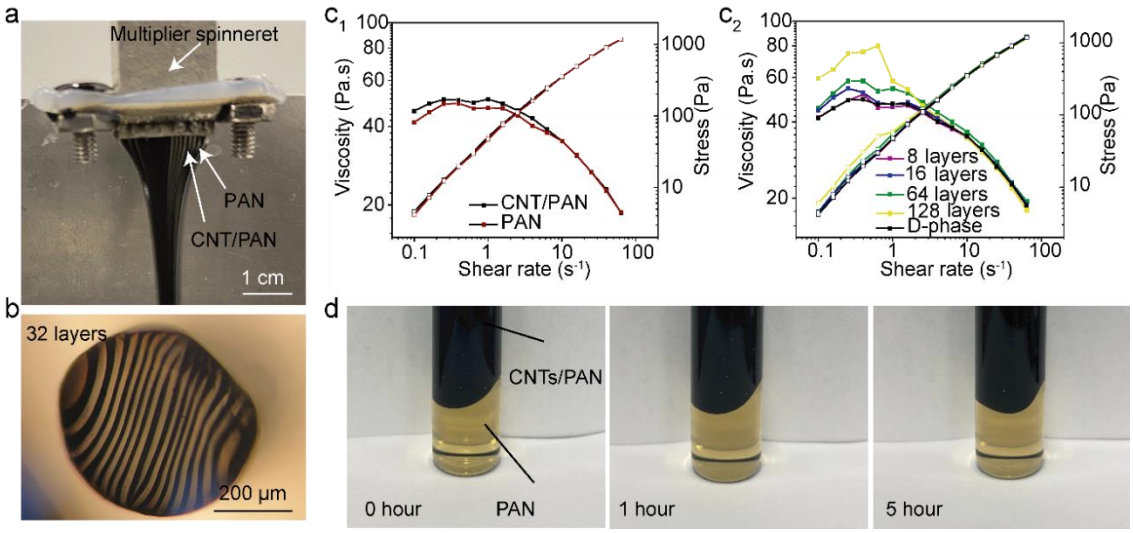

Figure 50. Multilayer structure characterization. (a) Photograph during 32-layer fiber spinning. (b) Cross-sectional optical image of a 32-layer fiber. Rheology behavior of (c$_1$) PAN and CNT/PAN, and (c$_2$) stacked PAN and CNT/PAN layers. (d) Stability test of CNT/PAN and PAN layered solutions.

Viscosity measurements of varied stacking layers of PAN and CNT/PAN solutions (e.g., 8, 16, 64, and 128 layers) and their mixture (e.g., D-Phase) were performed and fitted using the Carreau-Yasuda model according to Equation 5.1 (Table 5),[231]

$$\eta = \eta_\infty + (\eta_0 - \eta_\infty)[1 + (\lambda\dot{\gamma})^a]^{\frac{n-1}{a}} \quad (5.1)$$

where η_0 and η_∞ are the zero-rate viscosity and infinite-rate viscosity indices, respectively. $\dot{\gamma}$, λ, n, and a represent shear rate, consistency, rate index, and transition index, respectively. The zero-rate viscosities (η_o) showed an apparent increasing trend with increased layer numbers, from 46.43 Pa.s for 8 layers to 68.70 Pa.s for 128 layers, while the viscosities of the D-Phase solution were only 49.33 Pa.s (Figure 50c$_2$). As the total polymer and CNT concentrations were maintained the same, this viscosity increase is likely the result of the additional interfaces between adjacent PAN and CNT/PAN layers (Figure 50d). The interface may not be perfectly smooth, causing an increase in the mechanical resistance/friction accumulated at a shear rate below 0.5 s^{-1}. Nevertheless, at higher shear rates where the interfacial resistance was overcome, the viscosity differences diminished, and all samples demonstrated shear-thinning behavior. With an increased shear rate beyond 10 s^{-1}, the relatively high viscosity also prohibited the phase diffusion of the CNTs across layers, as depicted in Figure 50d, where a distinct interface was stable for over five hours.

Table 5. Fitted Carreau-Yasuda model (Equation 5.1) of different types of solution combinations.

Type	η_0 (Pa.S)	η_∞ (Pa.S)	λ (s)	n	a
PAN	44.65	-299	0.537	0.977	34.79
D-phase	49.33	-3213	0.5	0.997	4.28
8 layers	46.43	-130006	0.457	0.999	127.7
16 layers	49.59	-786.756	0.54	0.989	1.86
64 layers	53.25	-1545	0.688	0.994	8.75
128 layers	68.70	-26.68	1.59	0.835	139.879

An additional sample of dispersed CNTs in PAN (i.e., 0.5 wt% CNT/PAN) without any layer features, termed a D-Phase fiber, was also fabricated for comparison. All composite fibers were processed under the same sonication and mixing conditions prior to fiber spinning, as detailed in the experimental section. After being collected from the coagulation bath, these as-spun fibers were drawn at three different temperature stages in water and silicone oil to their maximum draw ratios before breakage (Table 6). The morphologies of 8-, 32-, 256-, 512-, 1024-layered, and D-Phase fibers as spun and collected are shown in Figure 51. The post-drawing fiber morphologies are shown in Figure 52a, with images taken on 800 nm-thick cross-sections prepared via a microtome. The layer morphology was not distinct for the 1024-layered fiber and could be mainly due to the multipliers' dimensional design and 3D printing resolution. Layering path length and

restacking transition smoothness could both lead to disturbances to the polymer flow and CNT conformations.[60]

Table 6. Draw ratios of all types of fibers.

Fiber type	Draw ratio at 80°C	Draw ratio at 130 °C	Draw ratio at 150 °C	Total draw ratio
8 layers	5.6	2.3	1.9	24.4
16 layers	4.9	2.0	2.2	21.0
32 layers	5.2	2.1	2.1	22.4
64 layers	5.1	2.0	2.1	20.5
128 layers	5.0	1.9	2.2	21.2
256 layers	5.6	1.8	2.6	26.6
512 layers	5.8	2.0	2.2	25.0
1024 layers	5.4	2.4	2.1	27.1
2048 layers	5.3	2.8	2.0	28.3
D-Phase	5.3	2.2	2.3	26.0

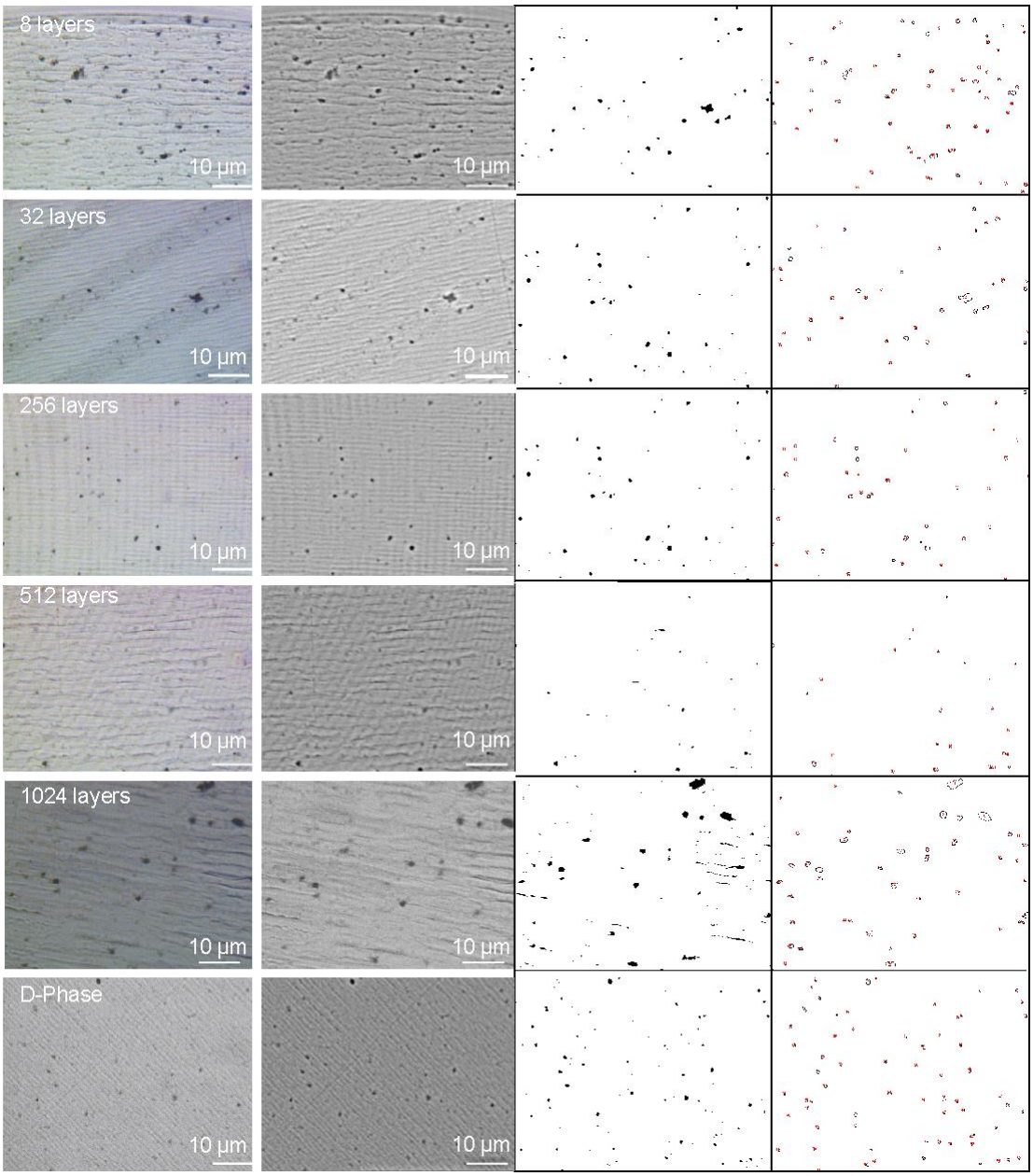

Figure 51. Optical images for the as-spun fibers of 8-, 32-, 256-, 512-, 1024-layered, and D-Phase fibers. Images were processed using ImageJ. From left to right: original image, 8-bit black and white format, applied intensity threshold, applied minimum size (0.2 μm^2),

and roundness (0.5). The coordinate of each spot was then used to calculate their nearest neighbor using MATLAB.

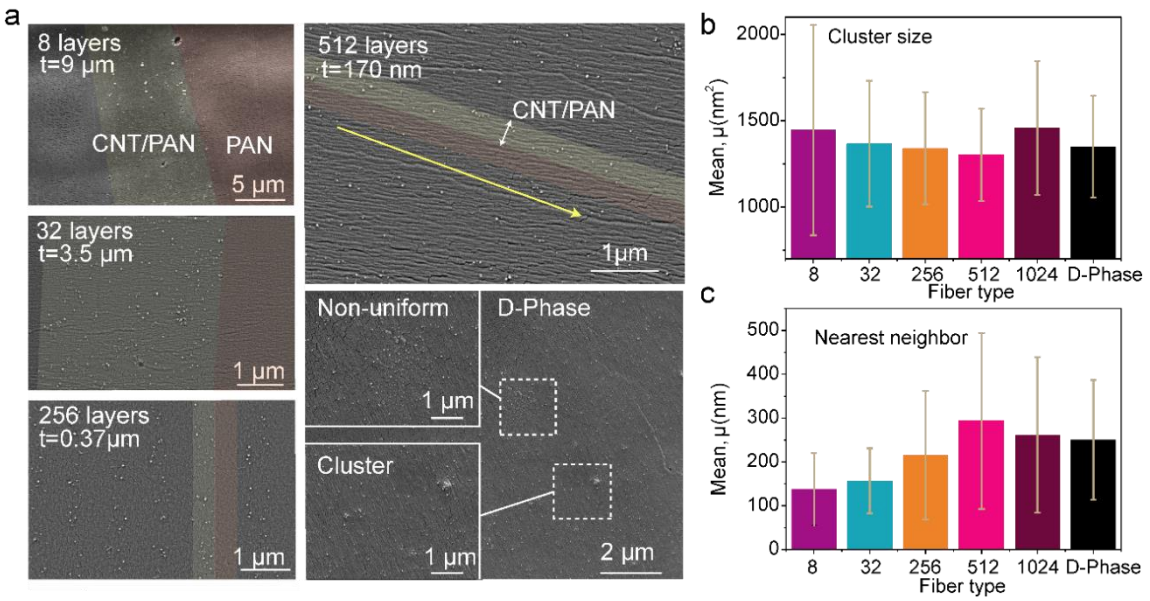

Figure 52. (a) SEM images of the post-drawn 8-, 32-, 256-, 512-, and D-Phase fibers where yellow- and red-colored regions represent CNT/PAN and PAN layers, respectively. The mean and standard deviation values of the clusters of post-drawn fibers in terms of (b) cluster size and (c) the nearest neighbor distance.

The nanoparticle dispersion quality was analyzed using software ImageJ for both cluster size and the first nearest neighbors. For the as-spun fibers, the largest CNT aggregate sizes of the 8-, 32-, 256-, 512-, and 1024-layered fibers were 6.9 μm^2, 5.6 μm^2, 5.1 μm^2, 4.2 μm^2, and 6.9 μm^2, respectively, showing a monotonic decrease with increasing layer number up to 512 layers (Figure 53a). In addition, D-Phase fiber showed its largest aggregate of 5.1 μm^2, which was larger than that of the 512-layered fibers. The first nearest neighbor distance was used to analyze the distribution homogeneity of the CNTs, where larger mean

and standard deviation values indicate better dispersion quality. 512-layered fiber showed the highest mean, 4.54 μm, and standard deviation, 2.97 μm, where D-Phase fiber showed a mean of 2.96 μm and a standard deviation of 1.55 μm, representing a worse dispersion uniformity (Figure 53b).

After drawing the fibers above their polymer T_g, the PAN polymer chains began to uncoil, reducing the fiber diameter to approximately 80 μm. Light yellow and red colors were applied to the CNT/PAN and PAN layers, respectively, for enhanced contrast (Figure 52a). All fibers maintained their as-spun multilayer structure with much smaller layer thicknesses, down to approximately 170 nm for the 512-layered fiber. The same trend in dispersion quality was observed between the post-drawn fibers and the as-spun fibers, where 512-layered fiber showed the smallest cluster size and best dispersion quality in terms of its largest first nearest neighbor distances (Figures 52b and c). On the contrary, SEM images of the D-Phase showed inferior dispersion quality (Figure 52a), where the upper zoomed-in image exposed non-uniform dispersion and the lower zoomed-in image exhibited different cluster sizes.

This decrease in the aggregate size during the fiber spinning process was due to polymer chain reorganization, with the nanotube aggregates physically confined within each layer. Under the same experimental conditions (e.g., tip sonication and mechanical stirring), CNTs were expected to have the same dispersion quality before spinning. During fiber spinning, as the layer thickness gradually decreased beyond a point when the layer width was less than the initial CNTs cluster size, the shear force generated between two adjacent PAN and PAN/CNT layers would start exfoliating the clusters and render their sizes lower

than the corresponding layer thickness. Both aggregate size distributions and the first nearest neighbor distance values proved that the decreased layer thickness positively influenced the nanoparticle dispersion and exfoliation quality as layer number increased.

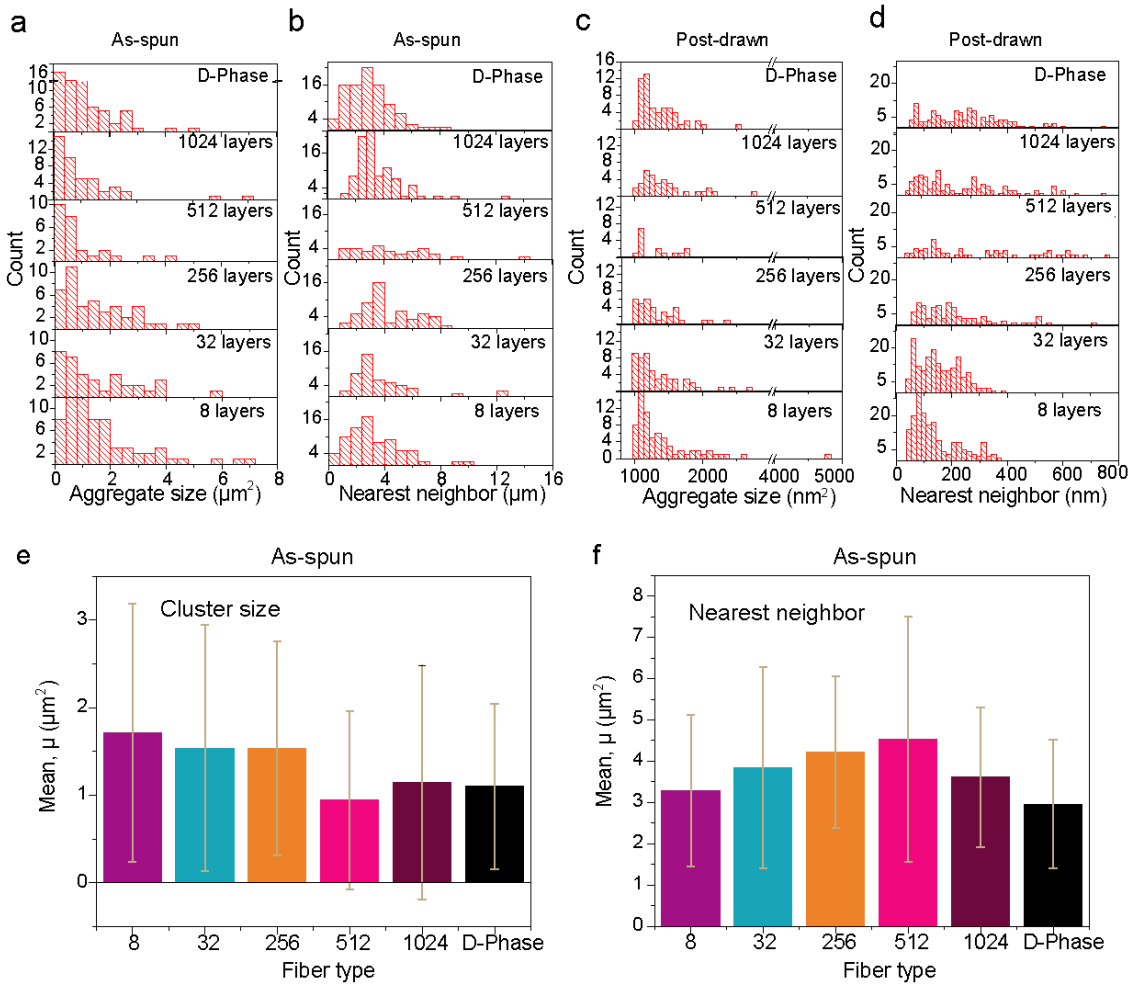

Figure 53. Nanoparticle cluster and dispersion study. (a) CNT cluster distribution of the as-spun fiber. (b) First nearest neighbor distribution of the as-spun fiber. (c) CNT cluster distribution of the post-drawn fiber. (d) First nearest neighbor distribution of the post-drawn fiber. (e) The mean and standard deviations of (a). (f) The mean and standard deviations of (b).

5.4 Mechanical Reinforcement

After microtoming the fibers embedded in epoxy resins, the cross-sectional areas of the drawn fibers were carefully measured through SEM images and the weighing method (Figure 54). There are small standard deviations for the weight from five different sections sampled from each fiber type, suggesting high fabrication precision of the fiber spinning process and size consistency (Figures 54 and 55). For example, 1 wt% CNTs in each CNT/PAN channel was used as feedstock, resulting in 0.5 wt% CNTs loading in the overall fiber (i.e., considering one channel was CNT/PAN and the other channel was PAN and these formed alternating layers) for all layered composites. For consistency, the CNT loading of the D-Phase fiber was controlled at 0.5 wt% with a single-phase morphology across the fiber. The volumetric concentrations of CNTs in all fibers were calculated at 0.27 vol%.

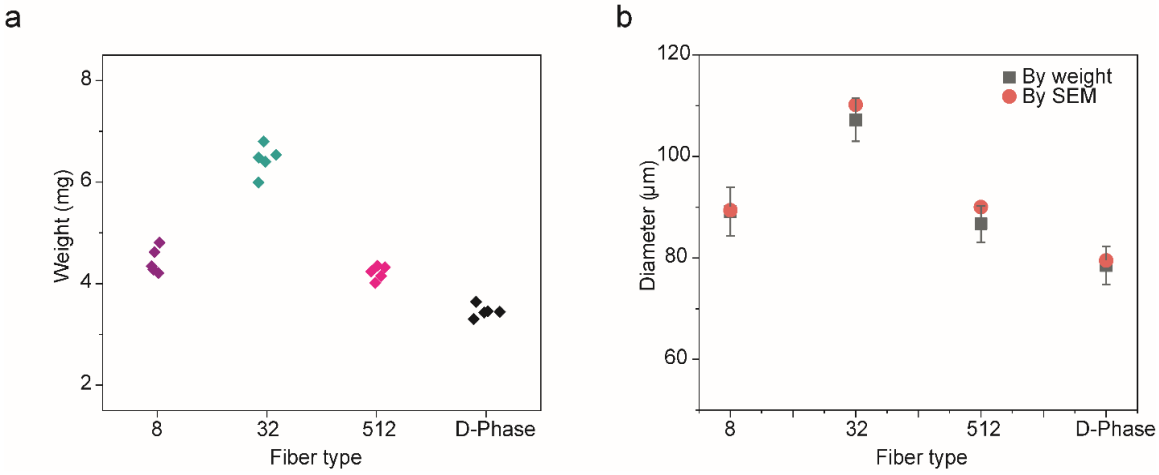

Figure 54. Consistency of the fiber dimension during fabrication. (a) Distribution of collected fiber segments for four selected fiber types. (b) Calculated fiber diameters with standard deviation compared with measured diameters from SEM images.

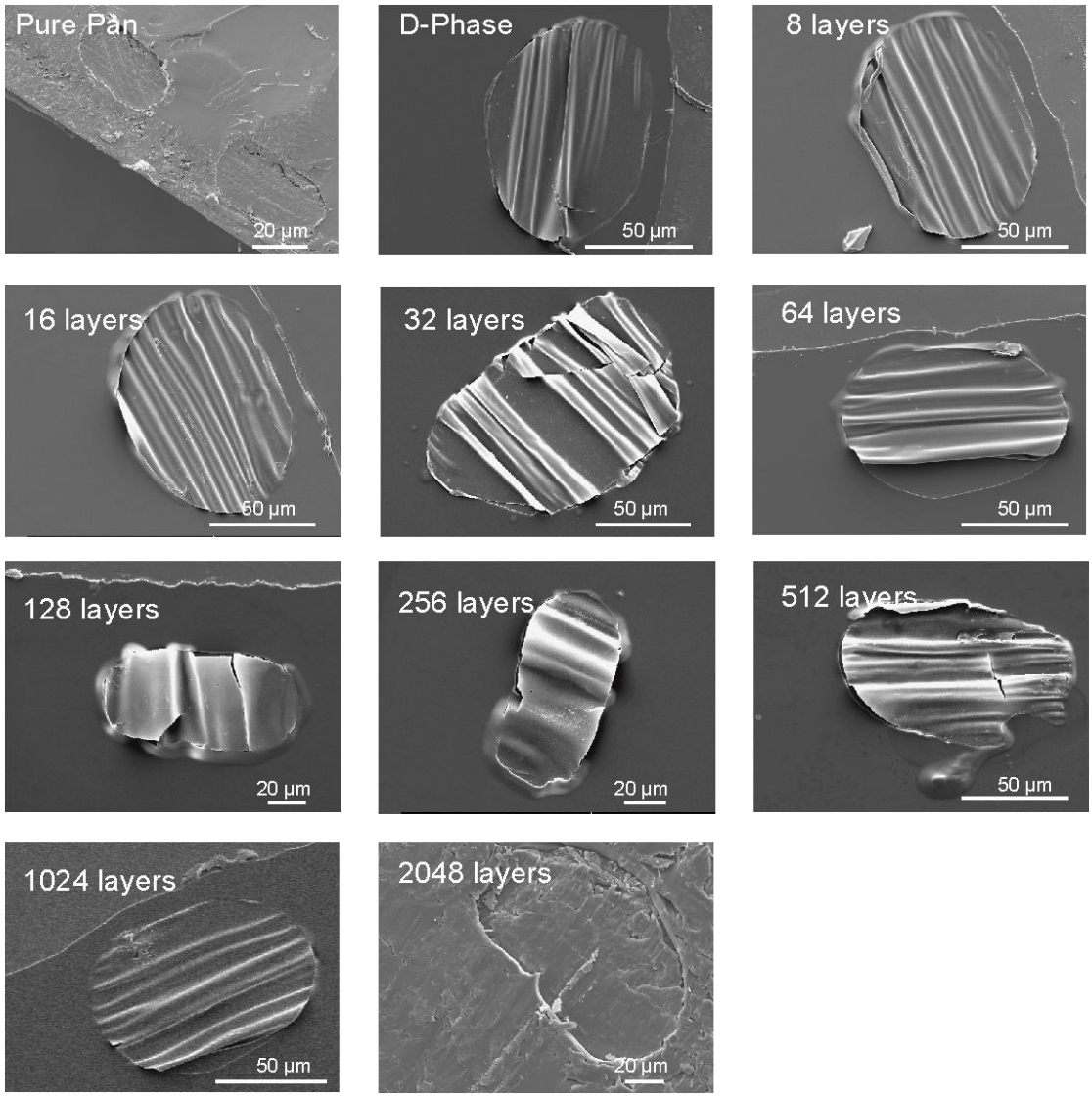

Figure 55. Microtomed cross-sectional SEM images of all fiber types

The stress-strain curves of different fiber morphologies are shown in Figure 56a, and detailed mechanical data are listed in Table 7. With similar ultimate strain values to the pure PAN, D-Phase fiber increased 12.3% and 12.9% in both ultimate tensile strength and Young's modulus, respectively. This enhancement has been observed in many polymer composites, mainly due to the polymer chains' load transfer to the more mechanically

robust CNTs.[11,232] Interestingly, the mechanical properties showed a strong dependence on layer thicknesses for the multilayered fibers. The 16-, 32-, and 64-layered fibers slightly increased from 8-layers. Starting from the 128-layered fiber, Young's modulus and ultimate tensile strength enhancements were observed and peaked at 512 layers (i.e., 170 nm layer thickness) with 19.3 GPa and 689 MPa for modulus and strength, respectively. By constructing the fiber with alternating layers containing PAN and PAN/CNT at the nanometer scale, 512-layered fiber showed a 46.4% increase in modulus and a 39.5% increase in strength from the pure PAN fiber. These mechanics increases were a 27.4% improvement in modulus and a 22.2% in strength compared to the D-Phase fiber.

Improving both material strength and toughness at the same time has always been a challenge.[233] PAN-based fiber showed an average toughness and strength of 26.67 MJ m^{-3} and 494.41 MPa, respectively. With increasing layer numbers and decreasing layer thicknesses, 512-layered fiber showed a 39.5% increase in strength and 36.4% increase in toughness (i.e., 689.54 MPa for strength and 36.37 MJ m^{-3} for toughness) than the pure PAN fiber (Figure 56c and Table 7). The fracture section SEM images showed that the fiber pull-out morphology was the most obvious for the 512-layered fiber (Figure 56d), whereas a smoother fracture surface was seen for the D-Phase fiber and the 8-layered fiber (Figures 56e and f). The fracture section SEM images of the 1024-layered fiber showed unpredicted voids and cracks, suggesting possible loss of the layer features, which ultimately led to their inferior mechanical properties (Figure 56g). The fiber pull-out morphology coincided with the increase of toughness, suggesting extra energy was consumed to cause fracture since more energy was dissipated at the CNT to polymer

interface and subsequent fibrillar formations.[35] On the other hand, limited dispersion quality also increased CNT-to-CNT contact, diminishing their load transfer efficiency with the polymer matrix.[234]

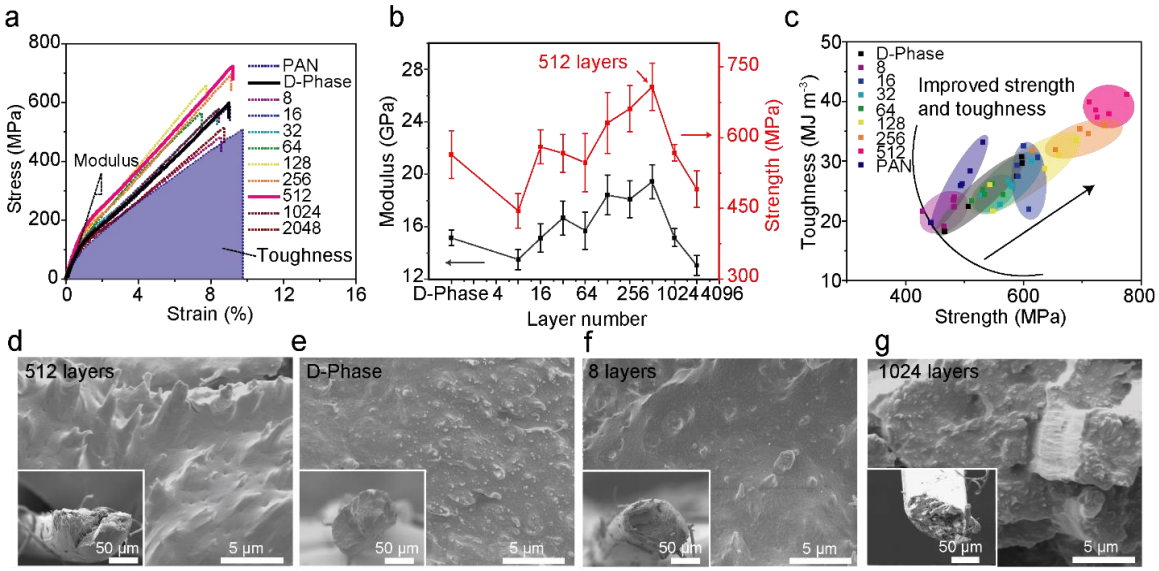

Figure 56. The mechanical properties of different fiber types. (a) The stress-strain curves of all the multilayered fibers plus pure PAN and D-Phase fibers. (b) The Young's modulus and ultimate tensile strength of different fibers. (c) Enhancement of ultimate strength and toughness with increasing layer numbers. The fracture SEM images of (d) 512-layered, (e) D-Phase, (f) 8-layered, (g) and 1024-layered fibers at room temperature.

Table 7. Mechanical data of all fibers and their associated diameters and calculated layer thicknesses.

Type	Modulus (GPa)	Strength (MPa)	Strain (%)	Toughness (MPa)	Diameter (um)	Calculated layer thickness (um)
Pure PAN	13.19±0.85	494.41±32.37	9.15±0.95	26.67±4.35	72.1	
D-phase	15.15±0.59	564.13±50.55	8.36±0.55	27.58±3.70	79.5	
8	13.50±0.78	444.95±36.12	7.87±0.79	20.19±3.08	89.4	11.18
16	15.14±1.08	580.57±36.45	8.57±0.72	26.98±3.78	85.12	5.32
32	16.66±1.30	566.82±30.89	7.93±0.67	25.49±3.38	110.2	3.44
64	15.71±1.40	546.91±61.28	7.95±0.64	25.49±5.02	87.0	1.36
128	18.42±1.50	630.87±64.70	7.69±0.44	27.31±4.22	87.0	0.68
256	18.11±1.40	661.57±48.80	8.62±0.80	31.30±4.39	87.0	0.34
512	19.31±1.28	689.54±48.42	9.08±0.61	36.37±3.69	90.02	0.17
1024	15.17±0.69	568.36±17.51	8.33±0.48	26.46±1.98	88.7	0.087 (not observed)
2048	13.05±0.77	491.03±38.87	8.04±0.68	20.57±3.72	90.92	0.044 (not observed)

Figure 57 depicts the structural differences between the D-Phase, 8-layered, 32-layered, and 512-layered fibers before and after drawing, and it illustrates the mechanism behind

the enhanced mechanical properties. In addition, the CNT aggregation study has shown the positive effect of thinner layer thickness on the CNTs' dispersion quality. Thus, XRD, DSC, DMA, and polarized Raman spectroscopy were used to show the improved polymer crystallinity and CNT alignment by including the hierarchical multilayered structure.

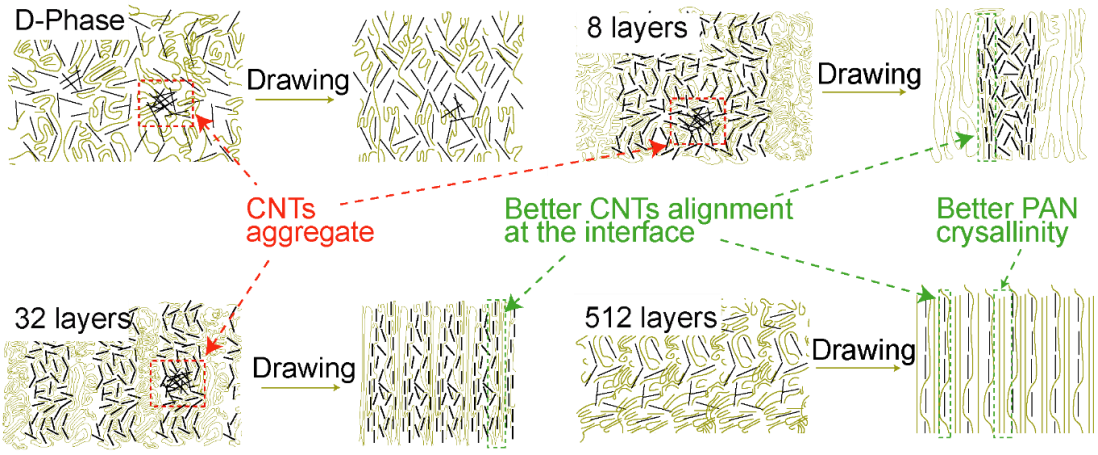

Figure 57. The schematic shows different fiber morphologies of PAN polymer chains and CNTs before and after drawing.

5.5 Polymer Crystallinity Dependency on Layer Morphology

The addition of nanoparticles in polymer composites sometimes disrupts the long-range order of polymer chains and depresses their crystallization behaviors.[235] XRD analysis was conducted on industrial-grade CNTs, background, and all fiber types, and their associated crystallinities and crystallite sizes were calculated based on the fitted curves shown in Figure 58. The CNTs' diffraction peak (002) at 2θ ~26.7° was not observed for all fiber types, indicating molecular level dispersion of the CNTs. The crystalline peaks were fitted at 2θ ~17° and 30°, representing the (200)/(110) and (310)/(020) plans, respectively, and the peak at an approximate 2θ ~22° came from the amorphous peak.

These peaks identified were consistent with previous research.[236] The crystallinity and crystallite size of the 2θ ~17° peak did not vary much from 8 to 64 layers but increased from 128 layers. Both values peaked at 512 layers with 70.6% and 9.46 nm, respectively, showing a trend of increasing crystallinity and crystallite size with decreasing layer thickness (Figure 59). In the D-Phase fiber, when the CNTs penetrated between the polymer chains, they limited the draw ratio and deteriorated the crystallinity of the overall fiber, resulting in only 63.3% crystallinity and a smaller crystallite size of 8.72 nm. The 2θ ~17° peak positions also shifted to a higher 2θ position from 8-layered to 512-layered fibers, resulting in a lowered *d*-spacing. This indicates that a decrease in layer thickness would cause a higher packing factor of the PAN molecules. The *d*-spacing increased to 0.5108 nm for the D-Phase fiber and 0.5222 nm for the pure PAN fiber, indicating a less packed molecule structure (Figure 59) and are highly consistent with previous literature reports.[236] The high crystallinity could be due to the confinement of the PAN polymer chains, which were sandwiched between two adjacent CNT-containing layers. As thickness gradually decreased to the nanoscale level, the polymer chains were more constrained to grow in the lateral direction than the axial direction, resulting in confinement of the polymer chains similar to polymer/polymer confinement found in previous multilayer composites with nanoscale layer thicknesses.[170,237]

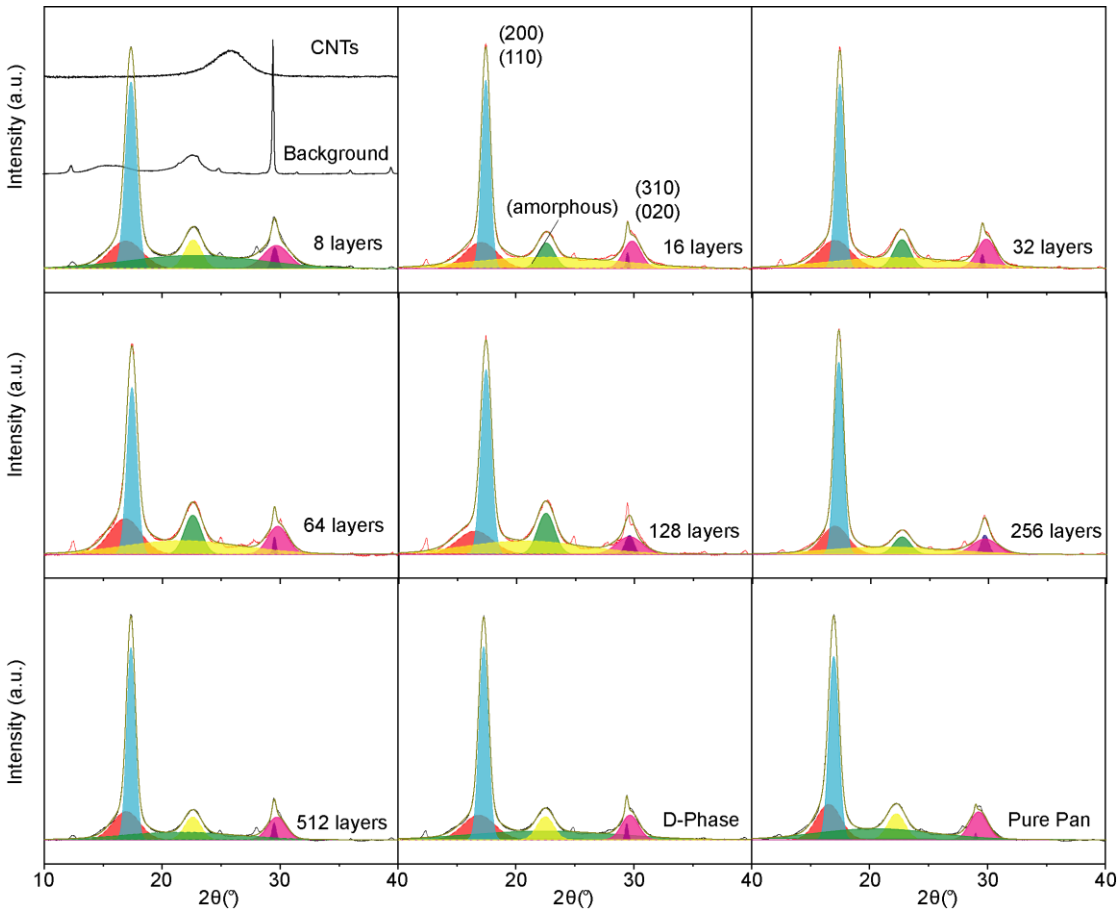

Figure 58. XRD measurements of different fiber types.

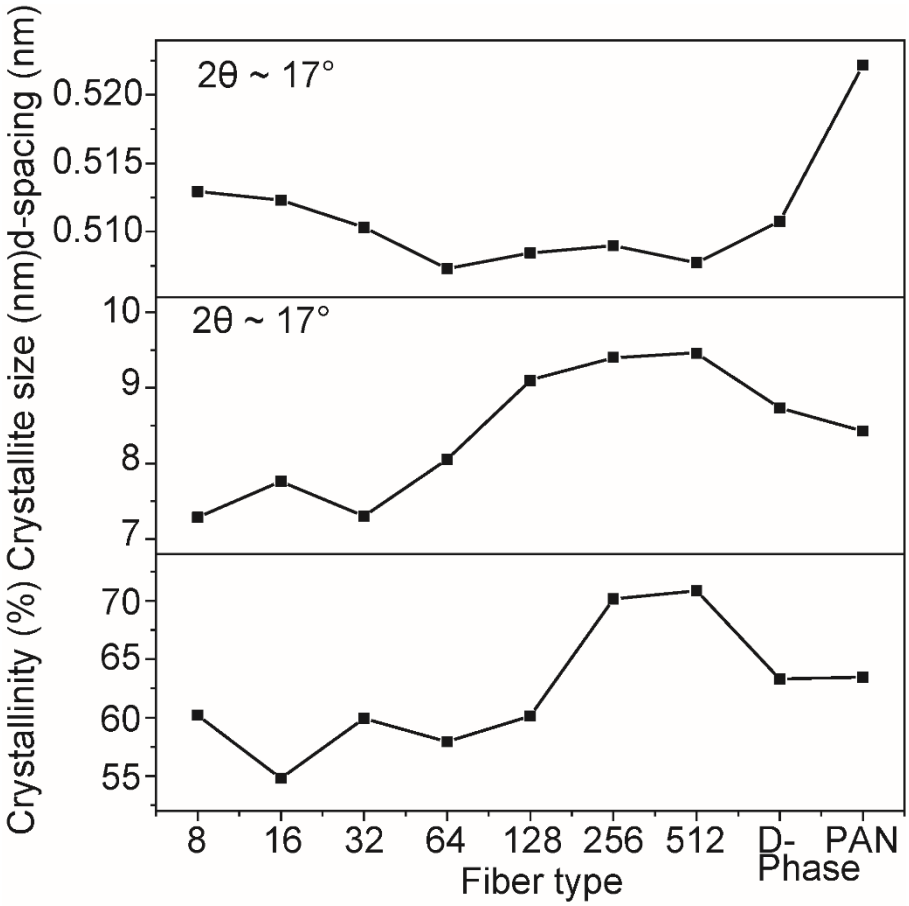

Figure 59. The *d*-spacings (2θ ~17° peak), crystallite sizes (2θ ~17° peak), and crystallinities for all fiber types.

PAN polymer in nitrogen undergoes a cyclization of the nitrile group process at elevated temperature (e.g., treatment of stabilization and carbonization), which is crucial for making PAN-based carbon fibers.[238] An increase in activation energy during this treatment leads to more stabilized and high-performance carbon networking.[239] For the composite fibers, there was a monoclinic increase in activation energy values with higher layer numbers (Figure 60 and Table 8). Among them, the 512-layered fibers showed the highest exothermal peak temperatures (i.e., 273.27, 285.74, 297.45, 309.79, and 318.38 ^{o}C) for the

cyclization process conducted at all different heating rates, shown in Table 9. The higher temperature requirement indicates that the 512 layers had the most reduced polymer chain mobility of the polymer chains during the cyclization reaction.[240] This was due to the enhanced nanoparticle dispersion and confinement in global and local regions. Kissinger Equation (Equation 5.2) was used to calculate the activation energy,

$$-\frac{E_a}{R} = \frac{d[ln\left(\frac{\varphi}{T^2}\right)]}{d(\frac{1}{T})} \tag{5.2}$$

where E_a is the activation energy (kJ mol^{-1}), φ is the heating rate (°C min^{-1}), R is the molar gas constant, and T is the peak temperature (Kelvin), which is obtained from DCS curves. A slight increase was found regarding kinetics between 512- 1024 layered fibers, among other types of fibers.

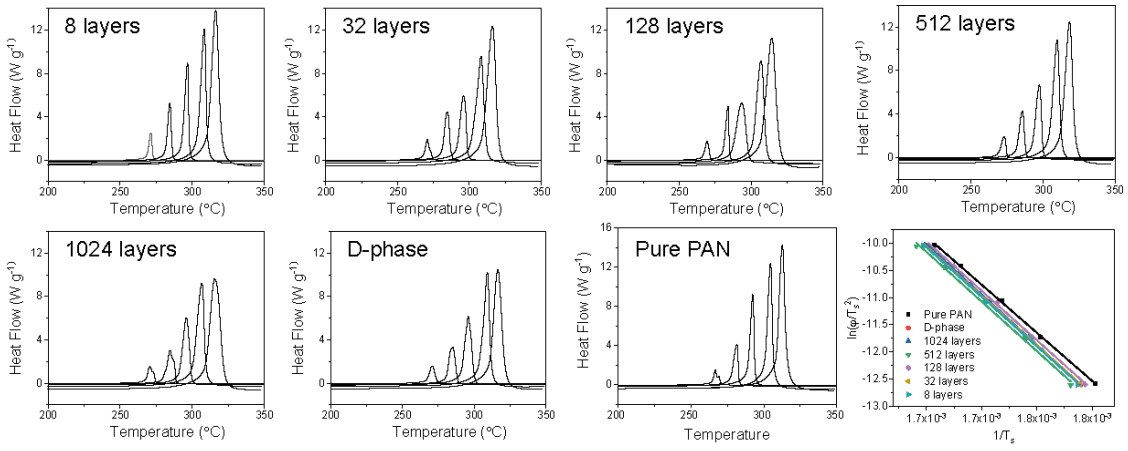

Figure 60. DSC of all fibers for different heating rates simulating the stabilization process with calculated activation energy.

Table 8. The activation energy calculated for the cyclization process using the Kissinger Equation

Fiber type	E_a [KJ mol^{-1}]
Pure PAN	146.53
D-phase	151.24
1024	153.09
512	151.30
128	150.71
32	150.28
8	150.80

Table 9. DSC peak temperatures of all fibers for different heating rates

Fiber Type	Peak temperature (°C)				
	1 (°C min^{-1})	2.5(°C min^{-1})	5 (°C min^{-1})	10 (°C min^{-1})	15 (°C min^{-1})
8	271.4	284.55	296.78	308.41	316.35
32	270.81	284.63	296.01	308.13	316.05
128	269.43	283.9	293.51	306.88	314.42
512	*273.27*	*285.74*	*297.45*	*309.79*	*318.38*
1024	270.75	284.75	296.03	306.77	315.68
D-phase	270.82	285.18	295.86	309.13	316.42
Pure PAN	266.68	281.57	292.43	304.63	312.71

5.6 Layer-layer Interactions

DMA was also conducted to further demonstrate the multilayered structure's effect on the overall mechanical behaviors. All fibers eventually fractured while maintaining a constant axial force of 1 N during temperature sweeping, as shown in the storage modulus results (Figure 61a). The 512-layered fiber had the highest failure temperature among all fibers, indicating the best thermal resilience and mechanical robustness (Figure 62b). Figure 61b shows the change of the composite damping factor (i.e., tan $(\delta)_c$), defined as the ratio between loss modulus and storage modulus at a specific temperature. The initial tan $(\delta)_c$ values at room temperature show a decreasing trend with increasing layer numbers, and 512-layered fibers showed the lowest value, indicating the highest elasticity (Figure 62b). The high elasticity is mainly due to limited polymer chain mobility, consistent with the above-mentioned DSC data (Table 9). On the other hand, pure PAN fiber had the highest tan $(\delta)_c$ value at room temperature, suggesting less constrained polymer chains. However, as temperature increased beyond the fiber's glass transition temperature (T_g, ~ 70 °C), tan $(\delta)_c$ changed, as pure PAN fiber had the lowest value and 512-layered fiber showed a dramatic increase. To understand this, tan $(\delta)_c$ was dissected into tan (δ) of the system (i.e., tan $(\delta)_s$) and tan (δ) of the interface (i.e., tan $(\delta)_{in}$) according to the following Equations 5.3 & 5.4.[241]

$$\tan(\delta)_c = \tan(\delta)_s + \tan(\delta)_{in} \tag{5.3}$$

$$\tan(\delta)_s = \frac{\tan\delta_f E_f' V_f}{E_c'} + \frac{\tan\delta_m E_m' V_m}{E_c'} \tag{5.4}$$

Here, $E_f', V_f, E_c',\ E_m', and\ V_m$ stand for the storage modulus and volume fraction of the nanoparticle, storage modulus of the composite, and storage modulus and volume fraction of the polymer matrix, respectively.

The tan $(\delta)_s$ is a value affected by both the polymer matrix and the loaded nanotubes. However, since CNTs can be considered a perfectly elastic material, their energy absorption could be zero, resulting in the total system damping, tan (δ)s, solely depending on the second term in Equation 5.4. Figure 61c shows the composite fibers' calculated *tan (δ)s*. The damping factor was much lower for the 512-layered fiber across the temperature range, indicating less energy absorption by the polymer chains due to their higher elasticity. On the other hand, *tan* $(\delta)_{in}$ is the highest for the 512 layered fiber, indicating much higher energy dissipation at the interface between the CNTs and the polymer chains (Figure 61d). Conventionally, there could be two main reasons for the increase in interface energy dissipation: (1) weaker interfacial interactions between the nanoparticles and the polymer chains and (2) an increase in the nanoparticle concentration resulting in an increased energy dissipation site.[241,242] However, since the CNTs in different samples were used as received and were dispersed and sonicated under the same condition, their surface morphology and aspect ratio were identical, leading to similar interfacial interactions between each CNT and PAN polymer chain. Also, CNTs' concentration was maintained at 0.5wt% across different samples, leading to no variation in the overall fiber composition. One possible explanation for the increase of tan $(\delta)_{in}$ could be the high interfacial areas between PAN/CNT and PAN layers. With a temperature increase beyond T_g, differences in the viscoelasticity behavior between the PAN and CNT/PAN would cause different polymer

chain elongation, resulting in shear stress generated at each layer interface.[199,243] This can be observed in the SEM images of the fractured surfaces of the different fiber types (Figures 63a$_{1\text{-}5}$). The fibrous sizes of each sample reflected the individual layer design and were highly consistent with the layer thickness, e.g., from tens of μm for 8 layers to about 200 nm for 512 layers (Figure 63b). The separation of these fibers at high temperatures indicated a thermal stability mismatch, causing the interfacial interactions between different layers to further contribute to the increased tan $(\delta)_{in}$.

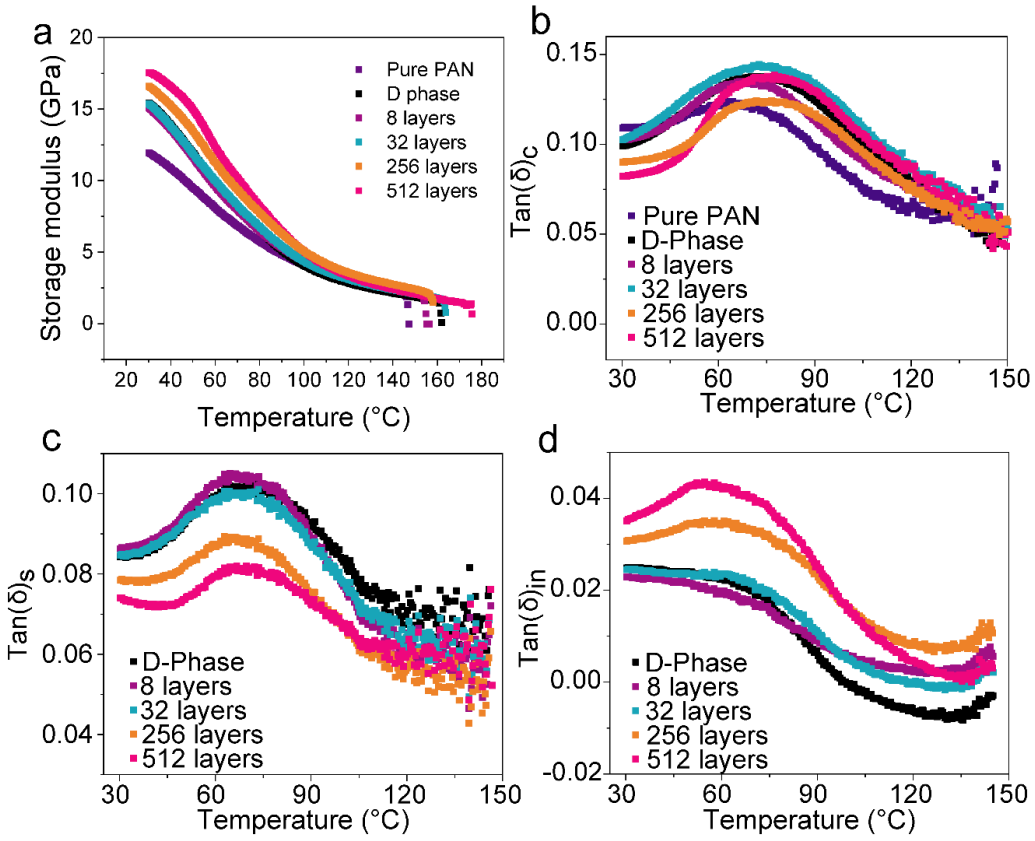

Figure 61. DMA of the multilayered fibers. (a) Storage modulus, (b) *Tan (δ)*, (c) *Tan (δ)*$_S$, and (d) *Tan (δ)*$_{in}$ of different types of fiber structures.

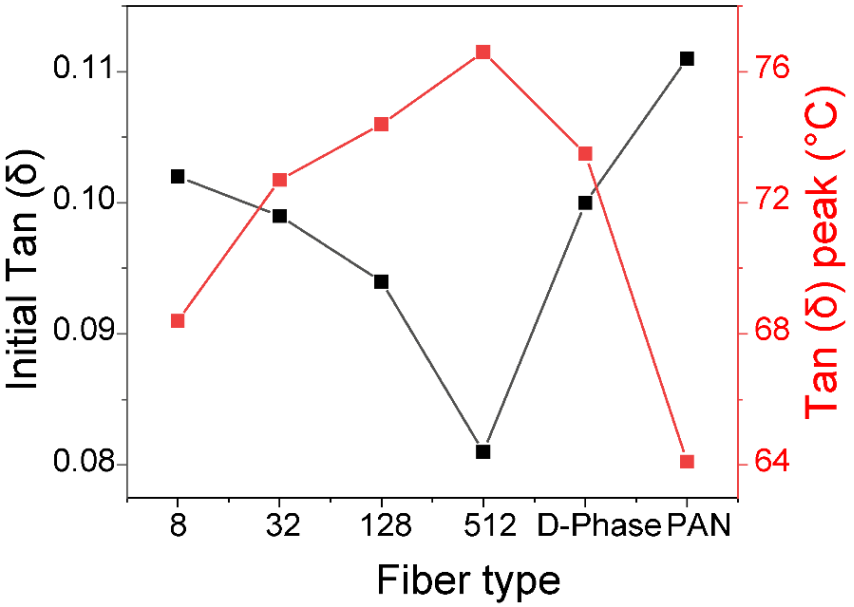

Figure 62. Initial Tan $(\delta)_c$ values at room temperature for various fibers and their peak temperatures.

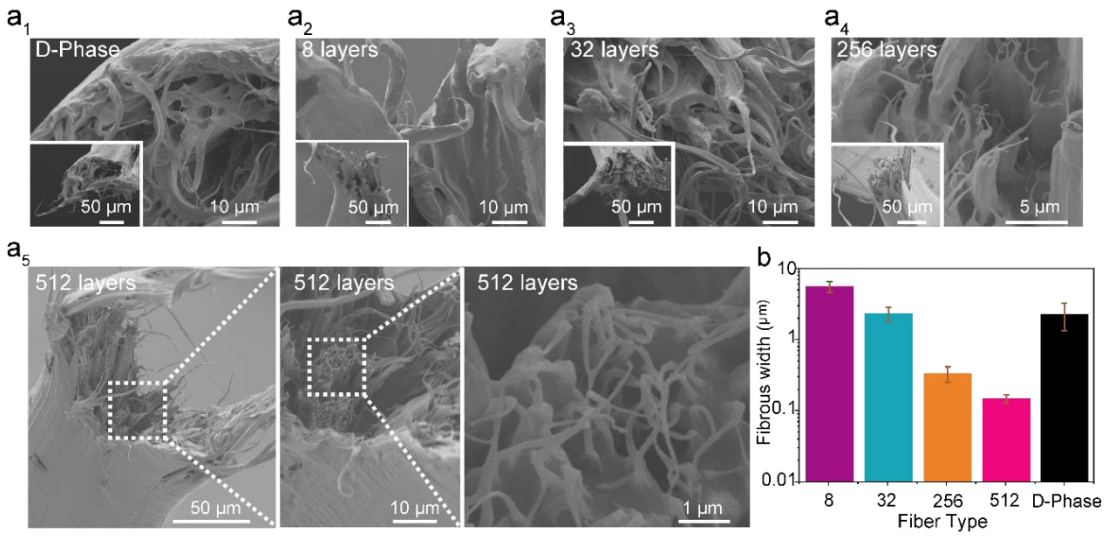

Figure 63. ($a_{1\text{-}5}$) SEM images of the fibers' cross-section after DMA with temperature sweeping. (b) The measured size of the fractured fibrils for selected fibers.

5.7 Shear stress-induced nanoparticle orientation

Based on the DMA analysis, it is expected that a similar interfacial shear force was generated during the fiber drawing process, causing different CNT orientations for different layer thicknesses. A polarized Raman spectroscopy was conducted to understand the CNTs' preferential alignment.[95,168] Considering the Raman mapping's resolution limit, only composite fibers with 8 layers were used to demonstrate the CNT conformation. For the Raman polarization, two different incident angles (ϕ=90^o, perpendicular to the fiber/layer axis, and ϕ=0^o , parallel to the fiber/layer axis) were used to analyze the nanotube orders (Figures 64a$_1$ and 64a$_2$, respectively). In the schematic in Figure 64a$_1$, the green arrow represents the polarized incident light direction while the black arrow represents the fiber axial direction (ϕ=90^o). When the laser beam was aligned perpendicular to the fiber/layer direction, there would be a minimum 'VV' configuration due to the polarization effect (intensity of I_{90^o} in Figure 64a$_1$). With the decrease of the laser beam-fiber layer misalignment angles, the 'VV' Raman intensity would be enhanced with the maximized peaks appearing in the parallel-to-fiber polarization directions (ϕ=0^o shown in the inserted schematic and intensity of I_{0^o} in Figure 64b$_1$). This Raman intensity *vs.* incidence angle relationship reported here is consistent with many studies regarding CNT or graphene orientations.[244,245]

Note that the spectra peaks in Figure 64a$_1$ (i.e., the red, green, and blue lines) correspond to the signals in Figure 64a$_2$ (i.e., the red, green, and blue regions). In the Raman analysis of the CNTs, the G band around 1600 cm^{-1} resulted from the E_{2g} vibration mode, and the D band around 1350 cm^{-1} was assigned to the A_{1g} symmetry, which was associated to the

defects (Figure 64a_1). Based on the signature peaks, both red and green spectra showed the D band at 1350 cm^{-1} representing the CNT/PAN layer, while the blue region represented the PAN layer (Figures 64a_2 and 64b_2). Interestingly, for CNT/PAN layers, the signals in the middle of the layer (colored red) showed higher average intensity than the signals in the edge of the layer (colored green) ($I_{90}°$ in Figure 64a_2). However, when the incident laser rotated to the direction parallel to the fiber axis, the intensity mapping of $I_0°$ showed the opposite trend; namely, the signals in the edge of the CNT/PAN layer had higher intensities than the middle of the layer (Figures 64b_1 and 64b_2). The higher depolarization effect observed at the edge of the layer indicated a better CNT alignment along the fiber axial direction. This more aligned orientation of CNTs was caused by the shear stress generated during the fiber drawing at the interfaces due to the composition and mechanics mismatch between neighboring layers. In addition, higher layer numbers led to more contacting interfacial areas, and upon stretching or drawing, this would result in more aligned CNTs. To further demonstrate the difference in CNT alignment between the 512-layered and D-Phase fibers, both samples were ϕ-rotated in the same VV configuration at random positions across the fiber surface (Figure 64c, with ϕ from 0^o to 90^o with a 10^o stepwise increase). Figure 64c shows the angular dependence of the Raman intensities for both 512-layered and D-Phase fibers, with both composites showing the maxima in D- and G-band signals at $\phi = 0°$, and their minima at $\phi = 90°$. Notably, the $I_0°/I_{90}°$ ratios are 3.57 and 2.56 for 512-layered and D-Phase fibers, respectively, where the higher ratio value for the 512 layers indicated a higher degree of CNT ordering along the axial direction (Figure 65).[52] To ensure that the Raman intensity was not affected by local CNT variations, three Raman

measurements were recorded for each angle. The normalized D-band intensities were averaged and plotted as a function of the corresponding polarization angles (Figure 64d). A fitting according to a Lorentzian form [246] shows that the composite fibers with 512 layers possess a half-width at half-maximum (HWHM) of 55.6°, while the D-Phase fiber has an HWHM of 66.5° (Figure 64d). As the distribution center was at ϕ=0°, a smaller HWHM of the 512-layered fiber indicates a better CNT orientation than the D-Phase fiber. Similar angular dependency was also found for the normalized G-band, where the 512-layered fiber showed a smaller HWHM. The average length of the CNTs was approximately 500 nm after six hours of sonication, which was three times larger than the layer thickness of 170 nm of the 512 layers, therefore facilitating the CNT alignment along the fiber axis. These enhanced CNTs orientations correspond to the improved mechanics, as shown in Figure 56.

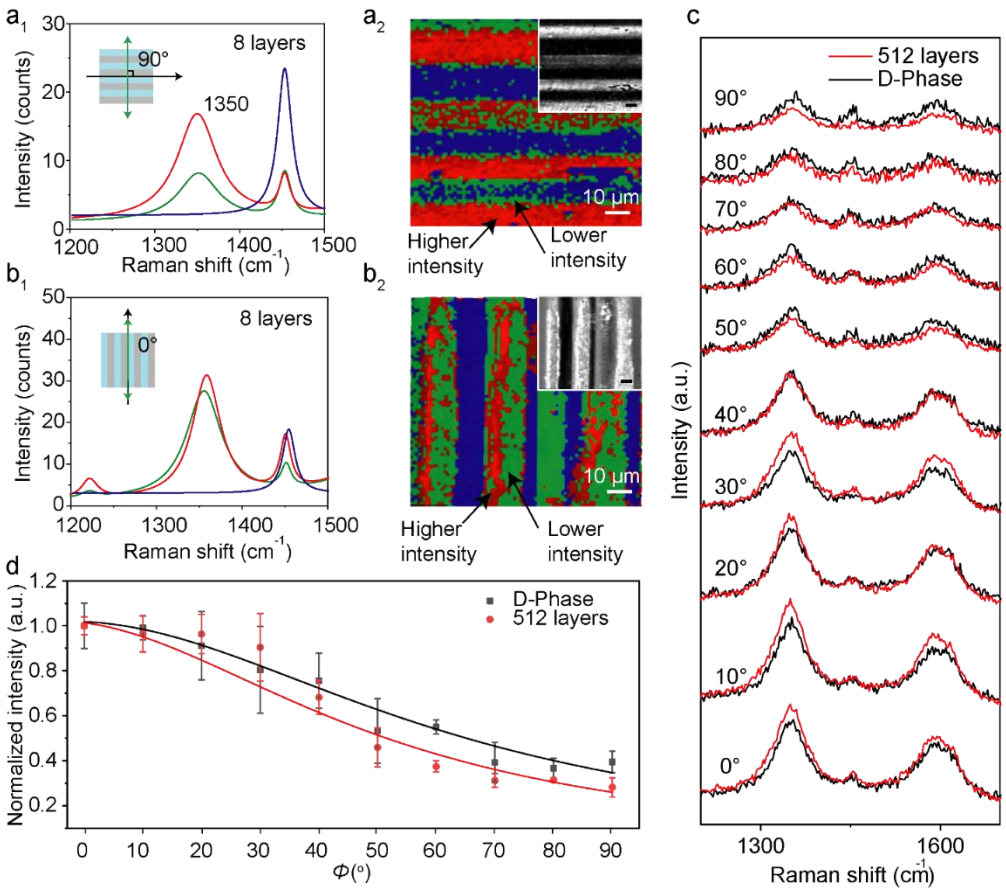

Figure 64. Polarized Raman spectroscopy mapping. (a_1) The average Raman mapping intensities at Φ=90°. Red, green, and blue curves correspond to the same colored regions in (a_2), where the D-band intensity is higher at the middle (colored in red) and lower towards the edge (colored in green) for each CNT/PAN layer. (b_1) The average Raman intensities at Φ=0°. Red, green, and blue curves correspond to the same colored regions in (b_2) where the D-band intensity is higher at the edge and lower toward the middle. Inserted images are without coloring with a scale bar of 10 μm. (c) The Raman intensities of the 512-layered and D-Phase composite fibers with Φ varying from 0° to 90°. (d) The

normalized D-band intensity as a function of the laser beam-layer misalignment angles for composites with 512-layered and D-Phase fibers.

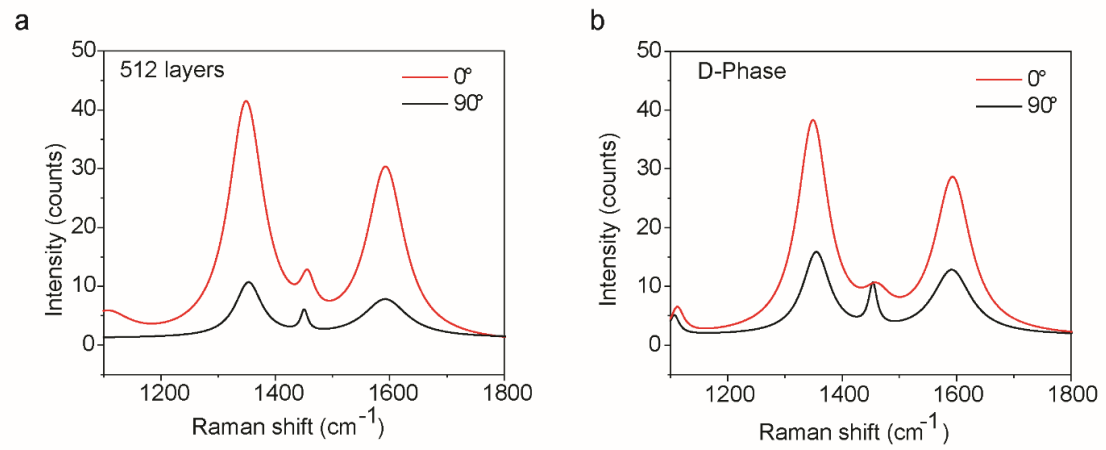

Figure 65. Comparison between the intensity of 0° and 90° for 512-layered and D-Phase fibers shows $I_0°/I_{90}°$ ratios of 3.57 and 2.56, respectively.

5.8 Conclusion

A CNT/PAN-based fiber was fabricated through a process that combined the dry-jet wet spinning and forced assembly techniques, enabling structural control of multilayered fiber morphology. The mechanical properties of the fiber gradually increased with increasing layer numbers. At 512 layers (layer thickness of approximately 170 nm), the fibers showed a 27.4% increase in Young's modulus and 22.2% increase in ultimate tensile strength compared to the traditionally dispersed D-Phase fiber (i.e., PAN/0.5 wt% CNTs). The stiffening and strengthening were mainly due to the following factors: (i) improved quality of nanoparticle dispersion, (ii) increased long-range crystallinity of the polymer chains, and (iii) enhanced nanoparticle orientation degree. The optimum dispersion contained nanotubes that were closely packed and continuously aligned. This higher nanoparticle

reinforcement efficiency demonstrated the potential to enhance carbon fibers for diverse mechanical applications. Furthermore, the scalable fabrication of such a hierarchical structure has great application potential in thermal management, energy storage devices, wearable electronics, and electromagnetic shielding.

CHAPTER 6

SUMMARY AND FUTURE OUTLOOK

In conclusion, this dissertation discusses fiber spinning with additive manufacturing as tooling engineering. 1D fibers with versatile internal structures were fabricated, and the process-structure-property relationship has been explored for each fiber type, namely coaxial TPU/GnPs/CNTs for VOC sensing, coaxial PVA/GnPs for electrically conductive fiber, multilayered PVA/BN for thermal conductivity, and multilayered PAN/CNTs for mechanically reinforced carbon fiber. Their performances, such as sensitivity, conductivity, durability, and mechanical properties, have improved with engineered fiber structures. Moreover, in Chapters 2 and 3, the multi-material fiber structures were enabled by 3D printed multi-exit nozzle, where the printing resolution limited the feature size. In Chapters 4 and 5, this issue was overcome by the layer multiplication process, where nanometer-scale features were achieved with millimeter-scale nozzles.

Beyond exploring fibers with complex internal structures, post fiber spinning assembly is one of the directions that has been often overlooked. Following fiber spinning, different types of weaving, such as plain, twill, satin, basket, and leno, all contribute to the overall aesthetic and functional properties. Especially for highly engineered fabrics, parameters including thickness, weight, and orientation are all considered part of the fabrication process. However, this process has been continued for centuries without any significant improvement. Recently, the rapid development of 3D printing, especially direct ink writing (DIW), has gained some momentum to challenge the concept of fiber spinning and

weaving. The DIW-based 3D printing shares many similarities with fiber spinning, such as high compatibility to multi-material composites or hybrids, low viscosity processibility, and flexibility with application-driven structures. Besides, DIW has superior technology transferability due to its user-friendly and straightforward extrusion characteristic, making it one of the most cost-efficient and low footprint manufacturing techniques for making 1D fibers, 2D surface orders, and 3D layers.

Moreover, on top of fiber weaving, where functions and properties mostly depend on the material section, DIW allows independent control over printing pattern, direction, resolution, and speed, opening new pattern-based functions. In essence, the deposition of fibers in DIW incorporates top-down processing (i.e., from fiber to fiber-contained nanoparticle alignment) and bottom-up manufacturing (i.e., from fiber to fiber-stacked layers). As a result, the nanoscale particle alignment, microscale composition selectivity, and macroscale patterns in DIW naturally embrace a cross-scale hierarchy.

Based on these similarities and advantages over the traditional fiber spinning technique, purposely depositing each fiber/filament to construct an overall 3D fiber-based “fabric” is a viable future direction for textile engineering.

REFERENCES

[1] K. N. Keya, N. A. Kona, F. A. Koly, K. M. Maraz, M. N. Islam, R. A. Khan, *Mater. Eng. Res.* **2019**, *1*, 69.

[2] D. Charles, *Science (80-.).* **2009**, *325*, 1329.

[3] E. G. Chatzi, J. L. Koenig, *Polym. Plast. Technol. Eng.* **1987**, *26*, 229.

[4] T. Kato, A. Magario, *Tribol. Trans.* **1994**, *37*, 559.

[5] E. M. Hicks, A. J. Ultee, J. Drougas, *Science (80-.).* **1965**, *147*, 373.

[6] Y. Qiu, P. Schwartz, *Compos. Sci. Technol.* **1993**, *47*, 289.

[7] P. J. Rivero, A. Urrutia, J. Goicoechea, F. J. Arregui, *Nanoscale Res. Lett.* **2015**, *10*, 1.

[8] R. J. Diefendorf, E. Tokarsky, *Polym. Eng. Sci.* **1975**, *15*, 150.

[9] D. B. Eagles, B. F. Blumentritt, S. L. Cooper, *J. Appl. Polym. Sci.* **1976**, *20*, 435.

[10] A. E. Standage, R. Matkowsky, *Nature* **1969**, *224*, 688.

[11] K. Song, Y. Zhang, J. Meng, E. C. Green, N. Tajaddod, H. Li, M. L. Minus, **2013**, *6*, 2543.

[12] R. Vogel, B. Tändler, D. Voigt, D. Jehnichen, L. Häußler, L. Peitzsch, H. Brünig, *Macromol. Biosci.* **2007**, *7*, 820.

[13] J. E. Spruiell, J. L. White, *Polym. Eng. Sci.* **1975**, *15*, 660.

[14] R. Zhu, V. Yadama, H. Liu, R. J. T. Lin, D. P. Harper, *Compos. Part A Appl. Sci. Manuf.* **2017**, *97*, 111.

[15] T. Kaneda, T. Katsura, K. Nakagawa, *Polymer (Guildf).* **1986**, *32*, 3151.

[16] Y. Gong, Y. Wei, J. Cheng, T. Jiang, L. Chen, B. Xu, *Sci. Total Environ.* **2017**, *574*, 1432.

[17] M. P. Vocht, R. Beyer, P. Thomasic, A. Müller, A. Ota, F. Hermanutz, M. R. Buchmeiser, *Cellulose* **2021**, *28*, 3055.

[18] B. Gupta, N. Revagade, N. Anjum, B. Atthoff, J. Hilborn, *J. Appl. Polym. Sci.* **2006**, *100*, 1239.

[19] Y. Dzenis, *Science (80-.).* **2004**, *304*, 1917.

[20] D. Papkov, N. Delpouve, L. Delbreilh, S. Araujo, T. Stockdale, S. Mamedov, K. Maleckis, Y. Zou, M. N. Andalib, E. Dargent, V. P. Dravid, M. V. Holt, C. Pellerin, Y. A. Dzenis, *ACS Nano* **2019**, *13*, 4893.

[21] O. Nechyporchuk, R. Bordes, T. Köhnke, *ACS Appl. Mater. Interfaces* **2017**, *9*, 39069.

[22] A. R. Bhattacharyya, T. V. Sreekumar, T. Liu, S. Kumar, L. M. Ericson, R. H. Hauge, R. E. Smalley, *Polymer (Guildf).* **2003**, *44*, 2373.

[23] C. H. Choi, H. Yi, S. Hwang, D. A. Weitz, C. S. Lee, *Lab Chip* **2011**, *11*, 1477.

[24] D. Li, M. M. Jacobsen, N. G. Rim, D. Backman, D. L. Kaplan, J. Y. Wong, *Biofabrication* **2017**, *9*, 025025.

[25] F. Wu, X. J. Ju, X. H. He, M. Y. Jiang, W. Wang, Z. Liu, R. Xie, B. He, L. Y. Chu, *J. Mater. Chem. B* **2016**, *4*, 2455.

[26] Y. Zhang, C. F. Wang, L. Chen, S. Chen, A. J. Ryan, *Adv. Funct. Mater.* **2015**, *25*, 7253.

[27] X. Y. Du, Q. Li, G. Wu, S. Chen, *Adv. Mater.* **2019**, *31*, 1903733.

[28] W. S. Khan, R. Asmatulu, M. Ceylan, A. Jabbarnia, *Fibers Polym.* **2013**, *14*, 1235.

[29] W. Xu, S. Jambhulkar, D. Ravichandran, Y. Zhu, M. Kakarla, Q. Nian, B. Azeredo, X. Chen, K. Jin, B. Vernon, D. G. Lott, J. L. Cornella, O. Shefi, G. Miquelard-Garnier, Y. Yang, K. Song, *Small* **2021**, *2100817*, 2100817.

[30] J. Xiong, J. Chen, P. S. Lee, *Adv. Mater.* **2021**, *33*, 2002640.

[31] Y. Zhang, J. Ding, B. Qi, W. Tao, J. Wang, C. Zhao, H. Peng, J. Shi, *Adv. Funct. Mater.* **2019**, *29*, 1902834.

[32] K. Dong, X. Peng, Z. L. Wang, *Adv. Mater.* **2020**, *32*, 1902549.

[33] J. S. Heo, J. Eom, Y. H. Kim, S. K. Park, *Small* **2018**, *14*, 1703034.

[34] L. Wang, X. Fu, J. He, X. Shi, T. Chen, P. Chen, B. Wang, H. Peng, *Adv. Mater.* **2020**, *32*, 1901971.

[35] S. Mane, *Canchemtrans.Net* **2016**, *4*, 210.

[36] F. R. Mansour, S. Waheed, B. Paull, F. Maya, *J. Sep. Sci.* **2020**, *43*, 56.

[37] S. Yarova, D. Jones, F. Jaouen, S. Cavaliere, *Surfaces* **2019**, *2*, 159.

[38] D. Shahriari, G. Loke, I. Tafel, S. Park, P. H. Chiang, Y. Fink, P. Anikeeva, *Adv. Mater.* **2019**, *31*, 1902021.

[39] A. I. Cooper, A. B. Holmes, *Adv. Mater.* **1999**, *11*, 1270.

[40] B. P. Santora, M. R. Gagné, K. G. Moloyt, N. S. Radu, *Macromolecules* **2001**, *34*, 658.

[41] J. Lin, B. Ding, J. Yang, J. Yu, G. Sun, *Nanoscale* **2012**, *4*, 176.

[42] P. Dayal, T. Kyu, *J. Appl. Phys.* **2006**, *100*, 043512.

[43] J. Wang, X. Jiang, H. Zhang, S. Liu, L. Bai, H. Liu, *Anal. Methods* **2015**, *7*, 7879.

[44] D. Ravichandran, W. Xu, R. Franklin, N. Kanth, S. Jambhulkar, S. Shukla, K. Song, *Molecules* **2019**, *24*, 025002.

[45] B. Grena, J. B. Alayrac, E. Levy, A. M. Stolyarov, J. D. Joannopoulos, Y. Fink, *Nat. Commun.* **2017**, *8*, 364.

[46] J. Gao, X. Wang, W. Zhai, H. Liu, G. Zheng, K. Dai, L. Mi, C. Liu, C. Shen, *ACS Appl. Mater. Interfaces* **2018**, *10*, 34592.

[47] Y. Yu, Y. Zhai, Z. Yun, W. Zhai, X. Wang, G. Zheng, C. Yan, K. Dai, C. Liu, C. Shen, *Adv. Electron. Mater.* **2019**, *5*, 1900538.

[48] N. Kanth, W. Xu, U. Prasad, D. Ravichandran, A. M. Kannan, K. Song, *Nanomaterials* **2020**, *10*, 1.

[49] A. D. Roberts, J. S. M. Lee, A. Magaz, M. W. Smith, M. Dennis, N. S. Scrutton, J. J. Blaker, *Molecules* **2020**, *25*, 1207.

[50] E. L. G. Medeiros, A. L. Braz, I. J. Porto, A. Menner, A. Bismarck, A. R. Boccaccini, W. C. Lepry, S. N. Nazhat, E. S. Medeiros, J. J. Blaker, *ACS Biomater. Sci. Eng.* **2016**, *2*, 1442.

[51] H. Zhang, I. Hussain, M. Brust, M. F. Butler, S. P. Rannard, A. I. Cooper, *Nat. Mater.* **2005**, *4*, 787.

[52] Y. Cui, H. Gong, Y. Wang, D. Li, H. Bai, *Adv. Mater.* **2018**, *30*, 1706807.

[53] J. Zhao, H. Lu, Y. Zhang, S. Yu, O. I. Malyi, X. Zhao, L. Wang, H. Wang, J. Peng, X. Li, Y. Zhang, S. Chen, H. Pan, G. Xing, C. Lu, Y. Tang, X. Chen, *Sci. Adv.* **2021**, *7*, eabd6978.

[54] Z. Zhang, L. Cui, X. Shi, X. Tian, D. Wang, C. Gu, E. Chen, X. Cheng, Y. Xu, Y. Hu, J. Zhang, L. Zhou, H. H. Fong, P. Ma, G. Jiang, X. Sun, B. Zhang, H. Peng, *Adv. Mater.* **2018**, *30*, 1800323.

[55] M. Antonini, A. Sahasrabudhe, A. Tabet, M. Schwalm, D. Rosenfeld, I. Garwood, J. Park, G. Loke, T. Khudiyev, M. Kanik, N. Corbin, A. Canales, A. Jasanoff, Y. Fink, P. Anikeeva, *Adv. Funct. Mater.* **2021**, *2104857*, 2104857.

[56] N. Shirolkar, A. Maffe, E. DiLoreto, P. J. Arias-Monje, M. Lu, J. Ramachandran, P. Gulgunje, K. Gupta, J. G. Park, K. C. Shih, M. H. Kirmani, A. Sharits, D. Nepal, M. P. Nieh, R. Liang, T. Tsotsis, S. Kumar, *Carbon N. Y.* **2021**, *174*, 730.

[57] K. Flynn, R. O'Leary, C. Roux, B. J. Reedy, *J. Forensic Sci.* **2006**, *51*, 586.

[58] G. M. Spinks, *Adv. Mater.* **2020**, *32*, 1904093.

[59] R. Y. F. Liu, Y. Jin, A. Hiltner, E. Baer, **2003**, *24*, 943.

[60] M. Ponting, A. Hiltner, E. Baer, *Macromol. Symp.* **2010**, *294*, 19.

[61] H. Meng, X. Jiang, Y. Yu, Z. Wang, J. Wu, *Korean J. Chem. Eng.* **2017**, *34*, 1328.

[62] M. K. Singh, P. D. Anderson, H. E. H. Meijer, *Macromol. Rapid Commun.* **2009**, *30*, 362.

[63] C. Chávez-Madero, M. D. De León-Derby, M. Samandari, C. F. Ceballos-González, E. J. Bolívar-Monsalve, C. Mendoza-Buenrostro, S. Holmberg, N. A. Garza-Flores, M. A. Almajhadi, I. González-Gamboa, J. F. Yee-De León, S. O. Martínez-Chapa, C. A. Rodríguez, H. K. Wickramasinghe, M. Madou, D. Dean, A. Khademhosseini, Y. S. Zhang, M. M. Alvarez, G. Trujillo-De Santiago, *Biofabrication* **2020**, *12*, 035023.

[64] E. J. Bolívar-Monsalve, C. F. Ceballos-González, K. I. Borrayo-Montaño, D. A. Quevedo-Moreno, J. F. Yee-de León, A. Khademhosseini, P. S. Weiss, M. M. Alvarez, G. Trujillo-de Santiago, *Bioprinting* **2021**, *21*, e00125.

[65] M. Rein, V. D. Favrod, C. Hou, T. Khudiyev, A. Stolyarov, J. Cox, C. C. Chung, C. Chhav, M. Ellis, J. Joannopoulos, Y. Fink, *Nature* **2018**, *560*, 214.

[66] Z. Wang, T. Wu, Z. Wang, T. Zhang, M. Chen, J. Zhang, L. Liu, M. Qi, Q. Zhang, J. Yang, W. Liu, H. Chen, Y. Luo, L. Wei, *Nat. Commun.* **2020**, *11*, 3842.

[67] S. Feng, Y. Hou, Y. Chen, Y. Xue, Y. Zheng, L. Jiang, *J. Mater. Chem. A* **2013**, *1*, 8363.

[68] M. A. Skylar-Scott, J. Mueller, C. W. Visser, J. A. Lewis, *Nature* **2019**, *575*, 330.

[69] J. Chen, H. Wen, G. Zhang, F. Lei, Q. Feng, Y. Liu, X. Cao, H. Dong, *ACS Appl. Mater. Interfaces* **2020**, *12*, 7565.

[70] T. Ding, K. H. Chan, Y. Zhou, X. Q. Wang, Y. Cheng, T. Li, G. W. Ho, *Nat. Commun.* **2020**, *11*, 6006.

[71] Y. Yang, X. Li, M. Chu, H. Sun, J. Jin, K. Yu, Q. Wang, Q. Zhou, Y. Chen, *Sci. Adv.* **2019**, *5*, eaau9490.

[72] J. Liu, W. Li, Y. Guo, H. Zhang, Z. Zhang, *Compos. Part A Appl. Sci. Manuf.* **2019**, *120*, 140.

[73] C. Zhao, P. Zhang, J. Zhou, S. Qi, Y. Yamauchi, R. Shi, R. Fang, Y. Ishida, S. Wang, A. P. Tomsia, L. Jiang, M. Liu, *Nature* **2020**, *580*, 210.

[74] R. Sharma, C. Y. Lee, J. H. Choi, K. Chen, M. S. Strano, *Nano Lett.* **2007**, *7*, 2693.

[75] M. S. Scholz, B. W. Drinkwater, R. S. Trask, *Ultrasonics* **2014**, *54*, 1015.

[76] Y. Guo, S. Batra, Y. Chen, E. Wang, M. Cakmak, *ACS Appl. Mater. Interfaces* **2016**, *8*, 18471.

[77] S. Wu, R. B. Ladani, J. Zhang, E. Bafekrpour, K. Ghorbani, A. P. Mouritz, A. J. Kinloch, C. H. Wang, *Carbon N. Y.* **2015**, *94*, 607.

[78] Y. Kim, H. Yuk, R. Zhao, S. A. Chester, X. Zhao, *Nature* **2018**, *558*, 274.

[79] Y. Li, N. Mehra, T. Ji, X. Yang, L. Mu, J. Gu, J. Zhu, *Nanoscale* **2018**, *10*, 1695.

[80] V. Sazonova, Y. Yalsh, I. Üstünel, D. Roundy, T. A. Arlas, P. L. McEuen, *Nature* **2004**, *431*, 284.

[81] G. L. Goh, S. Agarwala, W. Y. Yeong, *Adv. Mater. Interfaces* **2019**, *6*, 1801318.

[82] B. G. Compton, J. A. Lewis, *Adv. Mater.* **2014**, *26*, 5930.

[83] P. Wadsworth, I. Nelson, D. L. Porter, B. Raeymaekers, S. E. Naleway, *Mater. Des.* **2020**, *185*, 108243.

[84] J. J. Martin, B. E. Fiore, R. M. Erb, *Nat. Commun.* **2015**, *6*, 8641.

[85] X. Wang, H. Zhai, B. Qie, Q. Cheng, A. Li, J. Borovilas, B. Xu, C. Shi, T. Jin, X. Liao, Y. Li, X. He, S. Du, Y. Fu, M. Dontigny, K. Zaghib, Y. Yang, *Nano Energy* **2019**, *60*, 205.

[86] Y. Cui, H. Gong, Y. Wang, D. Li, H. Bai, *Adv. Mater.* **2018**, *30*, 1706807.

[87] S. Jambhulkar, S. Liu, P. Vala, W. Xu, D. Ravichandran, Y. Zhu, K. Bi, Q. Nian, X. Chen, K. Song, *ACS Nano* **2021**, Online.

[88] G. Chu, A. Camposeo, R. Vilensky, G. Vasilyev, P. Martin, D. Pisignano, E. Zussman, *Matter* **2019**, *1*, 988.

[89] S. Jambhulkar, W. Xu, D. Ravichandran, J. Prakash, A. Nadar, M. Kannan, K. Song, *Nano Lett.* **2020**, *20*, 3199.

[90] M. Saeidijavash, J. Garg, B. Grady, B. Smith, Z. Li, R. J. Young, F. Tarannum, N. Bel Bekri, *Nanoscale* **2017**, *9*, 12867.

[91] W. Wang, N. S. Murthy, H. Gi, S. Kumar, *Polymer (Guildf).* **2008**, *49*, 2133.

[92] W. Xu, S. Jambhulkar, R. Verma, R. Franklin, D. Ravichandran, K. Song, *Nanoscale Adv.* **2019**, *1*, 2510.

[93] N. Tajaddod, K. Song, E. C. Green, Y. Zhang, M. L. Minus, *Macromol. Mater. Eng.* **2016**, *301*, 315.

[94] Y. Xu, W. Hong, H. Bai, C. Li, G. Shi, *Carbon N. Y.* **2009**, *47*, 3538.

[95] Z. Li, R. J. Young, N. R. Wilson, I. A. Kinloch, C. Vallés, Z. Li, *Compos. Sci. Technol.* **2016**, *123*, 125.

[96] G. R. Liu, *Compos. Struct.* **1997**, *40*, 313.

[97] K. Song, R. Polak, D. Chen, M. F. Rubner, R. E. Cohen, K. A. Askar, *ACS Appl. Mater. Interfaces* **2016**, *8*, 20396.

[98] Y. X. Wang, C. G. Wang, Y. J. Bai, Z. Bo, *J. Appl. Polym. Sci.* **2007**, *104*, 1026.

[99] D. G. Papageorgiou, I. A. Kinloch, R. J. Young, *Prog. Mater. Sci.* **2017**, *90*, 75.

[100] S. Gbordzoe, S. Yarmolenko, Y. Y. Hsieh, P. K. Adusei, N. T. Alvarez, S. Fialkova, V. Shanov, *Carbon N. Y.* **2017**, *121*, 591.

[101] A. D. Maynard, *Nat. Nanotechnol.* **2015**, *10*, 1005.

[102] J. V. L. Silva, R. A. Rezende, *IFAC Proc. Vol.* **2013**, *6*, 277.

[103] T. D. Ngo, A. Kashani, G. Imbalzano, K. T. Q. Nguyen, D. Hui, *Compos. Part B Eng.* **2018**, *143*, 172.

[104] M. Power, A. J. Thompson, S. Anastasova, G. Z. Yang, *Small* **2018**, *14*, 1703964.

[105] C. M. B. Ho, S. H. Ng, K. H. H. Li, Y. J. Yoon, *Lab Chip* **2015**, *15*, 3627.

[106] J. U. Park, M. Hardy, S. J. Kang, K. Barton, K. Adair, D. K. Mukhopadhyay, C. Y. Lee, M. S. Strano, A. G. Alleyne, J. G. Georgiadis, P. M. Ferreira, J. A. Rogers, *Nat. Mater.* **2007**, *6*, 782.

[107] J. P. Kruth, X. Wang, T. Laoui, L. Froyen, *Assem. Autom.* **2003**, *23*, 357.

[108] B. P. Croom, A. Abbott, J. W. Kemp, L. Rueschhoff, L. Smieska, A. Woll, S. Stoupin, H. Koerner, *Addit. Manuf.* **2021**, *37*, 101701.

[109] A. G. Hasib, S. Niauzorau, W. Xu, S. Niverty, N. Kublik, J. Williams, N. Chawla, K. Song, B. Azeredo, Rheology scaling of spherical metal powders dispersed in thermoplastics and its correlation to the extrudability of filaments for 3D printing. *Addit. Manuf.* **2021**, *41*, 101967.

[110] C. D. Armstrong, N. Todd, A. T. Alsharhan, D. I. Bigio, R. D. Sochol, *Adv. Mater. Technol.* **2021**, *6*, 2000829.

[111] R. Cornock, S. Beirne, B. Thompson, G. G. Wallace, *Biofabrication* **2014**, *6*, 025002.

[112] X. Li, J. M. Zhang, X. Yi, Z. Huang, P. Lv, H. Duan, *Adv. Sci.* **2019**, *6*, 1800730.

[113] R. Franklin, W. Xu, D. Ravichandran, S. Jambhulkar, Y. Zhu, K. Song, *J. Mater. Sci. Technol.* **2021**, *95*, 78.

[114] A. Lüken, M. Geiger, L. Steinbeck, A. C. Joel, A. Lampert, J. Linkhorst, M. Wessling, *Adv. Healthc. Mater.* **2021**, *10*, 2100898.

[115] R. Nazari, S. Zaare, R. C. Alvarez, K. Karpos, T. Engelman, C. Madsen, G. Nelson, J. C. H. Spence, U. Weierstall, R. J. Adrian, R. A. Kirian, *Opt. Express* **2020**, *28*, 21749.

[116] A. H. Jalal, F. Alam, S. Roychoudhury, Y. Umasankar, N. Pala, S. Bhansali, *ACS Sensors* **2018**, *3*, 1246.

[117] J. E. Colman Lerner, E. Y. Sanchez, J. E. Sambeth, A. A. Porta, *Atmos. Environ.*

2012, *55*, 440.

[118] J. Madureira, I. Paciência, J. Rufo, M. Severo, E. Ramos, H. Barros, E. de Oliveira Fernandes, *Build. Environ.* **2016**, *96*, 198.

[119] B. J. Finlayson-Pitts, J. N. Pitts, *Science (80-.).* **1997**, *276*, 1045.

[120] B. Pejcic, P. Eadington, A. Ross, *Environ. Sci. Technol.* **2007**, *41*, 6333.

[121] K. Urashima, J. S. Chang, *IEEE Trans. Dielectr. Electr. Insul.* **2000**, *7*, 602.

[122] K. Kobashi, T. Villmow, T. Andres, P. Pötschke, *Sensors Actuators, B Chem.* **2008**, *134*, 787.

[123] Q. Fan, Z. Qin, T. Villmow, J. Pionteck, P. Pötschke, Y. Wu, B. Voit, M. Zhu, *Sensors Actuators, B Chem.* **2011**, *156*, 63.

[124] S. Y. Cho, H. W. Yoo, J. Y. Kim, W. Bin Jung, M. L. Jin, J. S. Kim, H. J. Jeon, H. T. Jung, *Nano Lett.* **2016**, *16*, 4508.

[125] G. Siqueira, D. Kokkinis, R. Libanori, M. K. Hausmann, A. S. Gladman, A. Neels, P. Tingaut, T. Zimmermann, J. A. Lewis, A. R. Studart, *Adv. Funct. Mater.* **2017**, *27*, 1604619.

[126] J. van den Broek, S. Abegg, S. E. Pratsinis, A. T. Güntner, *Nat. Commun.* **2019**, *10*, 4220.

[127] B. L. Li, J. Wang, H. L. Zou, S. Garaj, C. T. Lim, J. Xie, N. B. Li, D. T. Leong, *Adv. Funct. Mater.* **2016**, *26*, 7034.

[128] A. T. Güntner, N. J. Pineau, D. Chie, F. Krumeich, S. E. Pratsinis, *J. Mater. Chem. B* **2016**, *4*, 5358.

[129] A. T. Güntner, S. Abegg, K. Königstein, P. A. Gerber, A. Schmidt-Trucksäss, S. E. Pratsinis, *ACS Sensors* **2019**, *4*, 268.

[130] J. Wu, H. Li, Z. Yin, H. Li, J. Liu, X. Cao, Q. Zhang, H. Zhang, *Small* **2013**, *9*, 3314.

[131] X. Lu, M. I. B. Utama, J. Zhang, Y. Zhao, Q. Xiong, *Nanoscale* **2013**, *5*, 8904.

[132] X. Wang, W. Fan, Z. Fan, W. Dai, K. Zhu, S. Hong, Y. Sun, J. Wu, K. Liu, *Nanoscale* **2018**, *10*, 3540.

[133] L. Han, K. Liu, M. Wang, K. Wang, L. Fang, H. Chen, J. Zhou, X. Lu, *Adv. Funct. Mater.* **2018**, *28*, 1.

[134] S. Guo, K. Qiu, F. Meng, S. H. Park, M. C. Mcalpine, **2017**, *29*, 1701218.

[135] B. Khatri, K. Lappe, D. Noetzel, K. Pursche, T. Hanemann, *Materials (Basel).* **2018**, *11*.

[136] A. C. De Leon, Q. Chen, N. B. Palaganas, J. O. Palaganas, J. Manapat, R. C. Advincula, *React. Funct. Polym.* **2016**, *103*, 141.

[137] Y. Joo, J. Byun, N. Seong, J. Ha, H. Kim, S. Kim, T. Kim, H. Im, D. Kim, Y. Hong, *Nanoscale* **2015**, *7*, 6208.

[138] X. Liao, Q. Liao, X. Yan, Q. Liang, H. Si, M. Li, H. Wu, S. Cao, Y. Zhang, *Adv. Funct. Mater.* **2015**, *25*, 2395.

[139] M. Castro, J. Lu, S. Bruzaud, B. Kumar, J. F. Feller, *Carbon N. Y.* **2009**, *47*, 1930.

[140] H. Xie, Q. Yang, X. Sun, J. Yang, Y. Huang, *Sensors Actuators, B Chem.* **2006**, *113*, 887.

[141] C. Tasaltin, F. Basarir, *Sensors Actuators, B Chem.* **2014**, *194*, 173.

[142] S. Z. Guo, X. Yang, M. C. Heuzey, D. Therriault, *Nanoscale* **2015**, *7*, 6451.

[143] P. C. Sherrell, C. Mattevi, *Mater. Today* **2016**, *19*, 428.

[144] S. Virji, J. Huang, R. B. Kaner, B. H. Weiller, *Nano Lett.* **2004**, *4*, 491.

[145] H. Liu, M. Dong, W. Huang, J. Gao, K. Dai, J. Guo, G. Zheng, C. Liu, C. Shen, Z. Guo, *J. Mater. Chem. C* **2017**, *5*, 73.

[146] B. Zhu, K. Li, J. Liu, H. Liu, C. Sun, C. E. Snape, Z. Guo, *J. Mater. Chem. A* **2014**, *2*, 5481.

[147] K. Krukiewicz, M. Krzywiecki, M. J. P. Biggs, D. Janas, *RSC Adv.* **2018**, *8*, 30600.

[148] J. G. Um, Y. S. Jun, H. Alhumade, H. Krithivasan, G. Lui, A. Yu, *RSC Adv.* **2018**, *8*, 17091.

[149] Z. He, G. Zhou, J. H. Byun, S. K. Lee, M. K. Um, B. Park, T. Kim, S. B. Lee, T. W. Chou, *Nanoscale* **2019**, *11*, 5884.

[150] J. J. Park, W. J. Hyun, S. C. Mun, Y. T. Park, O. O. Park, *ACS Appl. Mater. Interfaces* **2015**, *7*, 6317.

[151] S. Han, Q. Meng, X. Pan, T. Liu, S. Zhang, Y. Wang, S. Haridy, S. Araby, *J. Appl.*

Polym. Sci. **2019**, *136*, 1.

[152] Y. Li, T. Yang, T. Yu, L. Zheng, K. Liao, *J. Mater. Chem.* **2011**, *21*, 10844.

[153] J. C. Halpin, *J. Compos. Mater.* **1969**, *3*, 732.

[154] Y. Benveniste, *Mech. Mater.* **1987**, *6*, 147.

[155] B. Zhang, R. W. Fu, M. Q. Zhang, X. M. Dong, P. L. Lan, J. S. Qiu, *Sensors Actuators, B Chem.* **2005**, *109*, 323.

[156] B. Pan, B. Xing, *Environ. Sci. Technol.* **2008**, *42*, 9005.

[157] J. X. Jiang, F. Su, A. Trewin, C. D. Wood, H. Niu, J. T. A. Jones, Y. Z. Khimyak, A. I. Cooper, *J. Am. Chem. Soc.* **2008**, *130*, 7710.

[158] U. H. Shin, D. W. Jeong, S. M. Park, S. H. Kim, H. W. Lee, J. M. Kim, *Carbon N. Y.* **2014**, *80*, 396.

[159] R. Zhang, Y. Bin, R. Chen, M. Matsuo, **2013**, *45*, 1120.

[160] R. Buchdahl, L. E. Nielsen, *J. Appl. Phys.* **1952**, *23*, 600.

[161] L. Jin, C. Bower, O. Zhou, *Appl. Phys. Lett.* **1998**, *73*, 1197.

[162] M. Yoonessi, J. R. Gaier, *ACS Nano* **2010**, *4*, 7211.

[163] N. Yousefi, M. M. Gudarzi, Q. Zheng, S. H. Aboutalebi, F. Sharif, J. K. Kim, *J. Mater. Chem.* **2012**, *22*, 12709.

[164] G. C. Han, S. Kumar, *Science (80-.).* **2008**, *319*, 908.

[165] C. Shao, H. Y. Kim, J. Gong, B. Ding, D. R. Lee, S. J. Park, *Mater. Lett.* **2003**, *57*, 1579.

[166] A. K. Patel, R. Bajpai, J. M. Keller, *Microsyst. Technol.* **2014**, *20*, 41.

[167] K. Song, Y. Zhang, J. Meng, M. L. Minus, *J. Appl. Polym. Sci.* **2013**, *127*, 2977.

[168] Z. Li, R. J. Young, I. A. Kinloch, N. R. Wilson, A. J. Marsden, A. P. A. Raju, *Carbon N. Y.* **2015**, *88*, 215.

[169] Z. Li, R. J. Young, N. R. Wilson, I. A. Kinloch, C. Vallés, Z. Li, *Compos. Sci. Technol.* **2016**, *123*, 125.

[170] X. Zhao, Q. Zhang, D. Chen, P. Lu, *Macromolecules* **2010**, *43*, 2357.

[171] J. W. Kim, J. S. Lee, *Fibers Polym.* **2017**, *18*, 81.

[172] M. F. H. Wolff, V. Salikov, S. Antonyuk, S. Heinrich, G. A. Schneider, *Compos. Sci. Technol.* **2014**, *90*, 154.

[173] L. Zhang, X. Liu, A. Deb, G. Feng, *ACS Sustain. Chem. Eng.* **2019**, *7*, 19910.

[174] Y. Zhao, B. Zhang, B. Yao, Y. Qiu, Z. Peng, Y. Zhang, Y. Alsaid, I. Frenkel, K. Youssef, Q. Pei, X. He, *Matter* **2020**, *3*, 1196.

[175] L. Yin, K. N. Kim, J. Lv, F. Tehrani, M. Lin, Z. Lin, J. M. Moon, J. Ma, J. Yu, S. Xu, J. Wang, *Nat. Commun.* **2021**, *12*, 1542.

[176] Y. Cheng, Y. Ma, L. Li, M. Zhu, Y. Yue, W. Liu, L. Wang, S. Jia, C. Li, T. Qi, J. Wang, Y. Gao, *ACS Nano* **2020**, *14*, 2145.

[177] S. Z. Guo, K. Qiu, F. Meng, S. H. Park, M. C. McAlpine, *Adv. Mater.* **2017**, *29*, 1701218.

[178] Y. Chen, Z. Deng, R. Ouyang, R. Zheng, Z. Jiang, H. Bai, H. Xue, *Nano Energy* **2021**, *84*, 105866.

[179] Z. Wang, J. Ren, R. Liu, X. Sun, D. Huang, W. Xu, J. Jiang, K. Ma, Y. Liu, *Compos. Part A Appl. Sci. Manuf.* **2020**, *136*, 105957.

[180] Y. Zhu, W. Xu, D. Ravichandran, S. Jambhulkar, K. Song, *J. Mater. Chem. A* **2021**, *9*, 8514.

[181] Y. Liu, X. Zhang, Y. Xia, H. Yang, *Adv. Mater.* **2010**, *22*, 2454.

[182] S. Jambhulkar, S. Liu, P. Vala, W. Xu, D. Ravichandran, Y. Zhu, K. Bi, Q. Nian, X. Chen, K. Song, *ACS Nano* **2021**, *15*, 12057.

[183] K. M. Pawelec, H. A. van Boxtel, S. G. J. M. Kluijtmans, *Mater. Sci. Eng. C* **2017**, *76*, 628.

[184] V. Kumar, V. Shirke, K. D. P. Nigam, *Chem. Eng. J.* **2008**, *139*, 284.

[185] D. M. Hobbs, F. J. Muzzio, *Chem. Eng. J.* **1997**, *67*, 153.

[186] Y. Fang, G. Chen, M. Bick, J. Chen, *Chem. Soc. Rev.* **2021**, *50*, 9357.

[187] L. Gong, Y. Wang, X. Cheng, R. Zhang, H. Zhang, *Int. J. Heat Mass Transf.* **2013**,

67, 253.

[188] H. Chen, V. V. Ginzburg, J. Yang, Y. Yang, W. Liu, Y. Huang, L. Du, B. Chen, *Prog. Polym. Sci.* **2016**, *59*, 41.

[189] C. Huang, X. Qian, R. Yang, *Mater. Sci. Eng. R Reports* **2018**, *132*, 1.

[190] J. Wang, J. K. Carson, M. F. North, D. J. Cleland, *Int. J. Heat Mass Transf.* **2008**, *51*, 2389.

[191] L. Gong, Y. Wang, X. Cheng, R. Zhang, H. Zhang, *Int. J. Heat Mass Transf.* **2014**, *68*, 295.

[192] T. Gao, Z. Yang, C. Chen, Y. Li, K. Fu, J. Dai, E. M. Hitz, H. Xie, B. Liu, J. Song, B. Yang, L. Hu, *ACS Nano* **2017**, *11*, 11513.

[193] X. Yu, Y. Li, X. Wang, Y. Si, J. Yu, B. Ding, *ACS Appl. Mater. Interfaces* **2020**, *12*, 32078.

[194] M. Lu, J. Liao, P. V. Gulgunje, H. Chang, P. J. Arias-Monje, J. Ramachandran, V. Breedveld, S. Kumar, *Polymer (Guildf).* **2021**, *215*, 123369.

[195] K. Chatterjee, T. K. Ghosh, *Adv. Mater.* **2020**, *32*, 1902086.

[196] A. Etaati, S. Pather, Z. Fang, H. Wang, *Compos. Part B* **2014**, *62*, 19.

[197] Y. Rao, *Particuology* **2010**, *8*, 549.

[198] B. Oktay, N. Kayaman-Apohan, S. Erdem-Kuruca, *IOP Conf. Ser. Mater. Sci. Eng.* **2014**, *64*, 012011.

[199] K. Song, Y. Zhang, J. Meng, M. L. Minus, *J. Appl. Polym. Sci.* **2013**, *127*, 2977.

[200] R. Jan, P. May, A. P. Bell, A. Habib, U. Khan, J. N. Coleman, *Nanoscale* **2014**, *6*, 4889.

[201] V. Guerra, C. Wan, T. McNally, *Prog. Mater. Sci.* **2019**, *100*, 170.

[202] P. M. Ajayan, J. Suhr, N. Koratkar, *J. Mater. Sci.* **2006**, *41*, 7824.

[203] G. Szebényi, B. Magyar, T. Czigany, *Adv. Eng. Mater.* **2021**, *23*, 2000822.

[204] M. Fan, J. Domblesky, K. Jin, L. Qin, S. Cui, X. Guo, N. Kim, J. Tao, *Mater. Des.* **2016**, *99*, 535.

[205] R. Dai, G. Chandrasekaran, J. Chen, C. Jackson, Y. Liu, Q. Nian, B. Kwon, *Int. J. Therm. Sci.* **2021**, *169*, 107045.

[206] J. Hu, Y. Huang, X. Zeng, Q. Li, L. Ren, R. Sun, J. Bin Xu, C. P. Wong, *Compos. Sci. Technol.* **2018**, *160*, 127.

[207] P. Tervola, *Int. J. Heat Mass Transf.* **1989**, *32*, 1425.

[208] X. Zhang, R. Xiong, S. Kang, Y. Yang, V. V. Tsukruk, *ACS Nano* **2020**, *14*, 14675.

[209] F. Guo, X. Shen, J. Zhou, D. Liu, Q. Zheng, J. Yang, B. Jia, A. K. T. Lau, J. K. Kim, *Adv. Funct. Mater.* **2020**, *30*, 1910826.

[210] C. Lu, L. Yuan, Q. Guan, G. Liang, A. Gu, *J. Phys. Chem. C* **2018**, *122*, 5238.

[211] Y. C. Soong, C. W. Chiu, *J. Colloid Interface Sci.* **2021**, *599*, 611.

[212] J. P. Lu, *J. Phys. Chem. Solids* **1997**, *58*, 1649.

[213] Y. Ando, X. Zhao, H. Shimoyama, G. Sakai, K. Kaneto, **1999**, *1*, 77.

[214] L. T. O. Nature, **1996**, *382*, 54.

[215] P. Kim, L. Shi, A. Majumdar, P. L. Mceuen, **2001**, 19.

[216] J. Hone, M. Whitney, C. Piskoti, A. Zettl, **1999**, *59*, 2514.

[217] H. G. Chae, Y. H. Choi, M. L. Minus, S. Kumar, *Compos. Sci. Technol.* **2009**, *69*, 406.

[218] H. Liu, J. Gao, W. Huang, K. Dai, G. Zheng, C. Liu, C. Shen, X. Yan, J. Guo, Z. Guo, **2016**, 12977.

[219] X. Yan, J. Gu, G. Zheng, J. Guo, A. Maria, J. Yu, M. Alam, L. Sun, D. P. Young, Q. Zhang, S. Wei, Z. Guo, *Polymer (Guildf).* **2016**, *103*, 315.

[220] M. Razlan, M. Helmi, A. Kudus, H. Akil, *Compos. Part B* **2017**, *119*, 57.

[221] Y. Lee, V. T. Le, J. Kim, H. Kang, E. S. Kim, **2018**, *1706007*, 1.

[222] H. Chang, J. Luo, P. V. Gulgunje, S. Kumar, *Annu. Rev. Mater. Res.* **2017**, *47*, 331.

[223] S. Deville, E. Saiz, R. K. Nalla, A. P. Tomsia, *Science (80-.).* **2006**, *311*, 515.

[224] C. Properties, **2012**, *4*, 275.

[225] D. E. Tsentalovich, R. J. Headrick, F. Mirri, J. Hao, N. Behabtu, C. C. Young, M. Pasquali, **2017**.

[226] P. Nanocomposites, R. Arrigo, R. Teresi, C. Gambarotti, F. Parisi, G. L. Id, N. T. Dintcheva, 1.

[227] Z. Spitalsky, D. Tasis, K. Papagelis, C. Galiotis, *Prog. Polym. Sci.* **2010**, *35*, 357.

[228] Y. Yang, Z. Chen, X. Song, Z. Zhang, J. Zhang, K. K. Shung, Q. Zhou, Y. Chen, *Adv. Mater.* **2017**, *29*, 1605750.

[229] H. Hu, S. Wang, X. Feng, M. Pauly, G. Decher, Y. Long, *Chem. Soc. Rev.* **2020**, *49*, 509.

[230] X. Wang, Y. Soo, **2006**, *7*, 323.

[231] E. B. Duoss, M. Twardowski, J. A. Lewis, *Adv. Mater.* **2007**, *19*, 3485.

[232] S. L. Ruan, P. Gao, X. G. Yang, T. X. Yu, *Polymer (Guildf).* **2003**, *44*, 5643.

[233] X. Liao, M. Dulle, J. Martins, D. Souza, R. B. Wehrspohn, S. Agarwal, S. Förster, H. Hou, P. Smith, A. Greiner, *Science (80-.).* **2019**, *1379*, 1376.

[234] V. S. Sreenivasan, N. Rajini, A. Alavudeen, V. Arumugaprabu, *Compos. Part B* **2015**, *69*, 76.

[235] C. F. De Lannoy, D. Jassby, D. D. Davis, M. R. Wiesner, *J. Memb. Sci.* **2012**, *415–416*, 718.

[236] H. G. Chae, M. L. Minus, S. Kumar, *Polymer (Guildf).* **2006**, *47*, 3494.

[237] L. Yang, T. Suo, Y. Niu, Z. Wang, D. Yan, H. Wang, *Polymer (Guildf).* **2010**, *51*, 5276.

[238] T. Liu, J. Serrano, J. Elliott, X. Yang, W. Cathcart, Z. Wang, Z. He, G. Liu, *Sci. Adv.* **2020**, *6*, eaaz0906.

[239] B. Zhang, C. Lu, Y. Liu, S. Yuan, *Polym. Degrad. Stab.* **2019**, *170*, 109021.

[240] L. Quan, H. Zhang, L. Xu, *J. Therm. Anal. Calorim.* **2015**, *119*, 1081.

[241] A. Etaati, S. Pather, Z. Fang, H. Wang, *Compos. Part B Eng.* **2014**, *62*, 19.

[242] F. Zahedi, I. Amiri, *Polymer (Guildf).* **2018**, *151*, 187.

[243] W. Xu, S. Jambhulkar, R. Verma, R. Franklin, D. Ravichandran, K. Song, **2019**, *1*, 2510.

[244] T. Liu, S. Kumar, *Chem. Phys. Lett.* **2003**, *378*, 257.

[245] H. Ajiki, T. Ando, **1994**, *201*, 349.

[246] G. L. Goh, N. Saengchairat, S. Agarwala, W. Y. Yeong, T. Tran, **2019**.

[247] P. Galliker, J. Schneider, H. Eghlidi, S. Kress, V. Sandoghdar, D. Poulikakos, *Nat. Commun.* **2012**, *3*, 890.

[248] H. Yuk, X. Zhao, *Adv. Mater.* **2018**, *30*, 1704028.

[249] M. Chen, S. Hu, Z. Zhou, N. Huang, S. Lee, Y. Zhang, R. Cheng, J. Yang, Z. Xu, Y. Liu, H. Lee, X. Huan, S.-P. Feng, H. C. Shum, B. P. Chan, S. K. Seol, J. Pyo, J. Tae Kim, *Nano Lett.* **2021**, *21*, 5186.

[250] J. Hu, M. F. Yu, *Science (80-.).* **2010**, *329*, 313.

[251] M. Chen, Z. Xu, J. H. Kim, S. K. Seol, J. T. Kim, *ACS Nano* **2018**, *12*, 4172.

[252] J. R. Tumbleston, D. Shirvanyants, N. Ermoshkin, R. Janusziewicz, A. R. Johnson, D. Kelly, K. Chen, R. Pinschmidt, J. P. Rolland, A. Ermoshkin, E. T. Samulski, J. M. DeSimone, *Science (80-.).* **2015**, *347*, 1349.

APPENDIX A

STATEMENT OF COAUTHORS' PERMISSIONS

I, Weiheng Xu, committed that all co-authors have granted their permissions for the usage of following publications in this dissertation:

Chapter 1

(1) Xu, W.; Zhu, Y.; Ravichandran, D.; Jambhulkar, S.; Kakarla, M.; Bawareth, M.; Lanke, S.; Song, K. Review of Fiber-Based Three-Dimensional Printing for Applications Ranging from Nanoscale Nanoparticle Alignment to Macroscale Patterning. ACS Appl. Nano Mater. 2021, 4 (8), 7538–7562.

(2) Xu, W.; Ravichandran, D.; Jambhulkar, S.; Zhu, Y.; Song, K., A Mini-Review of Microstructural Control during Composite Fiber Spinning. Polym. Int. 2022, 71 (5), 569-577

Chapter 2

(3) Xu, W.; Ravichandran, D.; Jambhulkar, S.; Franklin, R.; Zhu, Y.; Song, K. Bioinspired, Mechanically Robust Chemiresistor for Inline Volatile Organic Compounds Sensing. Adv. Mater. Technol. 2020, 5 (10), 2000440.

Chapter 3

(4) Xu, W.; Jambhulkar, S.; Verma, R.; Franklin, R.; Ravichandran, D.; Song, K. In Situ Alignment of Graphene Nanoplatelets in Poly(Vinyl Alcohol) Nanocomposite Fibers with Controlled Stepwise Interfacial Exfoliation. Nanoscale Adv. 2019, 1 (7), 2510–2517.

Chapter 4

(5) Xu, W.; Rahul, F.; Ravichandran, D.; Bawareth, M.; Jambhulkar, S.; Zhu, Y.; Kakarla, M.; Ejaz, F.; Kwon, B.; Hassan, M. K.; Al-Ejji. M.; Asadi, A.; Chawla, N.; Song, K. Continuous Nanoparticle Patterning Strategy in Layer-Structured Nanocomposite Fibers. Submitted.

Chapter 5

(6) Xu, W.; Ravichandran, D.; Jambhulkar, S.; Zhu, Y.; Song, K. Hierarchically Structured Composite Fibers for Real Nanoscale Manipulation of Carbon Nanotubes. Adv. Funct. Mater. 2021, 31 (14), 2009311.